SAPIENZA
UNIVERSITÀ DI ROMA

SCUOLA DI DOTTORATO "VITO VOLTERRA"
DOTTORATO DI RICERCA IN FISICA XXV CICLO

Search for a Standard Model Higgs boson in the $H \to ZZ^{(*)} \to 4\ell$ decay channel with the ATLAS Experiment at CERN

Thesis Advisor:

Prof. Carlo Dionisi

Candidate:

Giacomo Artoni

Ai miei genitori, a mio fratello, a mia moglie.
Senza di voi non sarei l'uomo che sono.
Grazie.

Contents

Introduction

All known particle physics processes are very well described by the Standard Model, which is an effective quantum field theory that unifies the strong, weak and electromagnetic forces. It not only provides an elegant theoretical framework, but also allows for very precise predictions, which have been thoroughly verified in the last 30 years. The only major prediction of the Standard Model which has not been verified yet is the presence of a new particle, usually referred to as Higgs boson, which is needed in the theory, along with spontaneous symmetry breaking, for all particles to acquire mass. Over the last 20 years the Large Electron-Positron collider at CERN and the Tevatron at Fermilab have been focusing on the search for this missing piece and the Large Hadron Collider has been built to fulfill this task.

On the fourth of July 2012, at a seminar held at CERN, the two experiments ATLAS and CMS have disclosed their observation of a new particle, compatible with the long-sought Higgs boson.

This thesis will focus on one of the most promising channels for the discovery, $H \to ZZ^{(*)} \to 4\ell$. The author of this thesis has provided a significant contribution to the electron identification and reconstruction improvements, as well as in the background estimations for final states with electrons, for which new methods have also been developed.

The first chapter of this thesis is dedicated to the explanation of the basic concepts of the Standard Model, such as electroweak unification and spontaneous symmetry breaking. The theoretical and experimental limits on the Higgs boson mass will be discussed, together with its production mechanisms and decay channels.

The second and third chapters provide an introduction to the Large Hadron Collider and the ATLAS experiment, respectively. The fundamental notions

and terminology relevant to a hadron collider will be introduced, and the main characteristics of the LHC will be explained. The ATLAS experiment is described in all its sub-detectors and the data acquisition and computing systems are also discussed.

The fourth chapter is devoted to a detailed explanation of the electron reconstruction in the ATLAS experiment, with particular emphasis given to the newly introduced Gaussian Sum Filter algorithm, which allows for a correct description of the energy losses due to bremsstrahlung.

The fifth chapter will be dealing with the improvements made in the electron identification and the development of the *MultiLepton* identification menu dedicated to the $H \to ZZ^{(*)} \to 4\ell$ channel.

The sixth, seventh and eighth chapters will cover the $H \to ZZ^{(*)} \to 4\ell$ analysis. In particular, the sixth chapter will start from the Monte Carlo samples used and the event selection applied and will end with the determination of data/Monte Carlo scale factors for electrons. The seventh chapter will be entirely dedicated to the background estimations made, with a particular focus on those which have been developed for final states with electrons. Finally, the eighth chapter will show the results obtained by the $H \to ZZ^{(*)} \to 4\ell$ analysis, presenting all the systematic uncertainties which have been taken into account, the upper limits on the Standard Model Higgs boson production cross section and the significance of the excess observed around 125 GeV.

The ninth and last chapter will deal with the combination of the presented result with the other search channels from the ATLAS experiment. All systematic uncertainties which are correlated along different channels will be presented together with the significance of the observed excess and the signal strength for each separate channel.

The conclusions provide a summary of the results, as well as an outline of the prospects for future work.

Chapter 1

The Higgs Boson in the Standard Model of Particle Physics

Our current understanding of the fundamental components of matter as well as of their interactions is the result of an incredible theoretical and experimental effort, culminating in the formulation of the Standard Model of particle physics. The Standard Model has been finalized in the early 1970s and has provided an explanation for many phenomena observed in the field of particle physics in the 20th century. Until today, it has been thoroughly verified by experiments and some of its predictions have been confirmed with an amazing accuracy. In this Chapter we will try to give a brief overview of the main concepts of the Standard Model and then we will focus on spontaneous symmetry breaking and the reason why it has been introduced in the theory. In the rest of the Chapter the Higgs boson production mechanisms, as well as its decay branching fractions and experimental limits on its mass will be shown.

1.1 The Standard Model

The Standard Model incorporates successfully three out of four of the known interactions in Nature, the weak, the strong and the electromagnetic one. The gravitational interaction is not included in the Standard Model but on the

scales of particle physics this is completely negligible[1]. The complete unification of the four forces is still an open issue in the world of physics.

On the merely theoretical point of view, the Standard Model is a quantum field theory that is based on the gauge symmetry $SU(3)_C \otimes SU(2)_L \otimes U(1)_Y$. This gauge group includes the symmetry group of the strong interactions, $SU(3)_C$, and the symmetry group of the electroweak interactions, $SU(2)_L \otimes U(1)_Y$. In this Chapter we will focus on the latter, which is where spontaneous symmetry breaking arises.

In Nature there exist two different kinds of fields, matter and gauge fields. The first one is composed by quarks and leptons, which are both fermions and can both be organized in three different families. Quarks are subject to all three interactions while leptons interact only weakly and electromagnetically (if they have an electric charge). These fermionic fields can be defined by means of the chirality operator, $f_{l,r} = \frac{1}{2}(1 \mp \gamma_5) f$, and their left-handed part will transform as an $SU(2)_L$ doublet while their right-handed part will transform as $SU(2)_L$ singlets. Gauge bosons are instead responsible for the interac-

Table 1.1 Names, symbols associated, electric charges and interactions for the three families of particles of the Standard Model.

Family	Symbol	Name	Electric Charge	Interactions
First	e	electron	-e	Electromagnetic/Weak
	ν_e	e neutrino	0	Weak
	u	up quark	$\frac{2}{3}$e	Electromagnetic/Strong/Weak
	d	down quark	$-\frac{1}{3}$e	Electromagnetic/Strong/Weak
Second	μ	muon	-e	Electromagnetic/Weak
	ν_μ	μ neutrino	0	Weak
	c	charm quark	$\frac{2}{3}$e	Electromagnetic/Strong/Weak
	s	strange quark	$-\frac{1}{3}$e	Electromagnetic/Strong/Weak
Third	τ	tau lepton	-e	Electromagnetic/Weak
	ν_τ	τ neutrino	0	Weak
	t	top quark	$\frac{2}{3}$e	Electromagnetic/Strong/Weak
	b	bottom quark	$-\frac{1}{3}$e	Electromagnetic/Strong/Weak

[1] the gravitational interaction is 10^{25} times less strong then the weak force.

tions we observe, as they operate as their mediators. There are twelve different gauge bosons in Nature:

Gluons

Gluons are the carriers of the strong interaction, they are electrically neutral but carry color charge. There are in total eight gluons, one for each of the generators of the $SU(3)_C$ group.

Photon

The photon is the mediator of the electromagnetic interactions, it is massless and carries no electrical charge.

$W^{\pm}$ and Z

These three gauge boson are the responsible for the weak interactions. They acquire mass through spontaneous symmetry breaking (which we will cover later in this Chapter).

1.1.1 Quantum ElectroDynamics (QED)

The first relativistic quantum field theory that has been developed is Quantum ElectroDynamics, which has been formulated to explain the electromagnetic interactions of sub-atomic particles. The following lagrangian

$$\mathscr{L}_{QED} = \bar{\psi}[i\gamma^{\mu}(\partial_{\mu} - ieA_{\mu}) - m]\psi - \frac{1}{4}F^{\mu\nu}F_{\mu\nu} \tag{1.1}$$

describes the interaction between electrons, ψ, and the electromagnetic field, A_{μ}. This lagrangian includes also solutions for an anti-particle, the positron. A fundamental characteristic of Equation 1.1 is the invariance under local gauge transformations, which transform simultaneously the photon and the electron field:

$$A_{\mu}(x) \rightarrow A'_{\mu}(x) = A_{\mu}(x) + \partial_{\mu} f(x) \tag{1.2}$$

$$\psi(x) \rightarrow \psi' = e^{ief(x)}\psi(x) \tag{1.3}$$

This theory is one of the greatest achievements in particle physics, since its predictions have been verified by experiments with an incredible precision. Two of these results are the anomalous magnetic moment of the electron and the Lamb shift of the energy levels of hydrogen.

1.1.2 Quantum ChromoDynamics (QCD)

Quantum ChromoDynamics explains how the strong interactions work via the $SU(3)_C$ group, providing a non-abelian gauge theory that describes the behavior of quarks (available in three colors and their associated anti-colors) as well as the force carriers, the gluons [1, 2, 3, 4]. This is a perfect example of an application of the Yang-Mills theory, where the gauge fields, G^a_μ, must be massless. Each of the eight generators of this non-abelian theory, T_a, will introduce a mediator, giving rise to the eight gluons already mentioned.

Finally Quantum ChromoDynamics' lagrangian can be written as

$$\mathscr{L}_{QCD} = \bar{q}(i\gamma^\mu D_\mu - m)q - \frac{1}{4}G^a_{\mu\nu}G^{\mu\nu}_a \tag{1.4}$$

where $G^a_{\mu\nu} = \partial_\mu G^a_\nu - \partial_\nu G^a_\mu + g_s f^{abc} G^b_\mu G^c_\nu$ and f^{abc} are the structure constants of the group. There are three major characteristics of the theory which are worth noting:

Self interaction of gluons

Being a non-abelian theory, gluons can have self-interactions. This cannot happen in an abelian gauge theory, such as QED.

Color confinement

Color charged particles (quarks) cannot be isolated singularly, and therefore cannot be directly observed.

Asymptotic freedom

Quarks interact weakly at high energies, allowing perturbative calculations, and strongly at low energies, preventing the unbinding of baryons (protons, neutrons, etc.) or mesons (pions, for example).

1.1.3 Weak interactions

The weak interactions have been first described by Fermi in 1934 [5], in the attempt of explaining the β radioactive decay. This description is achieved via a contact four-fermion interaction, following the Quantum ElectroDynamics paradigm:

$$\mathscr{L}_{Fermi} = -\frac{G_F}{\sqrt{2}}\bar{\psi}\gamma_\mu(1-\gamma_5)\psi\bar{\psi}\gamma^\nu(1-\gamma_5)\psi \tag{1.5}$$

This theory has the problem of violating unitarity and of not being re-normalizable, but it represents an effective theory for weak interactions at low energies.

1.1.4 Electroweak unification

Quantum ElectroDynamics and the weak interactions can be unified with the $SU(2)_L \otimes U(1)_Y$ group [6, 7, 8], whose generators allow us to have four gauge boson, W_μ^1, W_μ^2, W_μ^3 and B_μ. It is possible to apply a transformation to these fields such as to re-obtain the photon field:

$$A_\mu = W_\mu^3 \sin\theta_W + B_\mu \cos\theta_W \tag{1.6}$$

$$Z_\mu = W_\mu^3 \cos\theta_W - B_\mu \sin\theta_W \tag{1.7}$$

$$W_\mu^\pm = \frac{1}{\sqrt{2}}\left(W_\mu^1 \mp W_\mu^2\right) \tag{1.8}$$

where θ_W is the weak mixing angle, which is defined from the $SU(2)_L$ coupling constant g and the $U(1)_Y$ coupling constant g' as follows:

$$\sin\theta_W = \frac{g'}{\sqrt{g^2 + g'^2}} \tag{1.9}$$

$$\cos\theta_W = \frac{g}{\sqrt{g^2 + g'^2}} \tag{1.10}$$

The standard electric charge can thus be written as a function of g and θ_W as $e = g\sin\theta_W$.

Although very elegant, this theory is in direct contrast with experimental results. We have to note, in fact, that gauge symmetry would be violated if we were to introduce explicitly either a mass term for the vector bosons or a mass term for the fermions. Thus this theory would predict massless fermions and massless gauge bosons. In the case of fermions all their masses have been measured and found to be non-zero. For the gauge bosons, only the photon does not have mass while the other three, although not yet observed at the time this theory was proposed, are expected to be very heavy, since they are the mediators of a short range interaction.

1.1.5 The Higgs mechanism

In order to solve the mass problem and thus preserve gauge invariance, Weinberg and Salam [7, 8] used a mechanism which had been developed by Brout, Englert [9] and Higgs [10] and later by Guralnik, Hagen, Kibble and others [11]. It consists in the introduction of a complex doublet of self-interacting auxiliary scalar fields $\phi = \begin{pmatrix} h_1 \\ h_2 \end{pmatrix}$, which gives rise to spontaneous breaking of the $SU(2)_L \otimes U(1)_Y$ gauge symmetry. The lagrangian describing this field is, in fact:

$$\mathscr{L}_{Higgs} = (D^\mu \phi)^\dagger D^\mu \phi - V_{Higgs} = (D^\mu \phi)^\dagger D^\mu \phi - \mu^2 \phi^\dagger \phi - \lambda (\phi^\dagger \phi)^2 \qquad (1.11)$$

where μ and λ are free parameters. Spontaneous symmetry breaking arises

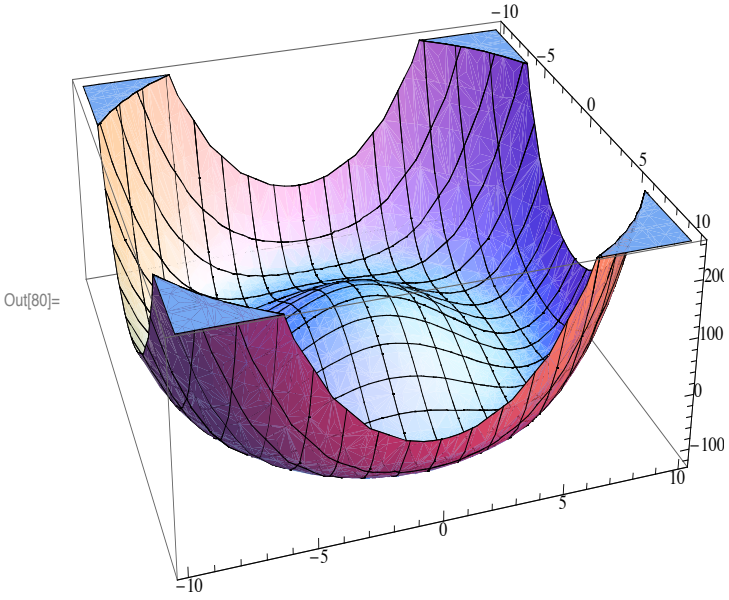

Figure 1.1 Higgs potential, $V_{Higgs} = \mu^2 \phi^\dagger \phi + \lambda (\phi^\dagger \phi)^2$, in the $Re(\phi), Im(\phi)$ plane.

if $\mu^2 < 0$. In Figure 1.1 it is shown the form of the Higgs potential, V_{Higgs}, in the $Re(\phi), Im(\phi)$ plane: the ground state of the Higgs field is given by the minimum of such a potential and it is thus degenerated. By choosing one particular state as a reference for the local gauge transformation, as for example $\phi_0 = \frac{1}{\sqrt{2}} \begin{pmatrix} 0 \\ v \end{pmatrix}$ (with $v = \sqrt{-\mu^2/\lambda}$), the system spontaneously breaks the symme-

try. If we expand around this ground state and calculate the resulting kinetic part of the Higgs lagrangian, we obtain:

$$\mathscr{L}_{Higgs}^{kinetic} = \frac{1}{2}\left(\frac{vg}{2}\right)^2 W_\mu^+ W^{+\mu} + \frac{1}{2}\left(\frac{vg}{2}\right)^2 W_\mu^- W^{-\mu} + \frac{v^2}{8}(g^2+g'^2) Z_\mu Z^\mu + \text{terms with H(x)} \tag{1.12}$$

From Equation 1.12 we can observe that three of the four degrees of freedom introduced in the theory with the complex Higgs doublet have been absorbed by the $W^\pm$ and Z bosons, thus allowing them to acquire mass:

$$\mathrm{m}_W = \frac{vg}{2} \tag{1.13}$$

$$\mathrm{m}_Z = \frac{v}{2}\sqrt{g^2+g'^2} \tag{1.14}$$

The masses of the fermions, unlike those of the vector bosons, are generated by Yukawa couplings between the fermions itself and the Higgs boson. These Yukawa terms appear in the form $\mathscr{L}_{Yukawa} = -\left(\frac{H}{\sqrt{2}}\right)\lambda_f \bar{f} f$ for each fermion f, where λ_f represents its coupling with the Higgs boson.

The electroweak theory has been deeply verified in the last thirty years of the 20$^{\text{th}}$ century, proving that the Standard Model offers a valid explanation of the nature of particle interactions. The Higgs boson has represented the only missing piece for more than a decade and has been searched by experiments at LEP, Tevatron and LHC.

1.1.6 Theoretical limits on the Higgs boson mass

The Standard Model is not able to predict the exact mass of the Higgs boson, being $\mathrm{m}_H = v\sqrt{2}$ a free parameter of the theory. The knowledge of the mass range in which the Higgs boson sits is very important in building experiments which could prove its existence. From the theoretical standpoint, there are three ways in which we can put constraints on the Higgs boson mass:

Unitarity

The scattering of longitudinal $W^\pm$ and Z bosons violates unitarity at high energy in the electroweak unification without the introduction of

the Higgs boson. By calculating the amplitude of this scattering and including diagrams with the Higgs boson, the divergence is cancelled, but only as long as $m_H < \sqrt{8\pi\sqrt{2}/3G_F} \sim 1$ TeV.

This limit is not very stringent and simply states that, if $m_H > 1$ TeV, other mechanisms should be introduced to avoid the longitudinal vector boson scattering amplitude from diverging.

Vacuum stability

The vacuum stability bound arises from the need of the potential to always be bounded from below [12]. This limit, provided by the renormalization group equations, is shown in Figure 1.2 [13].

Triviality

An upper limit on the Higgs mass can be derived from what is called the triviality bound. The running value of the coupling λ as a function of the scale, Q, is given by

$$\lambda(Q^2) = \frac{\lambda(v^2)}{1 - \frac{3\lambda(v^2)}{4\pi^2} log\left(\frac{Q^2}{v^2}\right)} \tag{1.15}$$

and if we require it to be valid also for $Q \to \infty$, we obtain a trivial theory, i.e. a theory without interactions, since $\lambda(v) \to 0$. Since such a theory is not observed in Nature, we can require the Standard Model to be valid up to a certain scale Λ and thus obtain the upper limit shown in Figure 1.2 [13].

1.1.7 Experimental limits on the Higgs boson mass

Experimental constraints on the Higgs boson mass have been collected from various experiments across the world and can be divided in two categories: indirect and direct searches.

Indirect searches

Indirect searches are based on the fact the the Higgs boson enters in loop corrections to some of the Standard Model parameters. It is thus possible to

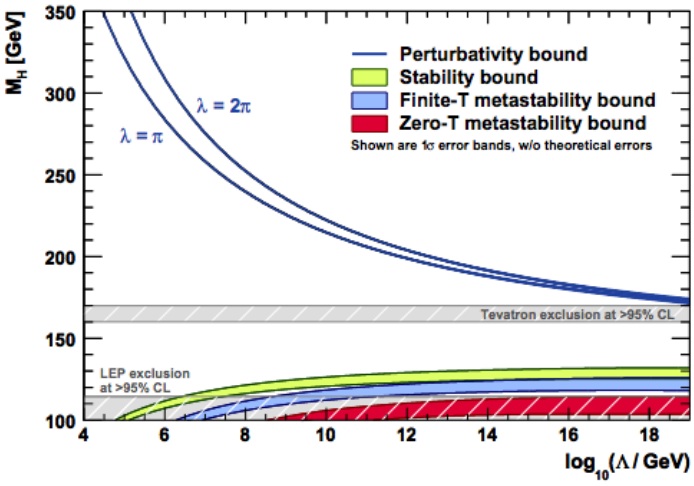

Figure 1.2 The scale Λ at which the two-loop renormalization group equations drive the quartic Standard Model Higgs coupling non-perturbative, and the scale Λ at which the same equations create an instability in the electroweak vacuum ($\lambda < 0$). The triviality upper bound is given for $\lambda = \pi$ and $\lambda = \pi$. The absolute vacuum stability bound is displayed by the light shaded green band.

combine the measurements on the set of Standard Model parameters (G_F, m_t, m_Z, α_{QED} and α_{QCD}) to obtain an indirect measurement of the Higgs boson mass. In Figure 1.3 is shown the $\Delta\chi^2$ for the fit to electroweak data, which gives a favored value for the Higgs mass of 91^{+30}_{-23} GeV [14]. This fit does not account for the direct searches of the Higgs boson performed at Tevatron and at the LHC but only relies on LEP and SLD (SLAC Large Detector) data.

Direct searches

First direct searches of the Higgs boson have been made by the four experiments at LEP (ALEPH, DELPHI, L3 and OPAL) and relied on the Higgsstrahlung production mechanism ($e^+e^-\rightarrow Z^*\rightarrow ZH$), see Section 1.1.8, and on the decay of the Higgs boson in a pair of b quarks. These searches have led to a limit of $m_H > 114.4$ GeV at a 95% of Confidence Level (CL) [15].

Also the Tevatron, with its experiments CDF and DØ, undertook the search for a Higgs, exploiting both the associated production with a vector boson and the gluon fusion production mechanisms. Tevatron's combined results with about 10 fb^{-1} exclude the presence of a Higgs boson at 95% CL in the mass

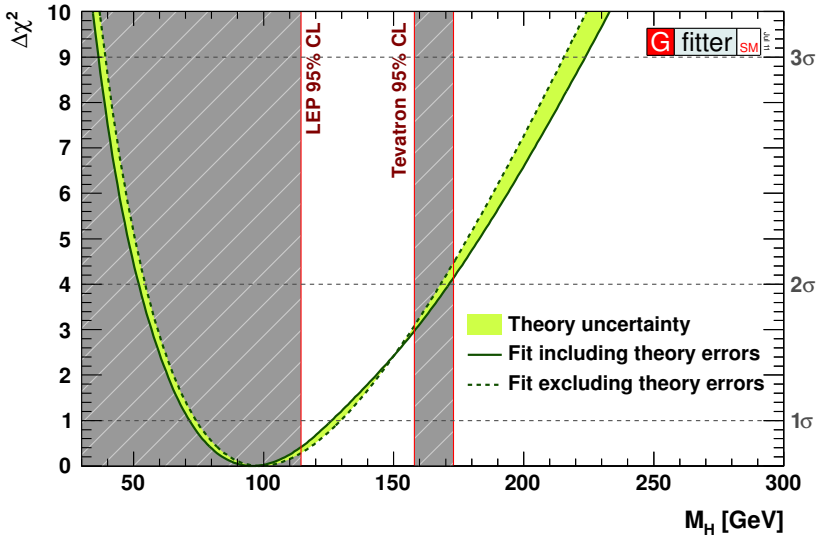

Figure 1.3 $\Delta\chi^2$ of the fit of electroweak data as a function of m_H. The solid (dashed) line gives the results when including (ignoring) theoretical errors. Exclusions from direct searches at Tevatron and at the LHC are shown in the plot but not used directly in the fit.

range 147-180 GeV, as can be seen in Figure 1.4 [16].

For what regards the LHC experiments, the situation until 2012 summer is shown in Figure 1.5 for ATLAS and in Figure 1.6 for CMS, in particular in Figure 1.5a and Figure 1.6a for the low mass range and in Figure 1.5b and Figure 1.6b for the whole mass range. The excluded area covers almost the complete mass range and only one small region at 118 GeV and another one between 122 and 130 GeV are still allowed [17, 18].

1.1.8 Higgs boson production mechanisms at the LHC

The Feynman diagrams for those processes that mainly contribute to the production of a Higgs boson at a hadron collider are shown in Figure 1.7. The cross sections for the same processes are shown in Figure 1.8 for pp collisions at $\sqrt{s}$ = 7 TeV and $\sqrt{s}$ = 8 TeV [19, 20].

Gluon-gluon fusion

The gluon-gluon fusion process is the most important mechanism at the LHC, for any m_H. The Higgs is produced by the fusion of two gluons via

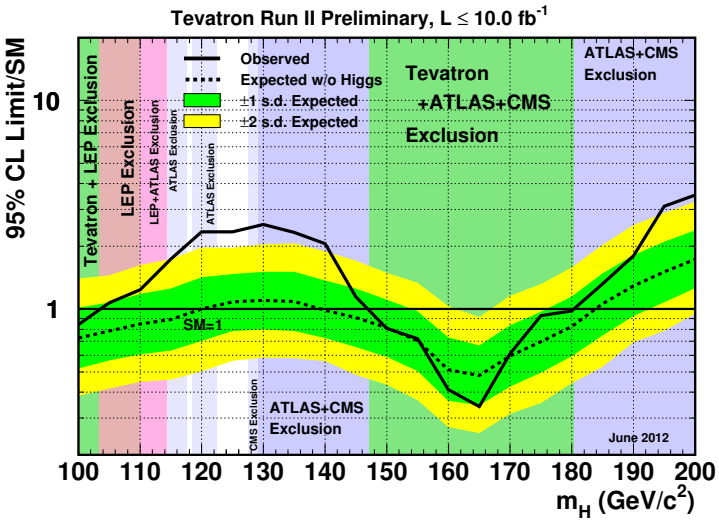

Figure 1.4 Exclusion limits obtained by the combination of the results from the CDF and DØ experiment at the Tevatron. The range excluded at 95% CL is 147-180 GeV. Also limits set by ATLAS and CMS are shown, as well as those from LEP.

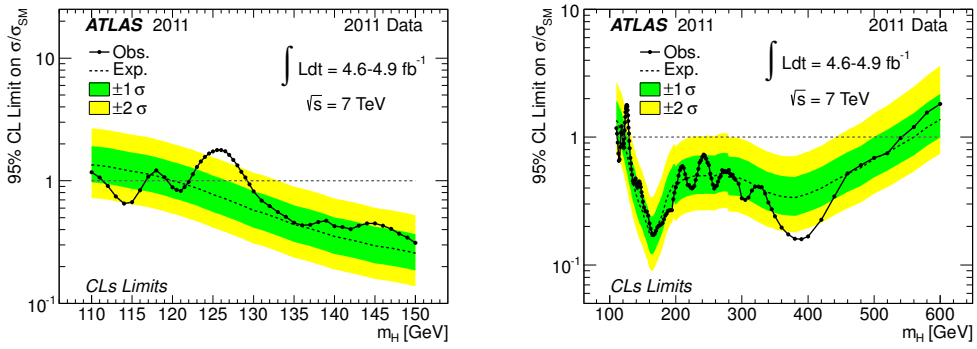

(a) **(b)**

Figure 1.5 Exclusion limits set by the ATLAS experiment at CERN [17], using 4.6-4.9 fb^{-1} of data collected during 2011 at $\sqrt{s}$ = 7 TeV.

a quark loop. Since the coupling of a fermion to the Higgs is proportional to the fermion's mass, the biggest contribution will be given by a loop with a top quark, which is the one indicated in Figure 1.7a.

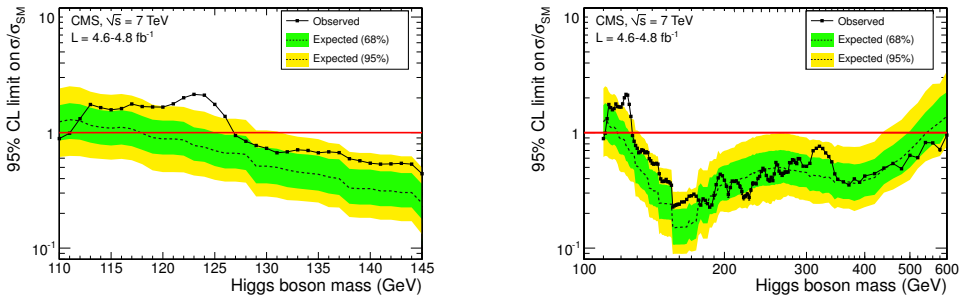

Figure 1.6 Exclusion limits set by the CMS experiment at CERN [18], using 4.6-4.8 fb^{-1} of data collected during 2011 at $\sqrt{s}$ = 7 TeV.

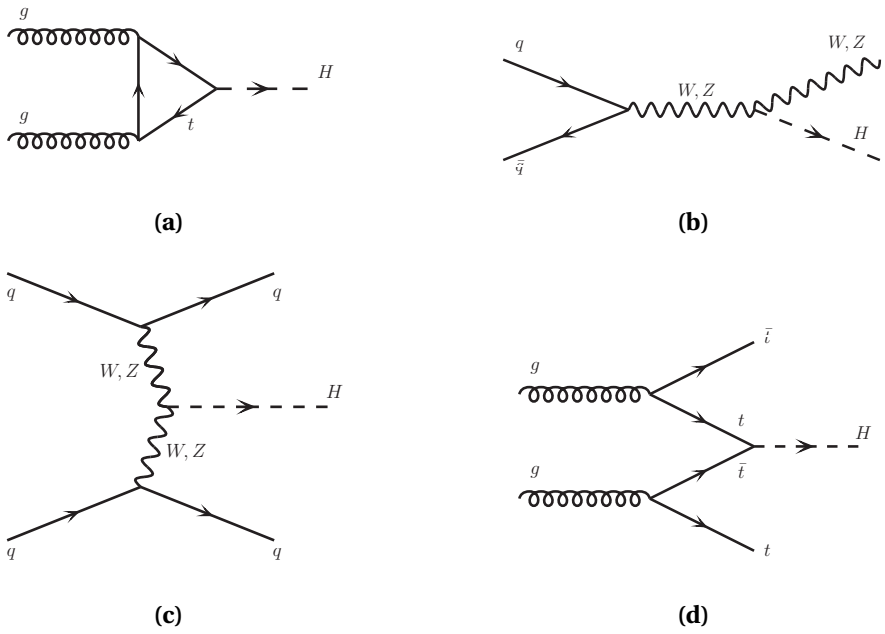

Figure 1.7 Feynman diagrams for the tree level production mechanisms for the Higgs boson at the LHC: (a) gluon-gluon fusion, (b) associated production with a $W^{\pm}$ or Z, (c) vector boson fusion and (d) $t\bar{t}$ associated production.

Vector boson fusion

The second dominant contribution to the total production cross section of the Higgs at LHC is given by the vector boson fusion process (see Figure 1.7c), which is still about one order of magnitude lower than the gluon-gluon fusion process. Its relevance is given by the very clean ex-

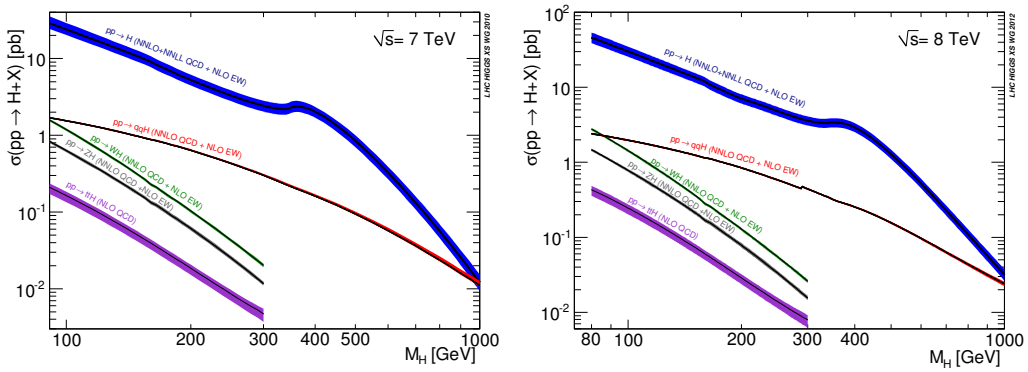

(a) **(b)**

Figure 1.8 Higgs boson production cross sections for pp collisions at $\sqrt{s}$ = 7 TeV (a) and at $\sqrt{s}$ = 8 TeV (b) as a function of m_H.

perimental signature that it provides: the two vector bosons that produce the Higgs are irradiated from quarks and these will hadronize to high energy jets. These jets could be easily recognized in the detector and provide a way to tag signal events and discriminate them from backgrounds.

Associated production with a $W^{\pm}$ or a Z

In this process, the Higgs boson is radiated from a $W^{\pm}$ or a Z boson and for this reason it is also called *Higgsstrahlung*. In this case the tagging of a signal event can be done by reconstructing the original boson that irradiated the Higgs, thus allowing for a cleaner experimental signature. This process, anyway, contributes very little to the final cross section.

Associated production with a $t\bar{t}$ pair

Also this process provides a clean experimental signature, having two top quarks in the final state together with the Higgs. As for the associated production with a $W^{\pm}$ or a Z, the cross section of this process is very small and becomes almost negligible when comparing it to the gluon-gluon or vector boson fusion processes.

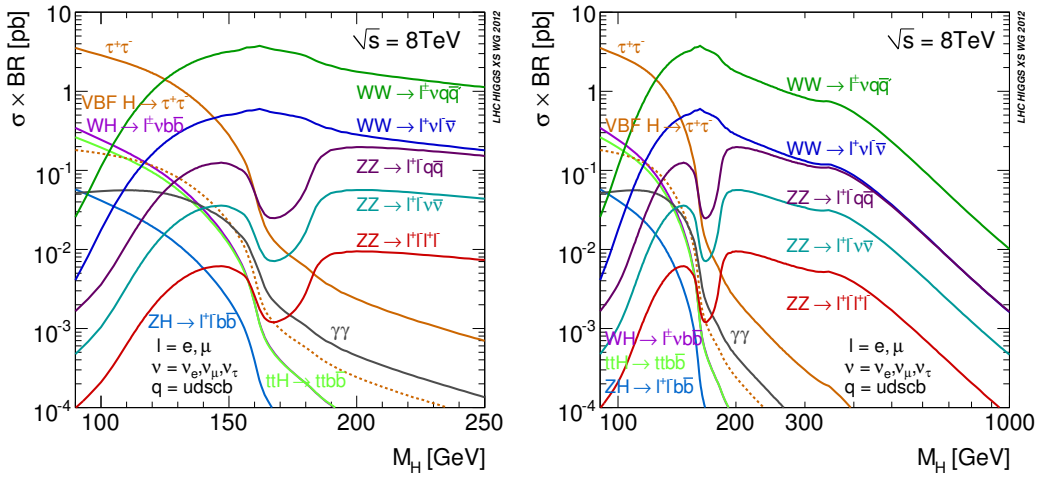

Figure 1.9 Higgs boson branching ratios multiplied by the total Higgs production cross section at $\sqrt{s}$ = 8 TeV as a function of m_H, for the low mass range (a) and for the high mass range (b).

1.1.9 Higgs boson decay

The different branching fractions for the Higgs boson multiplied by the total Higgs production cross section (at $\sqrt{s}$ = 8 TeV) are shown in Figure 1.9, for the mass ranges 90-250 GeV (Figure 1.9a) and 90 GeV-1 TeV (Figure 1.9b) [19, 20]. Here we analyze briefly the most promising channels in the different mass ranges.

Low mass, 115 < m_H < 130 GeV

In the low mass region, the highest branching ratio is the one of $H \to b\bar{b}$, since the Higgs couplings to the fermions are proportional to the mass. Nevertheless this is not the best experimental way to look for a Higgs boson at low mass since the di-jet background has a cross section more than six orders of magnitude higher than that of $pp \to H \to b\bar{b}$. The most promising way to observe a Higgs boson at very low mass is provided by the $H \to \gamma\gamma$ channel. Although it has a very small branching ratio (of the order of 10^{-3}), the signal to background ratio is of the order of 10^{-2}. Together with $H \to \gamma\gamma$, the $H \to ZZ^{(*)} \to 4\ell$ channel is expected to be very sensitive in this mass range. Despite the tiny branching ratio, see Fig-

ure 1.9, it can exploit the very clean signature provided by four leptons (electrons or muons) in the final state.

Intermediate mass, 130 < m_H < 180 GeV

In this region the most promising channels are given by the Higgs boson decaying into pairs of vector bosons, $H \to WW^{(*)}$ and $H \to ZZ^{(*)}$. The difference in the two branching ratios arises both from different couplings to the Higgs, as can be seen in Figure 1.10, and from the two Z bosons being identical particles (reducing by half the $H \to ZZ^{(*)}$ branching ratio). As a result, the $H \to WW^{(*)}$ branching ratio is always higher than the Z boson one, in particular around $2m_W$ when the production of two on-shell W becomes possible. Since there are two neutrinos in the final state for this process, it is very challenging experimentally but less sensitive than $H \to ZZ^{(*)}$ and it does not allow for a complete reconstruction of the Higgs' decay. In this mass range the best channel is clearly $H \to ZZ^{(*)} \to 4\ell$, which provides a signal to background ratio of about one.

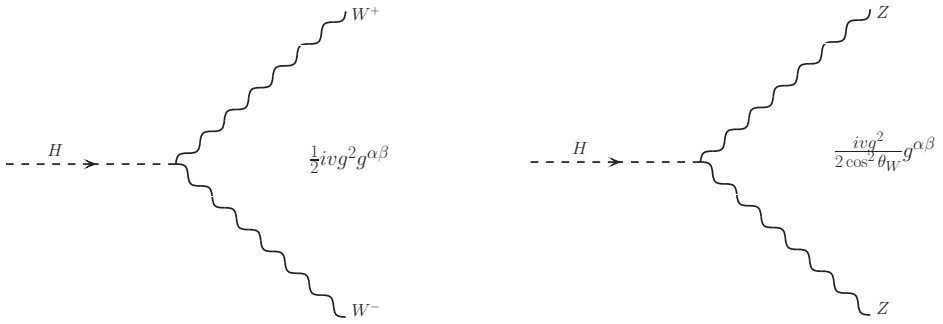

(a) **(b)**

Figure 1.10 Different couplings of the W and Z to the Higgs boson [21]).

High mass, 180 < m_H < 600 GeV

In this mass range, which is above the threshold for the production of two on-shell Z, the $H \to ZZ^{(*)} \to 4\ell$ channel still provides the best way to observe a Higgs boson. Other channels with higher branching ratios,

such as $H \to ZZ^{(*)} \to \ell\ell qq$ and $H \to ZZ^{(*)} \to \ell\ell\nu\nu$, can contribute for high values of m_H.

Finally, in Table 1.2, we list some of the relevant information for the channels that contribute to the search at low mass, for the ATLAS Experiment. For each channel the mass range explored, the signal/background ratio expected, the number of signal events expected and the expected resolution on the Higgs mass are shown.

Table 1.2 Mass range explored, signal/background ratio expected, number of signal events expected and expected resolution on the Higgs boson mass for the $H \to ZZ^{(*)} \to 4\ell$, $H \to WW^{(*)} \to \ell\nu\ell\nu$, $H \to \gamma\gamma$, $H \to \tau^+\tau^-$ and $H \to b\bar{b}$ channels in the ATLAS Experiment.

Channel	Mass Range (GeV)	S/B	Expected Signal Events	σ_{m_H} (GeV)
$H \to ZZ^{(*)} \to 4\ell$	110-600	1	5	2
$H \to WW^{(*)} \to \ell\nu\ell\nu$	110-600	0.1	56	~30
$H \to \gamma\gamma$	110-140	0.03	190	1.6
$H \to \tau^+\tau^-$	110-140	0.01	26	poor
$H \to b\bar{b}$	110-140	0.01	5	poor

1.1.10 Higgs boson total decay width

The total decay width of the Higgs boson is shown in Figure 1.11, as a function of m_H. It is of the order of the MeV below the $2m_W$ threshold and then it rapidly increases. With m_H below $2m_Z$, the detector resolution dominates over the Higgs width, since it is of maximum 1 GeV. Above the threshold for the production of two on-shell Z, the width is dominated by the decays in two W or two Z and continues to increase, reaching almost 1 TeV for $m_H \simeq 1$ TeV [19].

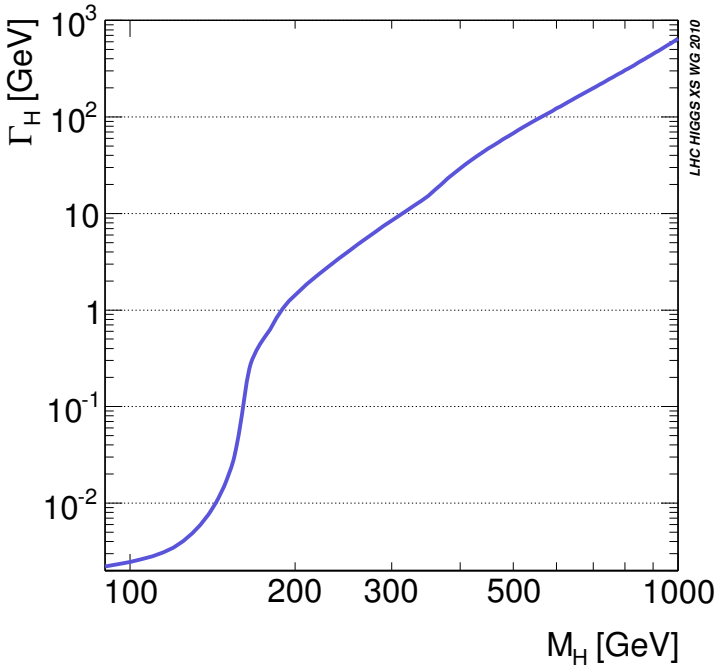

Figure 1.11 Total decay width of the Higgs boson as a function of m_H.

Chapter 2

The Large Hadron Collider

The Large Hadron Collider (LHC) is the largest and highest energy particle accelerator ever built. It is a project developed by the European Organization for Nuclear Research (CERN) to test the predictions of the Standard Model of particle physics and to discover the existence of the Higgs boson or of other particles.

2.1 General remarks

The LHC is a proton-proton collider designed to have a center-of-mass energy of 14 TeV and an instantaneous luminosity of $10^{34}\text{cm}^{-2}\text{s}^{-1}$, which translates into every proton being accelerated at a speed which is 99.9999991% of the speed of light [22, 23, 24]. The tunnel of the Large Electron-Positron Collider (LEP) [25] has been re-used for this purpose: it is 26.7 km long and lies beneath France and Switzerland, near Geneva.

The number of events generated for a specific process can be written, as it is common practice in particle physics, as $N = L \cdot \sigma$, where σ represents the cross section of the process being taken into account and $L = \int \mathscr{L} dt$ is the luminosity, integrated over time, provided by the machine. Since the intent of the LHC is to explore physics which has not been seen so far, the cross sections of the processes of interest will be very small and thus the luminosity

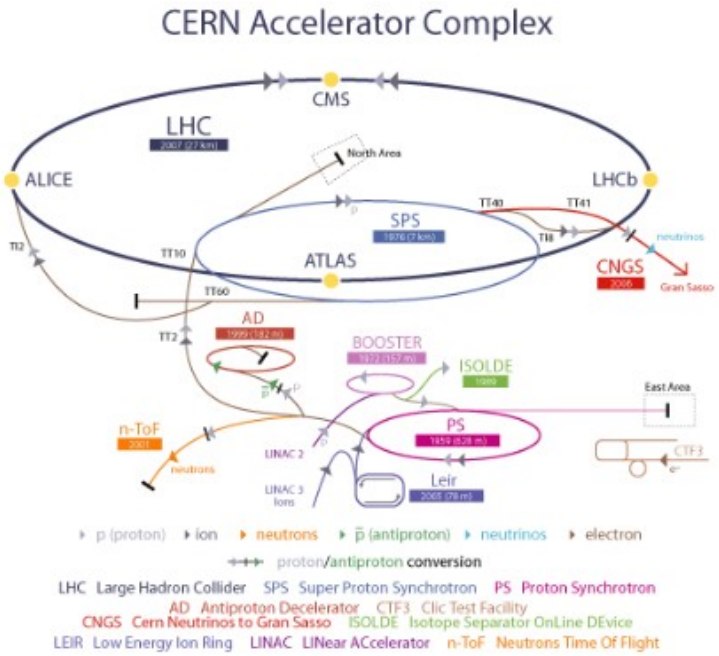

Figure 2.1 Schematic view of the Large Hadron Collider.

must be maximal. The instantaneous luminosity can be written as follows:

$$\mathscr{L} = \frac{N_b^2 n_b f_r \gamma_r}{4\pi\varepsilon_n \beta^*} \cdot (1 + (\frac{\theta_c \sigma_z}{2\sigma^*}))^{-1/2} \tag{2.1}$$

and all these parameters, explained in Table 2.1, have been optimized to ensure maximal luminosity.

2.2 2011 and 2012 data taking

On September 2008, a faulty electrical connection between two of the accelerator's magnets caused a large helium leak into sector 3-4 of the LHC [26]. This incident resulted in mechanical damage and release of helium from the magnet cold mass into the tunnel. In order to prevent this from happening again, the center of mass energy has been reduced to 7 TeV for the data taking periods of 2010 and 2011, while in 2012 the machine was running at $\sqrt{s}$ = 8 TeV.

N_b	$1.67 \cdot 10^{11}$	Number of protons per bunch
n_b	2808	Number of bunches
f_r	400.79 MHz	RF frequency
ε_n	3.75 μm	Transverse normalized emittance
σ_z	7.55 cm	RMS bunch length
σ^*	16.7 μm	RMS beam size at the interaction point
β	0.55 m	Lorentz factor
γ_r	7461	Relativistic gamma factor
θ_c	$\pm$142.5 μrad	Crossing angle between the beams

Table 2.1 Relevant design parameters of the LHC.

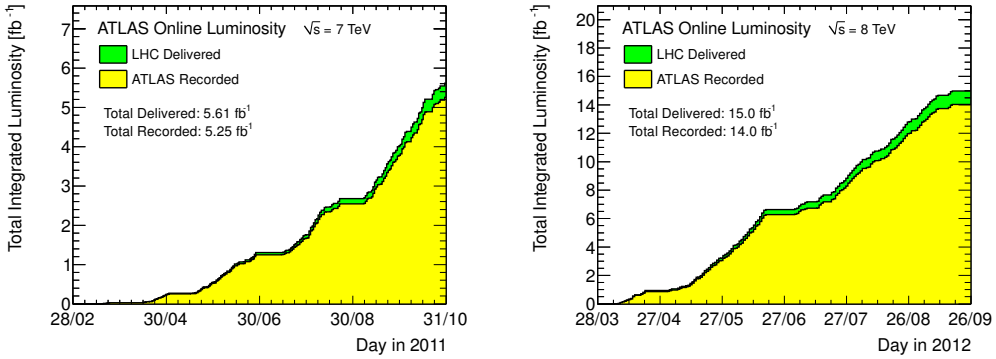

(a) **(b)**

Figure 2.2 Cumulative luminosity versus day delivered to (green), and recorded by ATLAS (yellow) for pp collisions at $\sqrt{s}$ = 7 TeV in 2011 (a) and at $\sqrt{s}$ = 8 TeV in 2012 (b). The results shown in this thesis have been obtained using these two datasets up to the technical stop which took place in mid-June 2012.

In this thesis we used data from 2011 and the first half of 2012 and we were thus forced into splitting our analysis in two separate analyses since many theoretical parameters change with the center of mass energy, as explained in Chapter 1. In Figure 2.2 are shown the luminosities delivered by the LHC (green) and recorded by ATLAS (yellow) for both 2011 and 2012. The results shown in the following of this thesis are based on the 5.25 fb^{-1} collected in 2011 and on the 6.3 fb^{-1} collected in 2012 until mid-June. The exact luminosi-

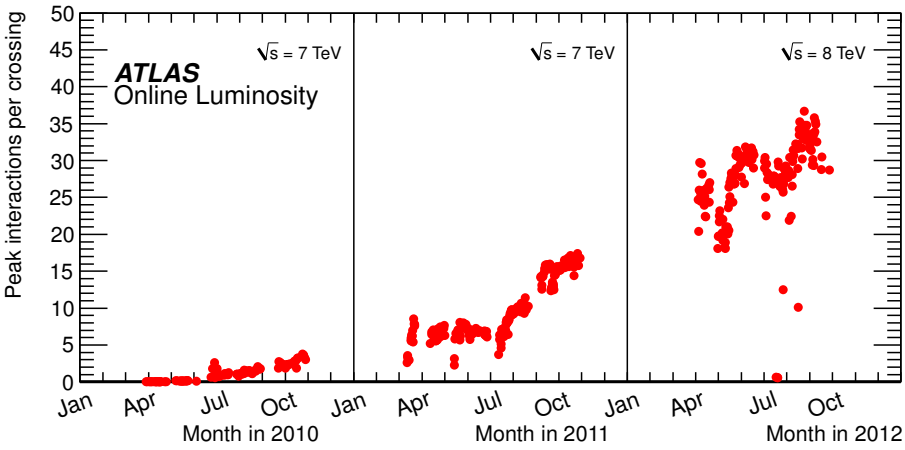

(a)

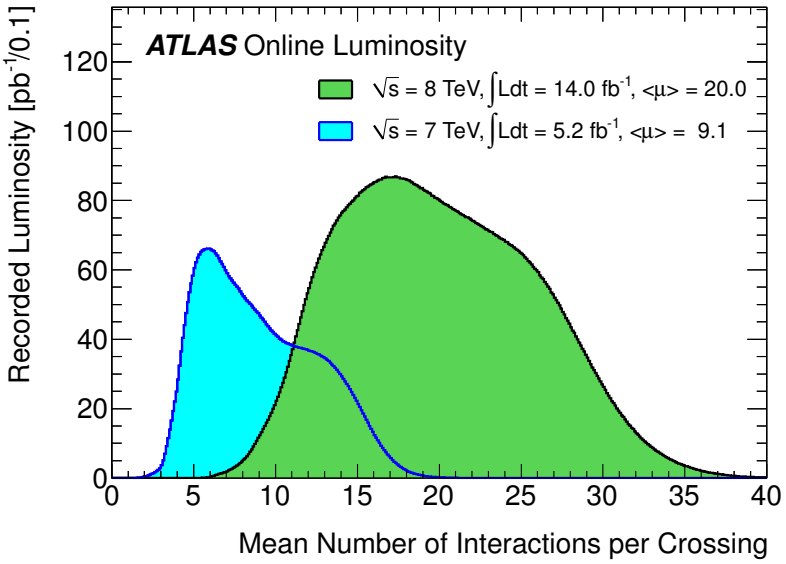

(b)

Figure 2.3 Number of interactions per bunch crossing plots. In (a) is shown the maximum mean number of events per beam crossing as a function of the day in the years 2010, 2011 and 2012. In (b) are shown the luminosity-weighted distributions of the mean number of interactions per crossing for the 2011 and 2012 data.

ties used in the analysis are shown in Chapter 6 and are smaller than these ones since we have to take into account detector inefficiencies, which in turn depend on the objects we are using in our final state [27, 28].

The striking performance of the LHC in 2012 allowed ATLAS to collect, in the period from January to June 2012, more statistics then all the previous years combined. This is the result of an enormous quantity of bunches colliding in ATLAS and this is reflected in the mean number of interactions for each bunch crossing, as shown in Figure 2.3. The increasing of the mean number of interactions per bunch crossing is also known as “pile-up” effect, since events that occur in the same interaction will pile up in the detectors, reducing the experimental resolution. Since this effect is already larger than what we expected when designing the LHC, special care has been taken for 2012 data, to ensure that all objects are reconstructed correctly as in the case of 2011 data.

Chapter 3

The ATLAS Detector

In this chapter we will present the most important features of the ATLAS experiment, its trigger system and, finally, the software and GRID infrastructure which have been fundamental for the analysis.

3.1 General Overview

The ATLAS detector is one of the four experiments working at the Large Hadron Collider at CERN [29, 30, 31]. It has been designed to investigate the physics at the TeV energy scale and, most important of all, to look for the Higgs boson.
A layout of the whole experiment is visible in Figure 3.1 and in Table 3.1 we summarized some of the most important facts about the ATLAS detector.

Table 3.1 Summary of the relevant facts concerning the ATLAS detector.

Height / Diameter	25 m
Length	44 m
Weight	7000 tonnes
Length of cables	3000 km

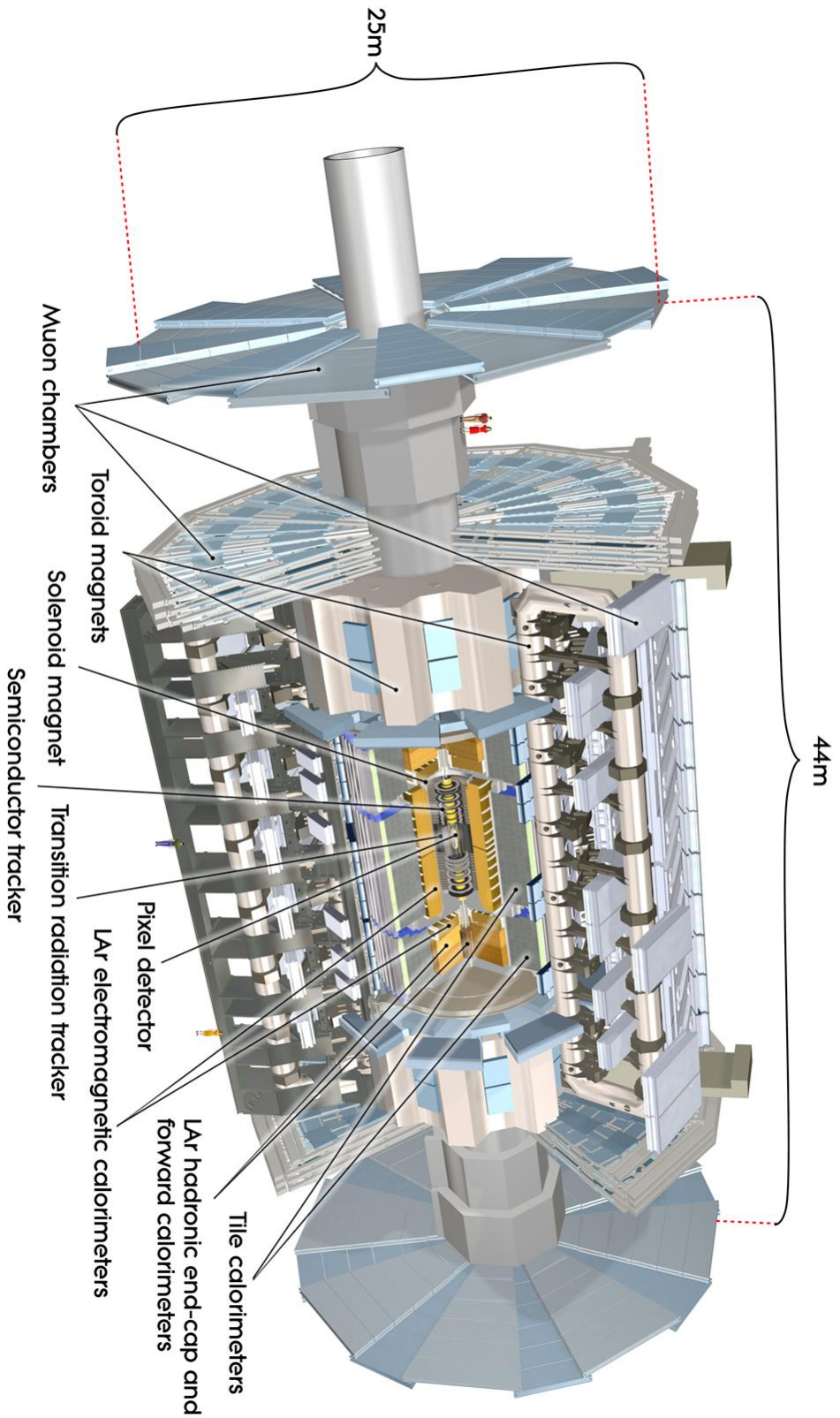

Figure 3.1 Layout of the ATLAS Experiment.

3.2 Coordinate System

The coordinate system used in ATLAS is a right-handed coordinate system with the x-axis pointing towards the centre of the LHC tunnel, and the z-axis along the beam line. As it is possible to see in Figure 3.2, the y-axis is tilted from vertical due to the general tilt of the LHC tunnel. In ATLAS, as in all other

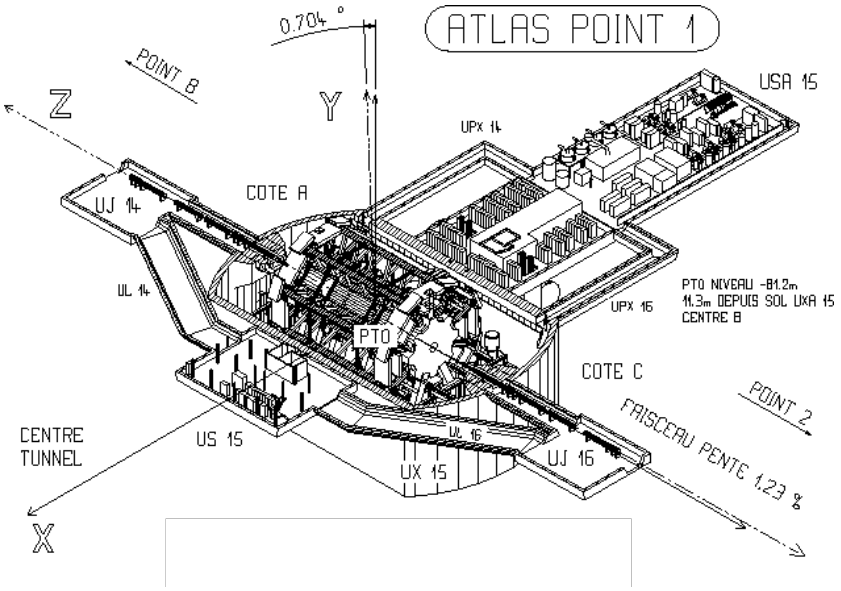

Figure 3.2 Coordinate system of the ATLAS experiment.

experiments at a hadron collider, cylindrical coordinates are used instead of xyz coordinates: we use the azimuthal angle ϕ and, instead of the polar angle θ, we use rapidity, defined in Equation 3.1, in case of a massive particle, or pseudo-rapidity, defined in Equation 3.2, in case the mass of the object can be neglected.

$$y = \frac{1}{2} log\left(\frac{E+P_z}{E-P_z}\right) \tag{3.1}$$

$$\eta = -log\left(\tan\frac{\theta}{2}\right) \tag{3.2}$$

This choice is driven by the fact that at a hadron collider the total momentum of the initial system along the z-axis cannot be known (since the collision takes place at the parton level, not at the proton level). For this reason we have to use a quantity which is not dependent on Lorentz' boosts along the

z-axis[1]. Pseudo-rapidity is commonly used to divide the ATLAS detector in sections with different characteristics. For example, we are used to dividing the detector in two halves, side A ($\eta > 0$) and side C ($\eta < 0$). In general, the central part of the detector ($|\eta| < X$, where X depends on the specific sub-detector) is denoted as barrel, while the other parts ($|\eta| > X$) are denoted as endcaps.

Other important quantities commonly used in ATLAS are the transverse momentum p_T, the transverse energy E_T and the missing transverse energy E_T^{miss}, which are all defined in the xy plane. This is, in fact, the only plane where energy and momentum conservation laws can be applied.

Finally, the distance between two particles in ATLAS in the $\eta-\phi$ coordinate system is in general indicated using the ΔR coordinate, defined as follows:

$$\Delta R = \sqrt{\Delta\eta^2 + \Delta\phi^2} \tag{3.3}$$

3.3 Magnets

A magnetic field is fundamental for measuring the momenta of all the produced charged particles in the experiment. The ATLAS Magnet System is made out of superconducting magnets of three different kinds [32]:

Central Solenoid

In order to reconstruct the transverse momenta of all the charged particles coming from the interaction point, a solenoidal magnet has been designed to provide a magnetic field of ~2 T for the Inner Detector [33].

Barrel Toroid

An air-core toroid has been built for the muon spectrometer of the ATLAS experiment in the central region of the detector [34].

Endcap Toroids

Also the non-central regions of the muon spectrometer have been instrumented with a toroidal field, provided by two air-core toroids, one for Side A and one for Side C [35].

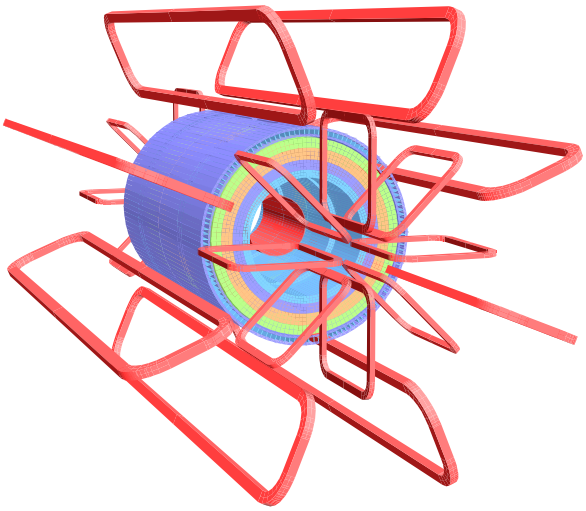

Figure 3.3 Schematic view of the magnetic fields in the ATLAS Experiment: in red are visible the toroidal magnets while in blue is highlighted the solenoid at the center of the detector.

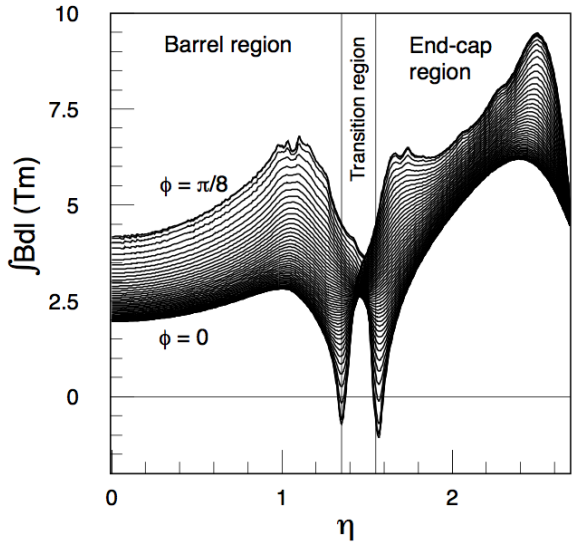

Figure 3.4 Field integral $\int Bdl$ of the ATLAS experiment as a function of pseudo-rapidity, with different starting angles.

The magnetic field provided by this system is not completely uniform, due to the complexity of the toroids. In Figure 3.4 it is shown the field integral $\int Bdl^2$ as a function of pseudo-rapidity for different starting angles. This bending power ranges from 2 to 6 Tm for the barrel, while it ranges from 4 to 8 Tm in the endcap. The superposition of the magnetic fields of the barrel and end-cap toroids originates the transition region, $1.3 < |\eta| < 1.6$, where the bending power is much poorer.

3.4 Tracking System: Inner Detector

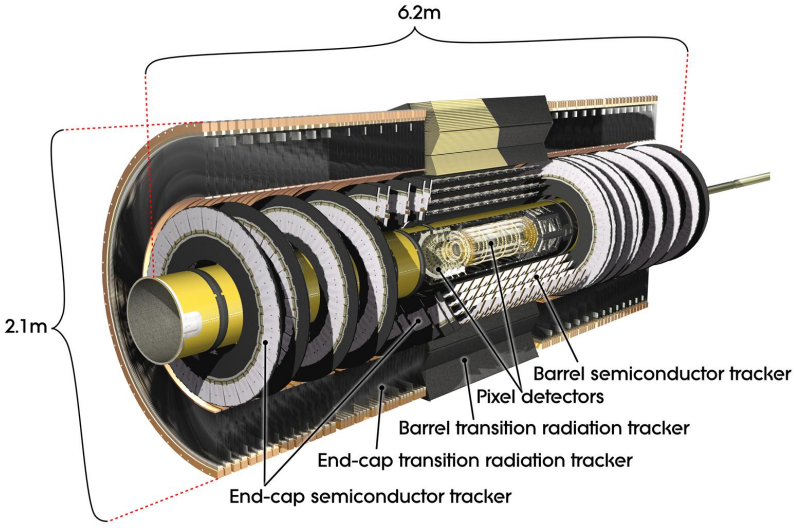

Figure 3.5 Cut-away view of the ATLAS Inner Detector.

The ATLAS Inner Detector tracker, often referred to as ID, is the innermost sub-detector of the experiment [36, 37]. Its duty is to reconstruct vertices and momenta of all the charged particles produced in the interaction point. In particular, there are three different components of the Inner Detector, the Silicon Pixel Detector, the SemiConductor Tracker and the Transition Radiation

[1] To be more precise, only differences in pseudorapidity can be considered Lorentz invariants: $\Delta\eta = \eta_1 - \eta_2$

[2] B is the azimuthal field component while dl is a straight line trajectory between the inner and the outer radius of the toroids.

Tracker. All three sub-detectors combined allow to have a very good precision on the momenta of the charged particles [38], such as:

$$\sigma_{p_T}/p_T = 0.05\% p_T \oplus 1\% \tag{3.4}$$

3.4.1 Silicon Pixel Detector

This detector is the nearest to the beam line and its major contribute is in the accurate measurement of vertices. In order to achieve this, it has been instrumented with 1744 modules each one consisting of a 16.4 x 60.8 mm wafer of silicon with 46080 pixels. This makes a total of about 80 million channels in a cylinder 1.4 m long and with a diameter of 0.5 m. The pixel layers are segmented in R-ϕ and z with typically three pixel layers crossed by each track. The first layer, usually called the Blayer, is at a radius of 51 mm and is necessary for vertexing. The intrinsic accuracies in the barrel are 10 mm (R-ϕ) and 115 mm (z) and in the disks in the endcap are 10 mm (R-ϕ) and 115 mm (R) [39].

3.4.2 SemiConductor Tracker

Just outside the Pixel detector there is the SemiConductor Tracker, consisting of eight strip layers, which should provide four space points. In the barrel region, this detector uses small-angle (40 mrad) stereo strips to measure both coordinates. In the endcap region, the detectors have a set of strips running radially and a set of stereo strips at an angle of 40 mrad. The total number of readout channels in the SCT is approximately 6.3 million.

3.4.3 Transition Radiation Tracker

The Transition Radiation Tracker consists of straw-tubes with a diameter of 4 mm each. The TRT can provide a high number of hits (usually 30 per track, with a possible maximum of 36) only in the region $|\eta| < 2.0$. The TRT provides information regarding only the R-ϕ plane and is capable of providing good electron-hadron separation [40].

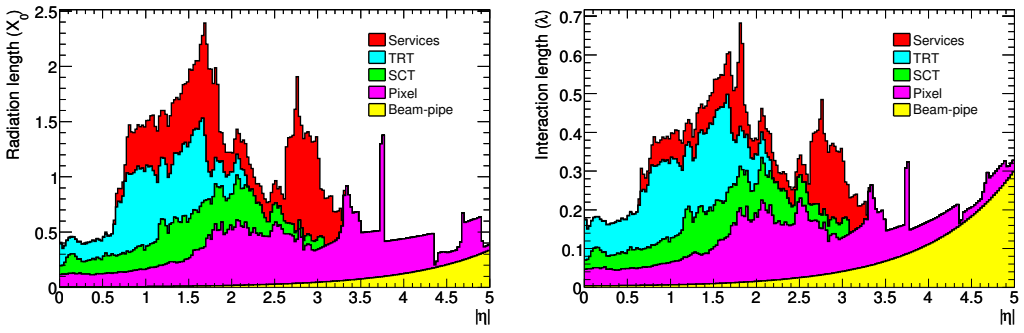

(a) **(b)**

Figure 3.6 Material distribution (X_0 in Figure 3.6a, λ in Figure 3.6b) at the exit of the ID envelope, including the services and thermal enclosures. The distribution is shown as a function of $|\eta|$ and averaged over ϕ. The breakdown indicates the contributions of external services and of individual sub-detectors, including services in their active volume.

Table 3.2 Summary of accuracies of the Inner Detector.

Detector	R-ϕ accuracy (μm)	z accuracy (μm)	R accuracy (μm)
Pixel			
BLayer (or Layer-0)	10	115	-
Layer-1	10	115	-
Layer-2	10	115	-
Disks	10	-	115
SCT			
Barrel	17	580	-
Disks	17	-	580
TRT	130	-	-

3.5 Calorimeters

In this section, the full ATLAS calorimetry system will be described. For details about coverage and segmentation of each part of the calorimeter, see also Table 3.3 [41].

3.5.1 Electromagnetic Calorimeter

The EM calorimeter is a sampling calorimeter made of Liquid Argon (LAr) as scintillating material and lead as absorbing material [42, 43, 44]. It consists of a barrel calorimeter which covers the range $|\eta| < 1.475$ and of an endcap calorimeter which extends from $|\eta| = 1.375$ to $|\eta| = 3.2$. As it is visible in Figure 3.7, the EM calorimeter is accordion shaped, providing complete coverage and symmetry in the azimuthal angle ϕ. The thickness of the lead absorber plates as well as the LAr gaps have been optimized to maximize energy resolution in the calorimeter. The total thickness provided by the EM calorimeter is $X_0 > 24$ in the barrel and $X_0 > 26$ in the endcaps. The resolution provided by the EM calorimeter is:

$$\frac{\sigma_E}{E} = \frac{10\%}{\sqrt{E}} \oplus 0.3\% \tag{3.5}$$

$$\sigma_\eta = \frac{40 \text{ mrad}}{\sqrt{E}} \tag{3.6}$$

where E must be used in GeV.

In the region $|\eta| < 2.5$, which is the one also covered by the tracking system and dedicated to precision measurements, the EM calorimeter has three longitudinal layers:

1st Sampling

The first sampling is 4.3 X_0 thick and has small strips in η ($\Delta\eta = 0.0031$). This is very useful to separate photons from π^0, as well as electrons from $\pi^\pm$.

2nd Sampling

The second sampling provides ~ 16 X_0 and thus the majority of the energy will be deposited in this layer. It is segmented into square towers since the measurement of both coordinates in this layer is equally important ($\Delta\eta \times \Delta\phi = 0.025 \times 0.025$).

3rd Sampling

The third and last sampling is specifically dedicated to high energy electrons (E > 50 GeV) which will have large clusters and thus the size of the towers in η can be doubled without loss in resolution.

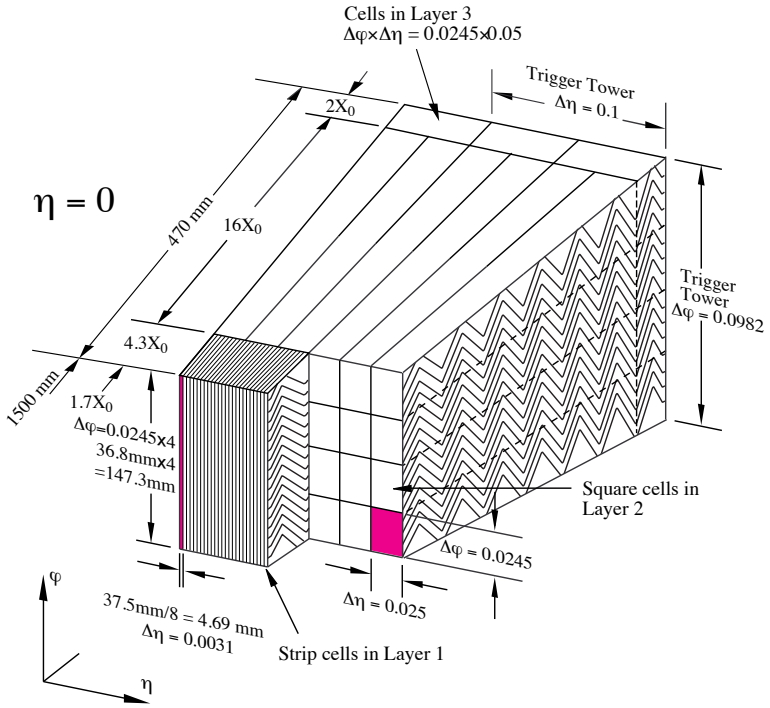

Figure 3.7 Structure of the EM calorimeter in the barrel. It is clearly visible the accordion shape and the three samplings with different granularities. The presampler is not shown and lies in front of the accordion.

3.5.2 Hadronic Calorimeters

In ATLAS, hadronic calorimeters cover the range $|\eta| < 4.9$ and exploit different techniques, since the resolution requirements and radiation environment change dramatically over this large η-range. A fundamental aspect for the hadronic calorimeter is its thickness, to contain hadronic showers and reduce punch-through into the muon system. In order to obtain this, it has been designed to provide 11 interaction lengths (λ) at $\eta = 0$, which are sufficient to reduce the rate of punch-through below the irreducible level of prompt μ or μ from semi-leptonic decays of $\pi^{\pm}$ and $K^{\pm}$. In the region $|\eta| < 3.1$ the hadronic calorimeter can provide a resolution which is:

$$\frac{\sigma_E}{E} = \frac{50\%}{\sqrt{E}} \oplus 3\% \tag{3.7}$$

while in the forward region ($3.1 < |\eta| < 4.9$) the resolution is the following:

$$\frac{\sigma_E}{E} = \frac{100\%}{\sqrt{E}} \oplus 10\% \tag{3.8}$$

and the energy E must always be considered in GeV.

Tile Calorimeter

In the barrel region, the hadronic calorimeter (positioned just after the EM calorimeter) has been assembled with iron plates as absorber and scintillating tiles as active material. These tiles have been placed in such a way that the shower should enter them from the side, in an attempt of improving e/h (the ratio between the hadronic calorimeter response for an electron and for a hadron) which is close to 1.3. The tile calorimeter is composed by the barrel section, which covers the region $|\eta| < 1.0$, and two extended barrels, which extend in $0.8 < |\eta| < 1.7$ [45, 46].

Liquid-Argon hadronic endcap Calorimeters

Each hadronic endcap calorimeter (usually referred to as HEC) consists of two independent wheels of outer radius 2.03 m. The first wheel is built out of 25 mm copper plates, while the second one uses 50 mm plates, as cost savings measure. This calorimeter is still a sampling calorimeter using LAr as

scintillating material, but in this case copper has been chosen as the absorber, since the amount of radiation is higher in the endcaps [42, 44].

Liquid-Argon forward Calorimeter

The ATLAS forward calorimeters (FCal) are situated inside the endcap cryostats together with the EM endcap calorimeter and also the hadronic endcap calorimeter. The FCal covers the very forward regions of $3.1 < |\eta| < 4.9$, where the energies and density of particles are very high. The FCal consists of three layers: the layer closest to the interaction point is a Cu/LAr calorimeter designed for electromagnetic calorimetry. The other two layers are hadronic W/LAr calorimeters. Behind the FCal is a passive layer of brass that absorbs hadronic shower remnants that punch through [42, 44].

3.6 Muon Spectrometer

The ATLAS muon spectrometer is instrumented with separate trigger and high-precision tracking chambers in the toroidal magnetic field described in Section 3.3 [47]. In the barrel region ($|\eta| < 1.0$), these chambers are arranged in three cylindrical layers, which are usually called "stations", around the beam axis, while in the endcap region ($1.0 < |\eta| < 2.7$) they are installed in three different wheels. In Figure 3.8 it is shown the layout of the muon chambers in the x-y plane for the barrel, while in Figure 3.9 it is shown the R-z projection for both barrel and endcap. The overall momentum resolution, σ_{p_T}/p_T achieved by the ATLAS muon spectrometer is ~2-3% over most of the kinematic range while for high-momenta it reaches ~10% for p_T = 1 TeV/c [48].

3.6.1 Monitored drift-tube chambers (MDT)

The high-precision chambers in both barrel and endcap are the MDTs, which are composed by aluminium tubes of 30 mm of diameter and 400 μm of wall thickness. In the middle of each tube there is a Tungsten-Rhenium wire of 50 μm diameter and the tubes are filled with a mixture of 93% Ar and 7% CO_2 at an absolute pressure of 3 bar. These characteristics provide a very

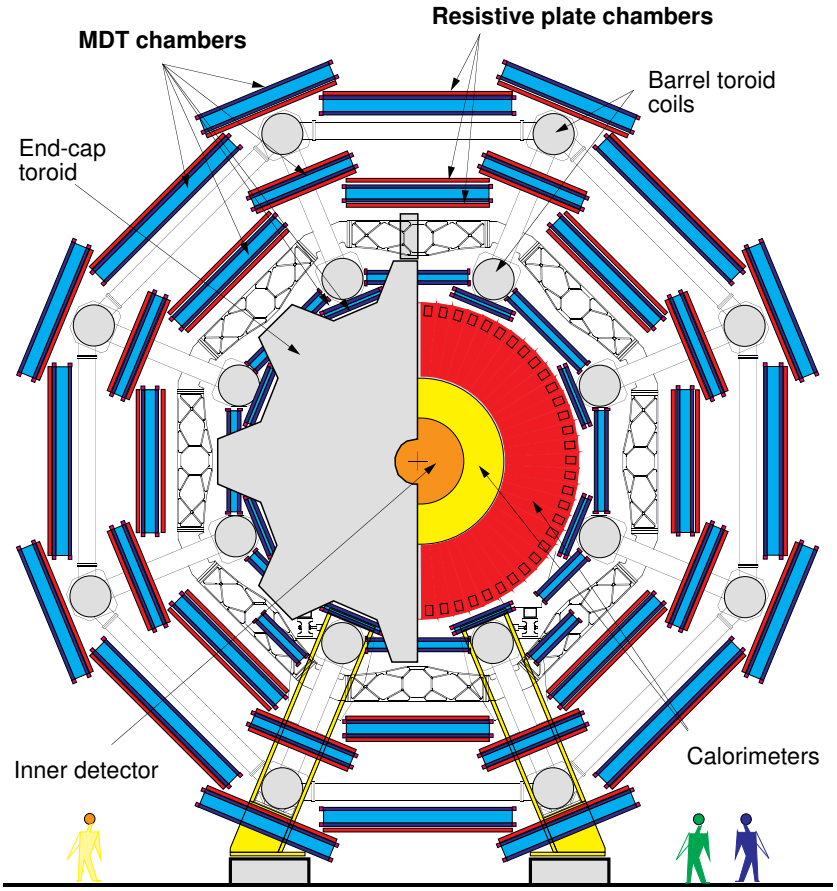

Figure 3.8 View in the x-y plane for the muon spectrometer in the barrel region.

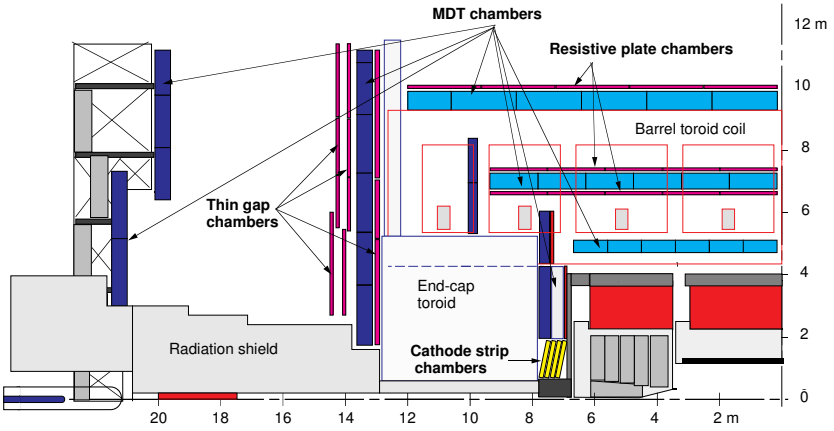

Figure 3.9 View in the R-z plane of the muon spectrometer.

Table 3.3 Summary of coverage, granularity and longitudinal segmentation of the ATLAS calorimetry system.

Presampler	**Barrel**	**Endcap**	
Coverage	$\|\eta\| < 1.52$	$1.5 < \|\eta\| < 1.8$	
Longitudinal Segmentation	one sampling	one sampling	
Granularity ($\Delta\eta \times \Delta\phi$)	0.025×0.1	0.025×0.1	
Electromagnetic Calorimeter	**Barrel**	**Endcap**	
Coverage	$\|\eta\| < 1.475$	$1.375 < \|\eta\| < 3.2$	
Longitudinal Segmentation	three samplings	three samplings	
Granularity ($\Delta\eta \times \Delta\phi$)			
1^{st} Sampling	0.003×0.1	0.025×0.1	$1.375 < \|\eta\| < 1.5$
		0.003×0.1	$1.5 < \|\eta\| < 1.8$
		0.004×0.1	$1.8 < \|\eta\| < 2.0$
		0.006×0.1	$2.0 < \|\eta\| < 2.5$
		0.1×0.1	$2.5 < \|\eta\| < 3.2$
2^{nd} Sampling	0.025×0.025	0.025×0.025	$1.375 < \|\eta\| < 1.5$
		0.1×0.1	$2.5 < \|\eta\| < 3.2$
3^{rd} Sampling	0.05×0.025	0.05×0.025	$1.5 < \|\eta\| < 2.5$
Hadronic Tile Calorimeter	**Barrel**	**Extended Barrel**	
Coverage	$\|\eta\| < 1.0$	$0.8 < \|\eta\| < 1.7$	
Longitudinal Segmentation	three samplings	three samplings	
Granularity ($\Delta\eta \times \Delta\phi$)			
1^{st} and 2^{nd} Samplings	0.1×0.1	0.1×0.1	
3^{rd} Sampling	0.2×0.1	0.2×0.1	
Hadronic Liquid-Argon Calorimeter		**Endcap**	
Coverage		$1.5 < \|\eta\| < 3.2$	
Longitudinal Segmentation		four samplings	
Granularity ($\Delta\eta \times \Delta\phi$)		0.1×0.1	$1.5 < \|\eta\| < 2.5$
		0.2×0.2	$2.5 < \|\eta\| < 3.2$
Liquid-Argon Forward Calorimeter		**Forward**	
Coverage		$3.1 < \|\eta\| < 4.9$	
Longitudinal Segmentation		three samplings	
Granularity ($\Delta\eta \times \Delta\phi$)		0.1×0.1	

good resistance against ageing, as well as a small Lorentz angle. The resolution achieved on a single wire is ~80 μm. On each chamber the tubes are arranged in two multi-layers and each of them is formed by three (for mid-

dle and outer stations) or four (for inner stations) layers of tubes, as shown in Figure 3.10.

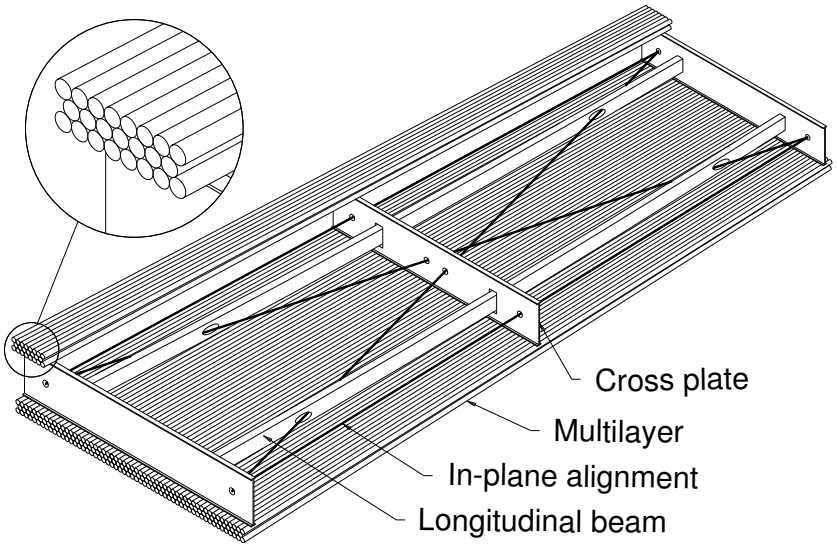

Figure 3.10 Schematic drawing of an MDT chamber.

3.6.2 Cathode strip chambers (CSC)

In the high-η region ($2.0 < |\eta| < 2.7$), MDTs are replaced by CSCs, which have a very low neutron sensitivity. The CSCs are multiwire proportional chambers with cathode strip readout. The avalanche around an anode wire from an ionization event creates an induced charge distribution on the cathode, thus allowing for a measurement of one coordinate. The other coordinate is measured with strips oriented parallel to the anode wires, which form the second cathode of the chamber.

3.6.3 Resistive plate chambers (RPC)

For trigger measurements at Level 1 (see Section 3.7) in the barrel region RPCs, operated in avalanche mode, are used. The basic unit is formed by two parallel resistive bakelite plates and between them there is a mixture of tetrafluoro-ethane ($C_2H_2F_4$) and a small component of SF_6. Each chamber is made from two detector layers and four readout strip panels: "η strips" which are

parallel to the MDT wires and "ϕ strips" which provide the second-coordinate measurement. Two layers of chambers are installed in the middle station, and provide the trigger for the low-p_T threshold. A third layer of RPC is installed on the outer chamber station, and is used, together with the other planes, for the high-p_T threshold.

3.6.4 Thin gap chambers (TGC)

These are multi-wire chambers operated in saturated mode, used in the endcap for the Level 1 muon trigger, with a 55% CO_2 and 45% n-pentane (n-C_5H_{12}) gas mixture. Their anode wires are arranged parallel to the MDT wires and provide position information together with readout strips, which are orthogonal to the wires and are also used to measure the second coordinate.

3.7 Trigger System

The ATLAS trigger and data-acquisition system (always referred to as DAQ), consists of three levels of online event selection. These selections are necessary since we expect an event rate of the order of 1 GHz but it is only possible to save data on tape at a rate which is ~100 Hz. In order to achieve this, as it is visible in Figure 3.11, the ATLAS trigger system has been organized in three different levels, with different latencies and rates.

3.7.1 Level 1 Trigger (LVL1)

The LVL1 trigger has to provide a decision in ~2 μs and thus must be operated at a hardware level, using only fast detectors [49]. For what regards muons only RPCs and TGCs are used; for what regards the calorimeter selections, these are made using reduced information from the calorimeter. The LVL1 should be able to operate at a rate of ~1 GHz and reduce it by four orders of magnitude. Trigger information, at this level, is provided for a number of of sets of p_T thresholds (which can range from 6 to 8 thresholds per object). When an event is selected by the LVL1, the information about that

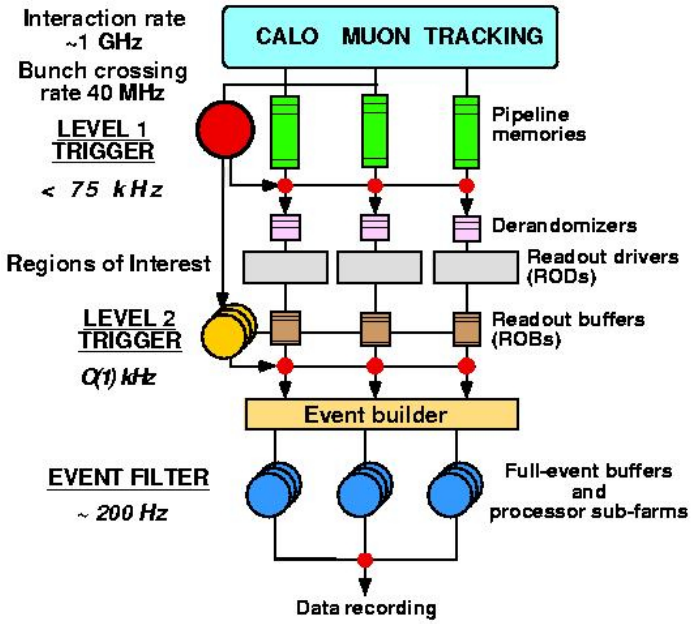

Figure 3.11 Block diagram of the Trigger/DAQ system in ATLAS.

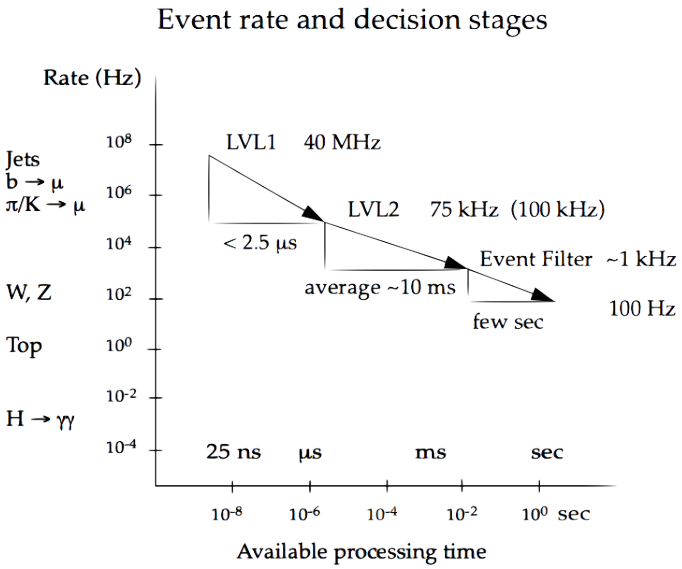

Figure 3.12 Event rate at the LHC as a function of the available processing time for the different trigger levels.

event is read out from the front-end electronics of the sub-detectors and held provisionally in readout buffers (called ROBs). If the LVL2 trigger rejects the event, the information is discarded from the ROBs, while if the LVL2 accepts the event, the different pieces of information coming from the various sub-detectors are merged and passed to the last level of decision; this is called event building.

3.7.2 Level 2 Trigger (LVL2)

The LVL2 trigger operates at a rate of ~100 kHz and consists of software algorithms that refine the decision taken at LVL1. For this reason, together with the EF, is part of the High Level Trigger of the experiment (HLT) [50]. This level does not have enough time to use the information from all the ATLAS detectors and must restrict itself to using information provided by the LVL1 in a "region of interest" (RoI). An RoI is defined as a region in the η-ϕ coordinates where the candidate object has been found by the LVL1. The LVL2 can thus exploit the full-granularity of the experiment (it can access MDT and CSC information as well as full-granularity calorimeter information), but only in this confined region, limiting the number of data processed and so the time needed for a decision. In the end, the LVL2 is expected to reduce the rate to ~1 kHz and this is usually achieved by sharpening the p_T thresholds inherited from the LVL1 or by adding isolation requirements: both things are allowed by precision measurements in MDTs and CSCs and by finer granularity in the calorimeter.

3.7.3 Event Filter Trigger (EF)

The EF must reduce the rate from ~1 kHz to the 100 kHz we can actually write on tape. At this stage, the EF has at its disposal all information from all sub-detectors and can thus perform the reconstruction of the full event in the ATLAS experiment. The EF can improve the LVL2 decision by:

- tightening the p_T thresholds with respect to LVL2;
- exploiting information about the complete detector, which was not accessible in its integrity at LVL2;

- using complex algorithms which could not run at LVL2 due to the latency limit of ~10 ms, but can run in the few seconds which are granted to the EF for decision making.

3.8 ATLAS Software and the GRID

3.8.1 Data Types in ATLAS

ATLAS has developed different data types to store information collected by the experiment, to cope with all the different studies needed for physics results as well as detector improvements and maintenance [51]. Here we will lists only the most relevant ones.

RAW Data

Raw data are the output of the EF decision and each event can reach asize of 1.6 megabytes. They represent data in "bytestream" format, as it is delivered by the detector. Thus there is no object-oriented representation in data at this stage nor any offline reconstruction.

Event Summary Data (ESD)

ESDs store information with an object-oriented format in POOL ROOT files. This information is the output of the reconstruction process and replaces Raw data in almost all cases except when particular calibration or reconstruction studies are needed. The final size of each event should be around 500 kilobytes.

Analysis Object Data (AOD)

This format is directly derived from ESD and still features an object-oriented representation. They are saved in POOL ROOT files and contain only information about physics objects, needed for physics analyses. The goal is to reduce the ESD file by a factor 5, reaching a size of ~100 kilobytes per event.

Derived Physics Data (DPD)

DPD is an n-tuple-style representation of event data for end-user analysis. The inclusion of DPD in the computing model has the aim of provid-

ing physicists with a data format suitable for direct analysis and display by means of standard analysis tools (such as ROOT), though the same results can be obtained with AOD as input. In particular, for all the studies that will be printed in this work, D3PDs have been used: they are one specific implementation of the general DPD model. The D3PD production mechanism does not introduce any data analysis but simply copies data necessary for the analysis from the AOD files (where it is stored in an object-oriented format) into flat n-tuples, without any structure.

3.8.2 ATLAS offline software: the Athena framework

The goal of the ATLAS offline software is to process all data coming from the trigger and DAQ systems and allow physicists in the ATLAS Collaboration to analyze them with specific tools. In order to achieve this, the Athena framework has been developed, starting from the pre-existing Gaudi framework used by the LHCb experiment [51]. The Athena framework is used not only for reconstructing real data from the experiment, but also for generating all Monte Carlo samples needed by the analzers [52]. The concept behind such a framework is a component-based model, which provides a very flexible infrastructure. The software has been written mainly in C++ and the configuration files are written in Python. In Figure 3.13 are represented the major components of the Athena framework, with their relationships. Among these, the most important are:

Application Manager

The Application Manager manages and coordinates the activity of all components within one application. Only one instance of the Application Manager can exist and it is shared between all applications.

Algorithms

Algorithms represent the common interface for users to deal with event loops within the Athena framework. Algorithms should perform configurable operation on the input data and generally produce some output data.

Sequencers

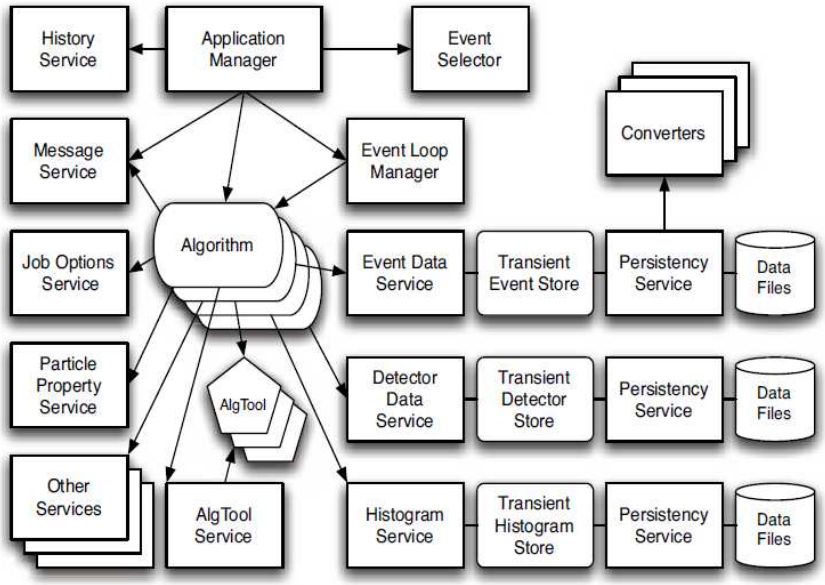

Figure 3.13 The Athena component model.

Sequencers are simply a chain of Algorithms, thus allowing for a structured analysis.

Tools

Tools have a similar structure of Algorithms with the only difference being that Tools can be called multiple times per event, while Algorithms can be called just once per event.

Job Option Service

An Algorithm or a Tool has configurable quantities that can be changed using the Job Option Service, which overwrites the default values present in the Algorithm or Tool itself.

3.8.3 The GRID infrastructure

In order to provide computing support to the experiments at the LHC, the LHC Computing Grid Project (LCG) has been approved by CERN with the goal of developing, building and maintaining a distributed computing infrastructure for data storage and analysis [53].

A traditional approach to the problem would have been to centralize all this at one location near the experiments. In the case of the LHC, however, a globally distributed model for data storage and analysis was chosen, for the following reasons:

- The significant costs of maintaining and upgrading the necessary resources for such a computing challenge are more easily handled by individual institutes and participating national organizations directly. They can fund local computing resources and retain responsibility for these, while still contributing to the global goal.

- Multiple copies of data and automatic reassigning of computational tasks to available resources ensures load balancing of resources and facilitates access to the data for all the scientists involved, avoiding single points of failure

The LCG Project has implemented the Grid in a four-tiered model:

- The original raw data which come from the ATLAS DAQ system will be recorded at the Tier-0 center at CERN. The first-pass reconstruction will also take place at the Tier-0, and a copy of these reconstructed data will be stored. The Tier-0 will distribute a second copy of the raw data across the Tier-1 centers associated with the ATLAS experiment.

- The Tier-1 centers in ATLAS have the prime responsibility for managing the permanent data storage and providing computational capacity for reprocessing, simulation and analysis processes that require access to large amounts of data.

- The role of the Tier-2 centers is to provide computational power and storage services for end-user analysis.

- Any other computing facility in a university or laboratory can take part in the processing and analysis of LHC data as a Tier-3 center.

Chapter 4

Electron Reconstruction in ATLAS

In this chapter we will cover in full detail the electron reconstruction in ATLAS. The standard electron reconstruction algorithm in ATLAS for 2010 and 2011 data acquisition periods does not account for the energy lost by the electron along the track due to bremsstrahlung [54]. Two different efforts have been undertaken in ATLAS, one to *refit* the standard tracks and improve the four-momentum of the electrons and another one to *recover* efficiency by developing dedicated reconstruction mechanisms for electrons which have radiated high energy photons and would not be reconstructed by the standard algorithm. This Chapter will describe both improvements. The author specifically contributed to the validation of the reconstruction algorithm based on the Gaussian Sum Filter model, which has significantly improved the performance of ATLAS especially for low-momentum electrons. The electron reconstruction in the region $|\eta| < 2.47$ is seeded by calorimeter deposits which are then associated to tracks in the Inner Detector. Two different aspects of the reconstruction can thus be identified: the cluster reconstruction and the matching of this cluster to one of the tracks in the Inner Detector.

4.1 EM cluster reconstruction

Electromagnetic cluster are reconstructed with a *sliding-window* algorithm, which consists in three steps: tower building, seed finding and cluster filling [55].

4.1.1 Tower building

The η-ϕ space of the EM calorimeter middle layer is divided in a grid of $n_\eta \times n_\phi = 200 \times 256$ elements, each having a size of $\Delta\eta \times \Delta\phi = 0.025 \times 0.025$, which are usually referred to as "towers". The energy of each tower is calculated by summing the energy of all the cells in all longitudinal layers of this $\Delta\eta \times \Delta\phi$ region. In case a cell extends across more than one tower, its energy is distributed among the corresponding towers considering the fractional area covered by each tower inside the cell.

4.1.2 Seed finding

The seed is looked for by creating a window of fixed size ($n_\eta \times n_\phi = 5 \times 5$) which is moved across the tower grid that we have just defined in steps of $\Delta\eta \times \Delta\phi = 0.025 \times 0.025$. For each of these possibilities, the window transverse energy is calculated (summing the transverse energy in all the cells contained in the window). If it represents a local maximum and it is above a specific threshold ($E_T{}^{\text{thr}} = 3$ GeV), a pre-cluster is formed. After this, the pre-cluster position must be determined: using a different window ($n_\eta \times n_\phi = 3 \times 3$) the energy-weighted η and ϕ barycenters of all cells around the tower at the center of the sliding window are computed.

4.1.3 Cluster filling

The last part of the algorithm must assign to the cluster all cells that are within a specific $n_\eta \times n_\phi$ window around the position of the clusters. This operation must be done for each longitudinal layer of the EM calorimeter, in this order: middle layer, strips, pre-sampler and the last layer. In order to compute the barycenter in the middle layer ($\Delta\eta_{mid}, \Delta\phi_{mid}$) we start from the pre-cluster barycenter positions ($\Delta\eta_{prec}, \Delta\phi_{prec}$) and then add all cells from the middle layer. The middle layer barycenter positions are then used as seeds for ($\Delta\eta_{strips}, \Delta\phi_{strips}$) and ($\Delta\eta_{back}, \Delta\phi_{back}$), while the barycenter positions of the strips are used as a seed for the pre-sampler ($\Delta\eta_{pres}, \Delta\phi_{pres}$). For an electron, the cluster size is $n_\eta^{cl} \times n_\phi^{cl} = 3 \times 7$ in the barrel and $n_\eta^{cl} \times n_\phi^{cl} = 5 \times 5$ in the endcap. Notice that in the barrel the cluster is particularly large in the ϕ

coordinate, since the magnetic field curves trajectories in this direction. In the endcap, instead, the size in ϕ is smaller because the effect of the bending induced by the magnetic field is less pronounced, while for the η coordinate the number of cells used is greater because the size of each cell is smaller.

4.2 The Gaussian Sum Filter algorithm

When reconstructing a charged particle in ATLAS, we can use the hits in the tracking system (explained in Section 3.4) to determine the particle's trajectory and estimate the track parameters that best describe it. These parameters are:

d_0
: This is the transverse position of the perigee, i.e. the closest distance in the x-y plane between the track and the beam line. It is also commonly referred to as impact parameter of the track.

z_0
: This is the longitudinal position of the perigee.

η
: This is the η direction of the track at the perigee.

ϕ
: This is the ϕ direction of the track at the perigee.

q/p
: This is the inverse track momentum multiplied by the charge of the particle.

In the case of muons or pions, a linear least-squares fit using a helical model (including the effect of multiple scattering) can be sufficient for fully reconstructing the trajectory. In the case of electrons, this is not completely true, since m_e = 0.511 MeV/c^2 [56], around 200 times smaller than m_μ. This means that energy losses due to bremsstrahlung are not negligible and must be taken

into account. The energy lost by a particle for bremsstrahlung has been modeled by Bethe and Heitler in 1934 [57], and according to this model the probability density function, f(z) for an electron to preserve a fraction $z = \frac{E_f}{E_i}$ of its starting energy E_i (with its final energy indicated by E_f) is given by:

$$f(z) = \frac{[-log(z)]^{a-1}}{\Gamma(a)}, \qquad a = t/log(2) \tag{4.1}$$

where t indicates the thickness of the material traversed by the electron in units of X_0. This expression is perfectly valid in case the subsequent inter-

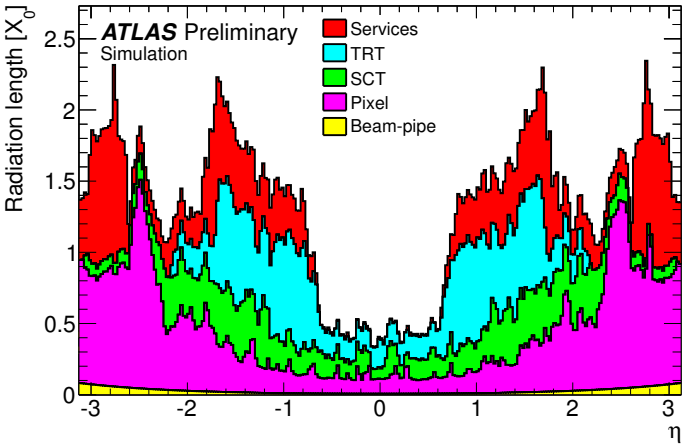

Figure 4.1 Distribution of the Inner Detector material thickness in units of radiation lengths (X_0) as a function of the pseudo-rapidity η. Each sub-detector is highlighted with a different color.

actions of the electron with the matter can be considered to be independent of each other. In the case of the experiments at the LHC, both the energies of the electrons and the material encountered by them can be very high (see Figure 4.1); this means we have to include also the Landau-Pomeranchuk-Migdal (LPM) effect [58, 59], as well as the Ter-Mikaelian effect [60]. The first one deals with the quantum interference effects arising from subsequent interaction. The second takes into account the longitudinal density of the matter. The probability density function arising from the inclusion of these two other effects does not have an analytical expression, and thus we must use a numerical implementation in a simulation program (GEANT4 [61]). Given these

conditions it is mandatory to develop a non-linear fitter which can provide optimal estimations for the track parameters. This non-linear fitter is a generalization of the Kalman Filter algorithm [62] and is usually called Gaussian Sum Filter (GSF) [63]. This algorithm has replaced the old reconstruction algorithm in ATLAS which used the pion hypothesis (thus no energy loss along the track) for all particles. The GSF algorithm has been validated on 2011 data at 7 TeV and then used in the $H \to ZZ^{(*)} \to 4\ell$ analysis for that same period [64]. In 2012 data at 8 TeV the GSF reconstruction algorithm has become the baseline algorithm and will be used by all ATLAS analyses. The assumption behind the GSF algorithm is that the trajectory state can be approximated as a weighted sum of Gaussian functions. This means that the GSF divides the experimental noise into individual Gaussian components and processes each one of them using a Kalman Filter. This yields to many Kalman Filters operating in parallel and each of them contributes to the full Bethe-Heitler spectrum. This algorithm has been designed to work using hits from the Silicon detectors of ATLAS, the Pixel and SCT shown in Section 3.4.1 and 3.4.2 but not from the TRT (see Section 3.4.3) since the use of GSF does not yield any particular improvement in this detector.

4.2.1 Validation of GSF with $Z \to ee$ events

The GSF algorithm is expected to improve the precision on the track parameters which belong to the bending plane and this has been studied first on electrons coming from the decay of a Z boson[1]. We have thus validated d_0/σ_{d_0} (where σ_{d_0} is the error on d_0 estimated by the fit itself), ϕ and q/p by comparing the reconstructed quantities from GSF and from the standard ATLAS algorithm (the one requiring pion hypothesis also for electrons) to the true quantities given by our Monte Carlo generator.

d_0/σ_{d_0}

This variable is very useful for the $H \to ZZ^{(*)} \to 4\ell$ analysis since it allows to remove the background given by electrons coming from the decays of heavy-

[1] For this validation the same kinematic range which we expect in the $H \to ZZ^{(*)} \to 4\ell$ analysis has been chosen.

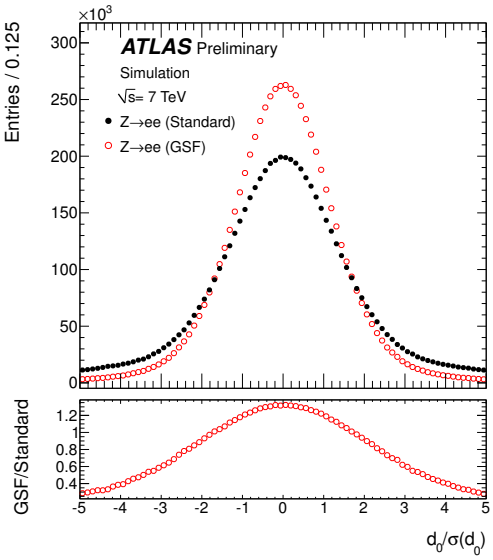

(a)

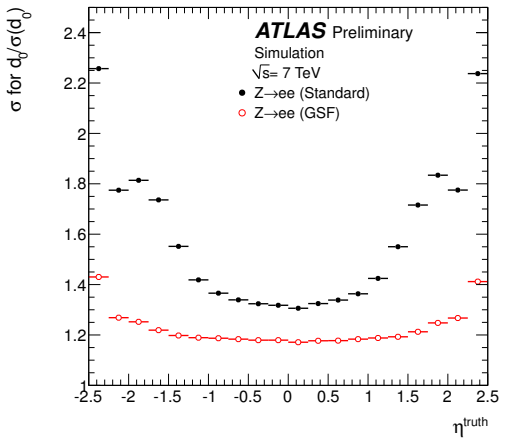

(b)

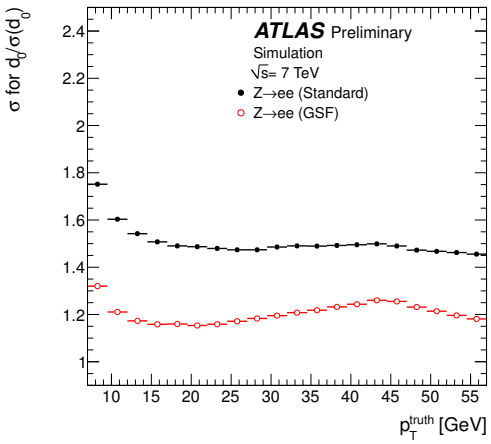

(c)

Figure 4.2 Results from validation of the d_0/σ_{d_0} variable. In 4.2a it is shown the full distribution for both GSF electrons and standard electrons. In the bottom part of the plot there is the ratio between these two. In 4.2b is shown the width of this same distribution as a function of the true electron η, while in 4.2c the same is shown as a function of the true electron p_T.

flavor quarks. In Figure 4.2a it is shown the d_0/σ_{d_0} distribution[2] for GSF and standard electrons, as well as their ratio. We also divided this distribution in bins of η^{truth} or ${p_T}^{\text{truth}}$ and computed the width of the distribution, in Figure 4.2b for what regards η^{truth} and in Figure 4.2c for what regards ${p_T}^{\text{truth}}$. The general improvement brought by the GSF algorithm is very evident and it is also worth noting that the dependence on the material crossed by the electron, as it has been shown in Figure 4.1, is considerably reduced.

ϕ

The azimuthal angle is very important when using the full four-momentum of an electron. Since the magnetic field in the tracker is solenoidal, this variable will be directly affected by it and will benefit considerably when using the GSF algorithm. As in the previous case, in Figure 4.3a it is shown the $\phi^{\text{reco}} - \phi^{\text{truth}}$ quantity for GSF and standard electrons while in Figure 4.2b and in Figure 4.2c it is shown the width of these distributions as a function of η^{truth} and ${p_T}^{\text{truth}}$ respectively. Also in this case the width of the distribution has been flattened by the GSF algorithm, which can model the different material densities much better than a simple linear fit.

q/p

The last quantity under study is the inverse of the track momentum multiplied by the charge, q/p. The variable used to verify the correct behavior of the GSF algorithm is $\frac{(q/p)^{reco} - (q/p)^{\text{truth}}}{(q/p)^{\text{truth}}}$ which shows the great improvements brought by GSF, in Figure 4.4a for the complete distribution and in Figure 4.4b and in Figure 4.4c its mean value as a function of η^{truth} and ${p_T}^{\text{truth}}$ respectively. We should note that it is practically impossible to account for all the energy that can be lost in the detector (for example if bremsstrahlung takes place in the first two layers of the Pixel detector). This yields to some remaining biases on our reconstructed variables, as it is possible to see from Figure 4.4a.

[2] Having chosen $Z \rightarrow ee$ as process for this study, the true d_0 value is zero.

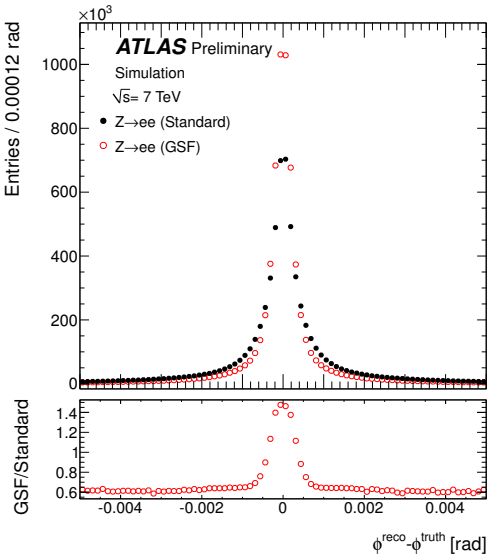

(a)

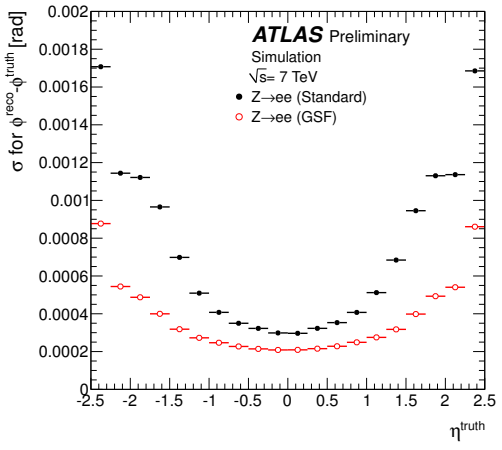

(b)

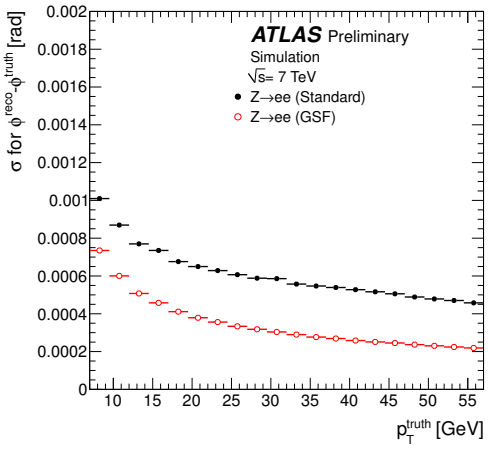

(c)

Figure 4.3 Results from validation of the ϕ variable. In 4.3a it is shown the full distribution of $\phi^{\text{reco}} - \phi^{\text{truth}}$ for both GSF electrons and standard electrons. In the bottom part of the plot there is the ratio between these two. In 4.3b is shown the width of this same distribution as a function of the true electron η, while in 4.3c the same is shown as a function of the true electron p_T.

4.2.2 J/ψ invariant mass shape

We expect the greatest improvements in the refitting of tracks to be clearly visible for electrons with E_T below 15 GeV. For this purpose, the J/ψ resonance ($m_{J/\psi}$= 3069.9 MeV [56]) represents the perfect object to test electrons at low E_T. In Figure 4.5 the invariant mass distributions for standard and GSF electrons are shown. It is clearly visible the tail on the left of the distribution, which represents the inability of the algorithm to properly account for bremsstrahlung losses. In particular this tail is much more pronounced for standard electrons, where there is no bremsstrahlung recovery at all. For GSF electrons the tail remains but it is less pronounced: this is due to those cases where the electrons radiate a considerable amount of energy in the first layers of the Pixel detector and the GSF algorithm cannot recover them. It is very important to note that the peak position is very stable with the GSF electrons, while for standard electrons its position heavily depends on the J/ψ rapidity y. Another proof of the better fitting provided by the GSF are the plots in Figure 4.6b, where we show the pull distributions for the invariant mass $(\frac{m_{e^+e^-}-m_{J/\psi}}{\delta m_{e^+e^-}})$. We would expect, for an ideal fitter, these distributions to be Gaussians with σ = 1 and mean value at zero. It is clearly visible the improvement given by the GSF electrons, which guarantee a more stable position of the peak and a better estimation of the error on the invariant mass $\delta m_{e^+e^-}$. This reflects directly on an improvement in the covariance matrix estimation which can be very useful for vertex position fits or lifetime measurements. It will also improve considerably the mass resolution for all possible resonances and this will be very important for the $H\rightarrow ZZ^{(*)}\rightarrow 4\ell$ channel, especially in the $H\rightarrow ZZ^{(*)}\rightarrow 4e$ sub-channel.

4.3 *Recovery* of electrons with hard bremsstrahlung

The GSF algorithm is not run on all tracks reconstructed by the ATLAS experiment. This is basically due to two significant facts:

1. The GSF fitting hypotheses are only valid for electrons, not for hadrons or muons. If we were to apply this reconstruction to all tracks, we could bias the tracks associated to hadrons which produce a shower of sec-

ondary particles. In this case, in fact, the GSF algorithm would try to associate to the original hadron the hits of the secondary particles which are compatible with an energy loss, thus deteriorating the initial hadron parameter estimation.

2. The GSF algorithm is a factor 10 slower than the default global χ^2 fit used in ATLAS[3] and thus for timing reasons we are forced to use it only on a set of preselected tracks, which are likely to be electrons.

While the GSF algorithm has been fully described in Section 4.2, here we will cover the changes applied for 2012 analysis in terms of the preselection of the tracks. The matching criteria are:

Simple extrapolation

Tracks are extrapolated to the second sampling of the calorimeter[4] and get selected if the difference between the extrapolated track and the cluster is smaller than 0.05 in η (for tracks with hits in the Pixel and SCT detectors), smaller than 0.05 in ϕ on the side not affected by bremsstrahlung and smaller than 0.2 in ϕ on the side affected by bremsstrahlung.

Rescaled extrapolation

Tracks can be extrapolated to the second calorimeter sampling replacing their measured momentum with the E_T measured by the cluster, in the attempt of recovering electrons which have lost a large amount of energy. We apply the same matching criteria as the previous case, with the exception that the difference in ϕ on the side affected by bremsstrahlung should be not larger than 0.1.

Another big improvement has been made in terms of track-cluster matching, when the reconstruction algorithm must find the best track for a given EM

[3] this is the default track fitter in ATLAS, which minimizes the following function:

$$\chi^2 = \sum_{hits} \frac{\Delta r^2}{\sigma^2_{hit}} + \sum_{scatters} \frac{\theta^2_{scatter}}{\sigma^2_{scatter}} + \sum_{ELoss} \frac{(\Delta E - \overline{\Delta E})^2}{\sigma^2_{\Delta E}}$$

where Δr is the track to hit residual and $\sigma_{scatter}$, $\overline{\Delta E}$ and $\sigma_{\Delta E}$ are properties of the material which is being traversed by the particle [65].

[4] this is the first sampling encountered by an electron which can provide both η and ϕ coordinate measurements, see also Section 3.5.1.

cluster. In the past this was done with simple criteria:

1. A track with at least 3 silicon hits is preferred over tracks which have less than 3 silicon hits (which are usually called TRT-only tracks).

2. If both tracks have at least 3 silicon hits, then the one having the smallest ΔR between extrapolated track and cluster barycenter is chosen.

In order to improve this part of the reconstruction, these criteria have been changed, for the 2012 data taking period, in this way:

1. A track with at least 1 Pixel hit is preferred on the other tracks, thus reducing the contamination from secondary particles.

2. In case we have at our disposal more than one track with Pixel hits, if $|\Delta R_1^{Res} - \Delta R_2^{Res}| > 0.01$ then the track with the smaller ΔR^{Res} gets selected[5].

3. In case $|\Delta R_1^{Res} - \Delta R_2^{Res}| \leq 0.01$, if $|\Delta R_1 - \Delta R_2| > 0.01$ the track with smaller ΔR is chosen.

4. In case $|\Delta R_1^{Res} - \Delta R_2^{Res}| \leq 0.01$ and $|\Delta R_1 - \Delta R_2| \leq 0.01$ we must conclude that there is no way to resolve geometrically the ambiguity between the two tracks. At this point we prefer tracks with more hits in the Pixel detector, especially if these hits are located in the first layers.

The results given by this recovery procedure are shown in Figure 4.7 where this new reconstruction strategy (in blue) is compared to the old one (in red) for both data and Monte Carlo. The improvements can reach 6-8% more efficiency in the low E_T region and also the η dependance of this efficiency is less pronounced.

[5] ΔR^{Res} is defined as the ΔR between the cluster barycenter and the extrapolated track when replacing the original track momentum with the E_T measured by the EM in the extrapolation process.

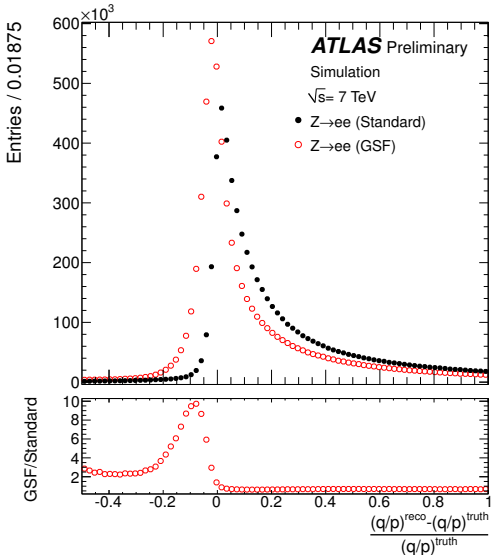

(a)

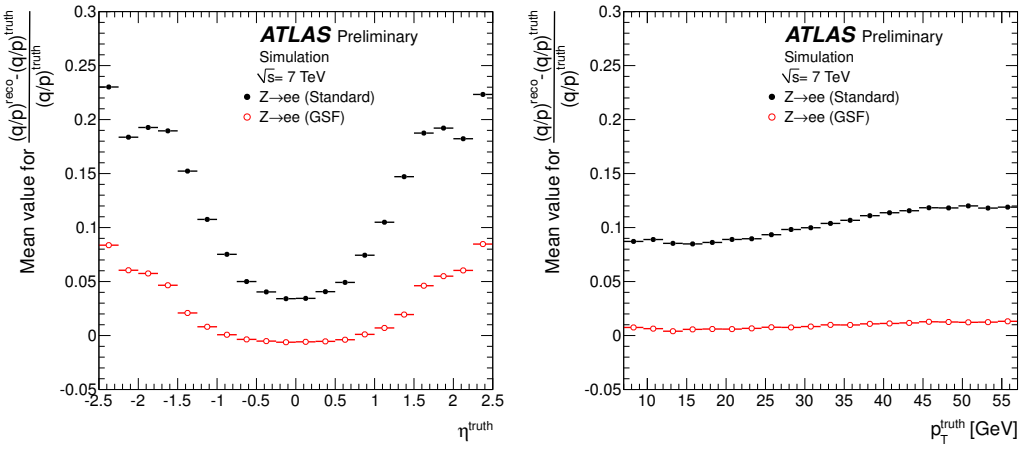

(b) **(c)**

Figure 4.4 Results from validation of the q/p variable. In 4.4a it is shown the full distribution of $\frac{(q/p)^{\text{reco}}-(q/p)^{\text{truth}}}{(q/p)^{\text{truth}}}$ for both GSF electrons and standard electrons. In the bottom part of the plot there is the ratio between these two. The GSF algorithm improves substantially our resolution in q/p but the distribution is not completely gaussian because we still have some cases where the algorithm is not able to reconstruct correctly the energy lost by the electron. In 4.4b is shown the mean of this same distribution as a function of the true electron η, while in 4.4c the same is shown as a function of the true electron p_T.

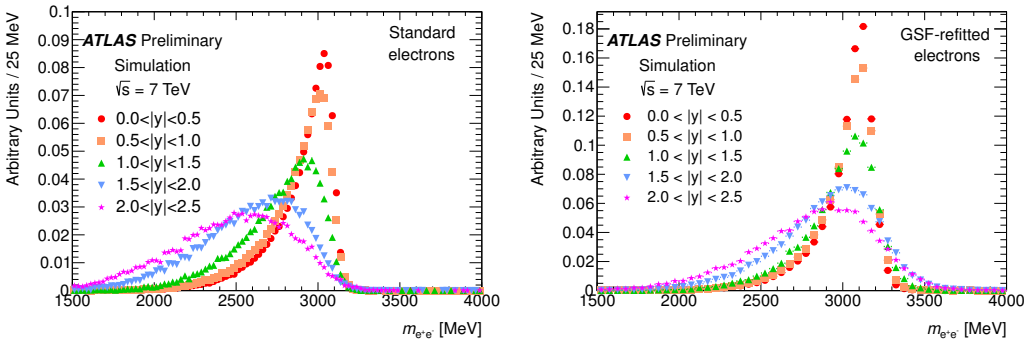

(a) Standard Reconstruction **(b)** GSF Reconstruction

Figure 4.5 Invariant mass distribution as a function of the J/ψ rapidity for the standard (4.5a) and the GSF (4.5b) reconstruction using simulated J/ψ decays to e^+e^-. The width of the distribution increases with y, but we can notice that the standard algorithm also sees a progressive shift of the peak, while the GSF algorithm maintains it close to the correct value.

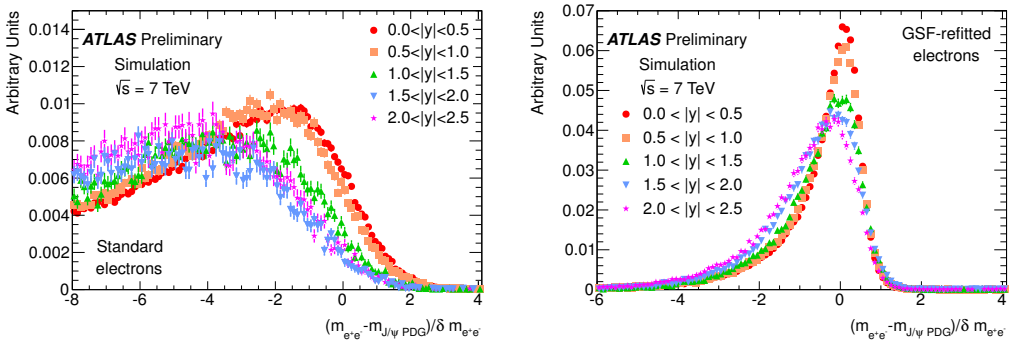

(a) Standard Reconstruction **(b)** GSF Reconstruction

Figure 4.6 Pull distribution as a function of the J/ψ rapidity for the standard (4.5a) and the GSF (4.5b) reconstruction using simulated J/ψ decays to e^+e^-. The ideal distribution would be a Gaussian with unity width and centered at zero. The tail for negative values is expected and the GSF algorithm shows a better result in reconstructing the J/ψ mass both overall and as a function of y.

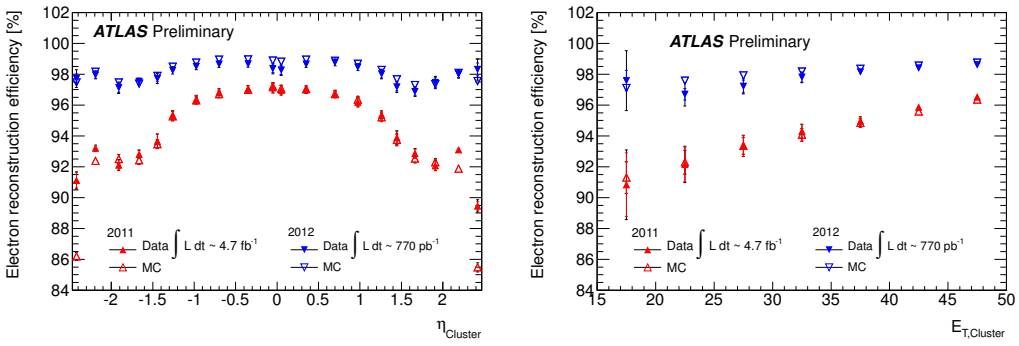

(a) **(b)**

Figure 4.7 Electron reconstruction efficiency of the old reconstruction (red) and the new reconstruction (blue) measured on data (full markers) and Monte Carlo (open markers).

Chapter 5

Electron Identification in ATLAS

Particle identification is very important at the LHC for any physics study. For example the $H \rightarrow ZZ^{(*)} \rightarrow 4e$ channel has a very low rate compared to the possible backgrounds and thus electron identification plays a very important role. In the ATLAS experiment, it has been decided to develop three working points for electron identification (called *loose*++, *medium*++ and *tight*++) which could cover all the requirements of the analyses performed by the experiment. This electron-ID menus are basically a set of rectangular cuts on variables which allow to distinguish isolated electrons from hadrons or electrons coming from semi-leptonic decays of b or c quarks. As the names suggest, the *loose*++ identification menu is the one having the highest efficiency but the lowest rejection, while the *tight*++ menu has the highest rejection but the lowest efficiency. For example, the $H \rightarrow ZZ^{(*)} \rightarrow 4e$ channel clearly needs the highest possible efficiency and thus makes use of *loose*++ electrons, while an analysis such as $W \rightarrow e\nu$ will definitely prefer a higher quality electron and will pick the *tight*++ menu. For the analysis of 2011 data, the $H \rightarrow ZZ^{(*)} \rightarrow 4\ell$ channel has used the *loose*++ menu to identify electrons, while for 2012 data, which features some changes in the reconstruction as explained in Section 4.3, the author of this thesis has developed a new working point, called *MultiLepton*, which was explicitly tailored to meet the $H \rightarrow ZZ^{(*)} \rightarrow 4\ell$ requirements. In the first section the samples used will be introduced. Then the variables used for electron identification will be explained and in the rest of the chapter the work for the *MultiLepton* menu, as well as its performance and expected impact on

the $H \to ZZ^{(*)} \to 4\ell$ analysis will be shown.

5.1 Samples used and electron categorization

The results shown in this chapter have been obtained by the analysis of D3PD samples (see Section 3.8.1), which have been produced with the official ATLAS software at $\sqrt{s}$ = 8 TeV. These are the samples:

1. A $Z \to ee$ inclusive sample generated with PYTHIA.
2. Two $H \to ZZ^{(*)} \to 4\ell$ samples, one with m_H = 120 GeV and the other with m_H = 130 GeV. At generator level there is a requirement of the four leptons to be electrons or muons with at least p_T > 5 GeV.
3. A sample containing all hard QCD processes, heavy flavor production and prompt photon production. At generator level the sum of the transverse energies of all final state particles (except muons and neutrinos) is summed in towers of $\Delta\eta \times \Delta\phi = 0.12 \times 0.12$. If one of the towers as an energy above 17 GeV the event is kept.

These samples provide a huge variety of different reconstructed electrons which could correspond to four main true objects:

Isolated electrons

These are those electrons which come directly from the decay of a Z or W boson, or from the decay of a J/ψ. These are the electrons we expect to have in case of the $H \to ZZ^{(*)} \to 4\ell$ decay channel.

Non Isolated electrons

These are real electrons and they differ from the previous case because they are produced by the semi-leptonic decay of a heavy flavor quark, c or b. These electrons will thus be produced in jets, making their identification harder.

Conversions

These are again real electrons, but in this case they come from the conversion of a photon. This is part of the background the identification

menu should try to remove, even if these objects will have characteristics which are very similar to those of the isolated electrons.

Hadrons

These are the principal background to be rejected. They are mainly $\pi^{\pm}$ which fake the electron behavior.

In order to categorize our reconstructed electrons, we used the official ATLAS tool designed for matching particles at the generator level with the reconstructed ones. In the case of electrons, which is the only one of interest in this context, the tool operates a matching between the true track and the reconstructed track.

5.2 Variables used in electron-ID

In the electron-ID process, three different kinds of variables are generally used:

- Calorimeter only variables;
- Tracking variables (hits in different sub-detectors);
- Variables which combine both calorimeter and tracker information.

In the following we will give details about each variable, showing its distribution for each of the categories explained in Section 5.1 as well as its pile-up, E_T and η dependence.

5.2.1 E_{Ratio}

The strips located in the first sampling of the calorimeter provide very good granularity in η and this is an important information since we expect electrons to generate a narrow electromagnetic shower in the calorimeter. We can take all strips with a minimal amount of energy (0.5% of the whole cluster) and find the cells which have the highest energy deposits. Using them we can construct the following variable:

$$E_{Ratio} = \frac{E_{1^{st}}^{max} - E_{2^{nd}}^{max}}{E_{1^{st}}^{max} + E_{2^{nd}}^{max}} \tag{5.1}$$

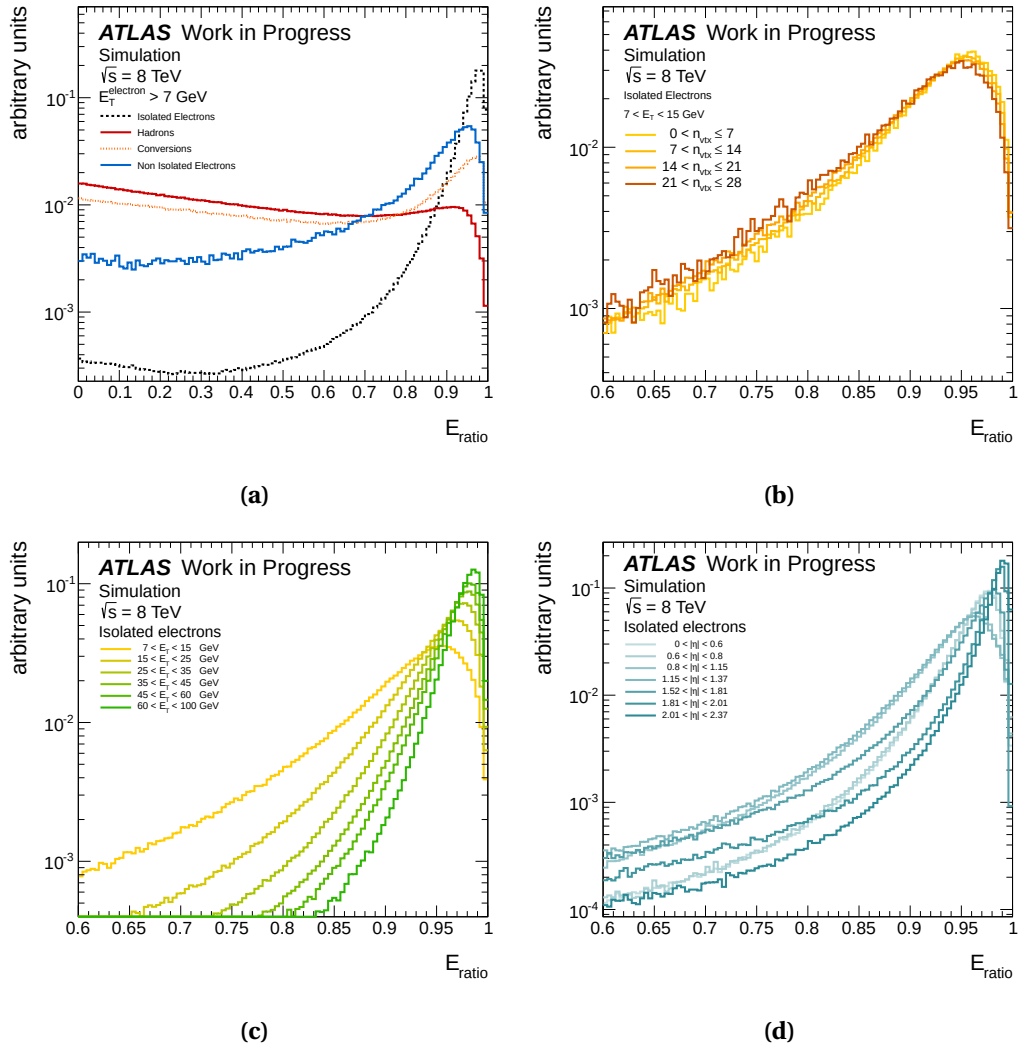

Figure 5.1 E_{Ratio} distributions. In (a) are shown the four categories (dashed black line for isolated electrons, red line for hadrons, dashed orange line for conversions and azure line for non isolated electrons) for electrons with an E_T greater than 7 GeV. In (b) it is shown the dependence of the distribution on the number of reconstructed vertices in the event, n_{vtx}, for isolated electrons with E_T between 7 and 15 GeV. In (c) it is shown the dependence of the distribution on the measured E_T and in (d) on the measured η, for isolated electrons only.

which is thus defined between 0 and 1. Electrons should cluster around 1 (having just one strip with a high deposit) and all the backgrounds will have

higher tails towards 0. This is clearly visible in Figure 5.1a where all the four categories have been included. In Figure 5.1c it is possible to see how the distribution of E_{Ratio} shifts towards 1 as the energy of the EM cluster increases, for isolated electrons only. Finally, in Figure 5.1b, the pile-up dependence is shown for isolated electrons having an E_T between 7 and 15 GeV[1]. As n_{vtx} increases, the mean of the distribution shifts to lower values as we expect since the noise in the calorimeter gets larger. The dependence on the amount of pile-up is anyway very small. We must note that this variable can be used only where strips are available, thus in the regions $1.37 < |\eta| < 1.52$ and $2.37 < |\eta| < 2.47$ there will not be any use of E_{Ratio}. In Figure 5.1d the effect of the position in the detector on the variable is clearly visible.

5.2.2 w_{stot}

The total shower width in the first layer of the calorimeter can also be used, providing a different information with respect to the one given by E_{Ratio}. If i is the strip number and i_{max} is the strip number of the cell with the highest energy deposit we can define, using 40 strips in η:

$$w_{\text{stot}} = \frac{\sum_i E_i \times (i - i_{max})}{\sum_i E_i} \tag{5.2}$$

Results for the w_{stot} variable are visible in Figure 5.2: in particular, as one can notice from Figure 5.2a, isolated electrons will show a narrower cluster than all other components, in particular hadrons. Higher energy electrons will feature narrower clusters and also a narrower distribution of w_{stot}, as shown in Figure 5.2c. The pile-up tends to enlarge the w_{stot} distribution but its effect is very small and almost invisible in Figure 5.2b. As for E_{Ratio}, the regions $1.37 < |\eta| < 1.52$ and $2.37 < |\eta| < 2.47$ do not have strips and thus we cannot use this variable in these two parts of the detector. Moreover, as it is shown in Figure 5.2d, changing the detector region changes dramatically the w_{stot} variable.

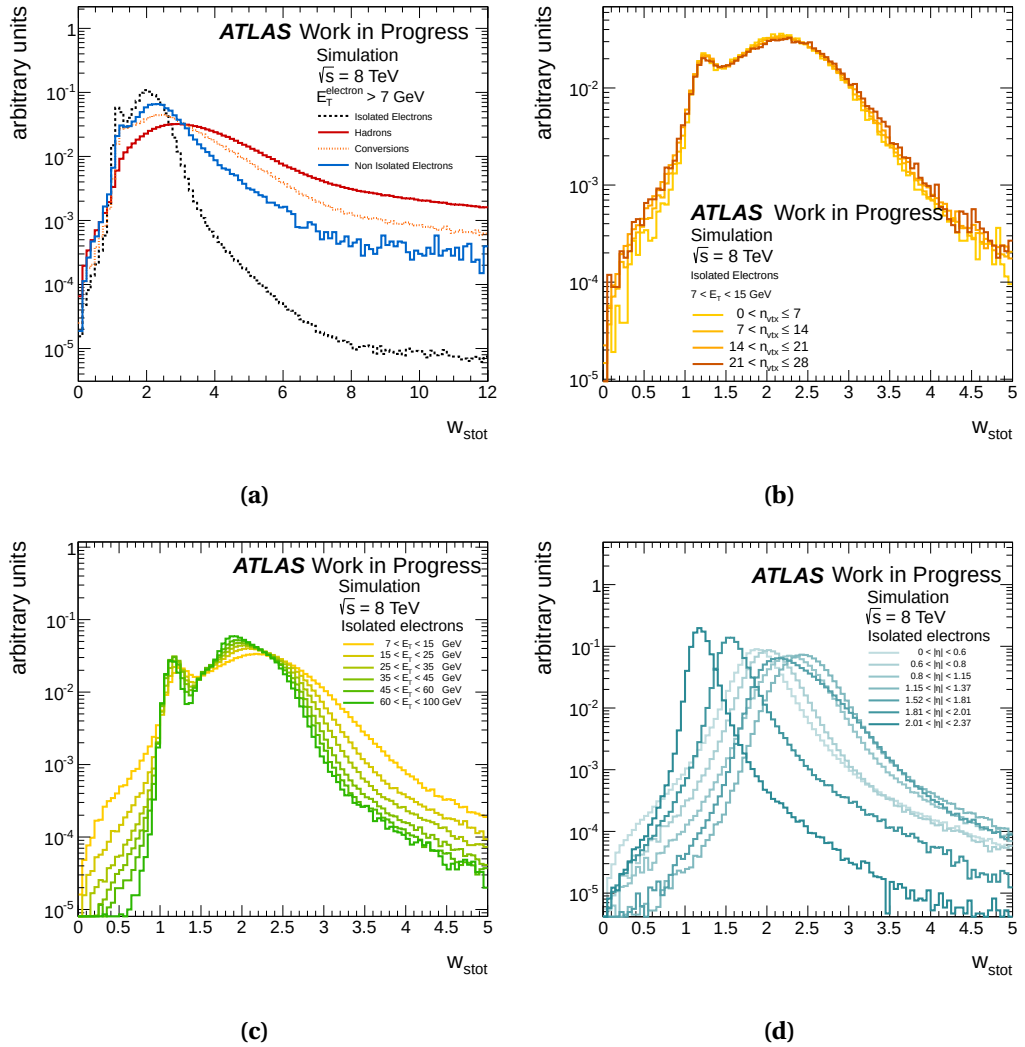

Figure 5.2 w_{stot} distributions. In (a) are shown the four categories (dashed black line for isolated electrons, red line for hadrons, dashed orange line for conversions and azure line for non isolated electrons) for electrons with an E_T greater than 7 GeV. In (b) it is shown the dependence of the distribution on the number of reconstructed vertices in the event, n_{vtx}, for isolated electrons with E_T between 7 and 15 GeV. In (c) it is shown the dependence of the distribution on the measured E_T and in (d) on the measured η, for isolated electrons only.

5.2.3 R_η

Using information of the second layer of the calorimeter, we can construct a variable that represents the energy containment in the η direction:

$$R_\eta = \frac{E_{3\times7}}{E_{7\times7}} \tag{5.3}$$

[1] the effect is more visible for low E_T electrons and we wanted to remove the E_T dependence to show only the effect of pile-up.

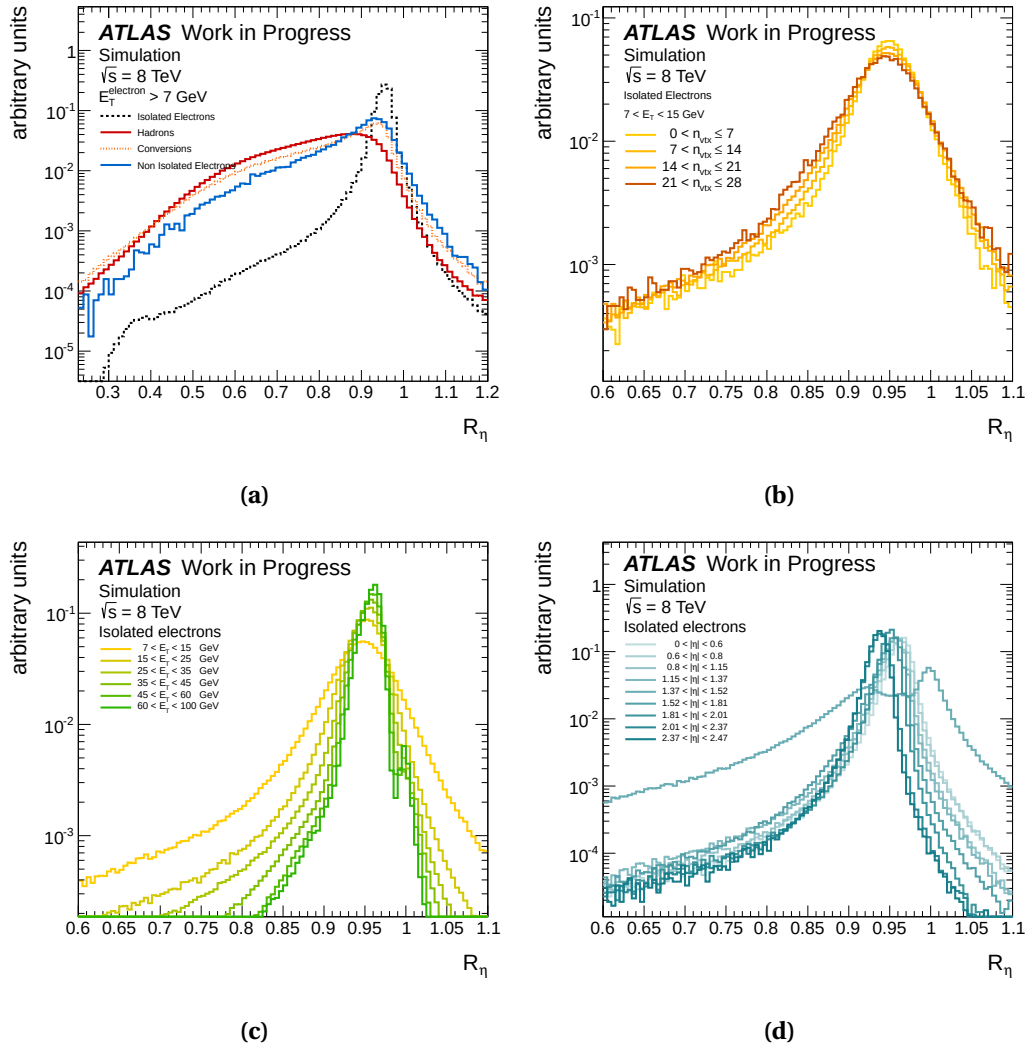

Figure 5.3 R_η distributions. In (a) are shown the four categories (dashed black line for isolated electrons, red line for hadrons, dashed orange line for conversions and azure line for non isolated electrons) for electrons with an E_T greater than 7 GeV. In (b) it is shown the dependence of the distribution on the number of reconstructed vertices in the event, n_{vtx}, for isolated electrons with E_T between 7 and 15 GeV. In (c) it is shown the dependence of the distribution on the measured E_T and in (d) on the measured η, for isolated electrons only.

where $E_{3\times7}$ is the energy contained in a 3×7 cluster ($\Delta\eta\times\Delta\phi = 0.075\times0.175$) and $E_{7\times7}$ is the energy contained in a 7×7 cluster ($\Delta\eta\times\Delta\phi = 0.175\times0.175$). The

small lateral leakage expected for isolated electrons is shown in Figure 5.3a where it is also clear that hadrons, conversions and non isolated electrons will show a wider cluster (which translates into smaller values of R_η). The E_T dependence of this variable is prominent (see Figure 5.3c), as it is its η dependence. A higher calorimeter noise, directly correlated to higher number of vertices in the event, tends to decrease R_η's discrimination power as we can see from Figure 5.3d.

5.2.4 $w_{\eta 2}$

The lateral width of the shower can be computed also for the second layer of the EM calorimeter (in a 3×5, $\Delta\eta \times \Delta\phi = 0.075 \times 0.125$, cluster):

$$w_{\eta 2} = \sqrt{\frac{\sum_i E_i \times \eta_i^2}{\sum_i E_i} - \left(\frac{\sum_i E_i \times \eta_i}{\sum_i E_i}\right)^2} \tag{5.4}$$

where E_i is the energy and η_i the η position of the i-th cell. The behavior of the four different components is exactly as expected (see Figure 5.4a), with isolated electrons providing clusters which are more contained than the other types of reconstructed electrons. One important thing to notice is that the effect of pile-up is very small on this variable, as visible in Figure 5.4b. E_T and η dependent distributions for $w_{\eta 2}$ are shown respectively in Figure 5.4c and 5.4d.

5.2.5 f_3

The last sampling of the EM calorimeter can be used to identified electrons, since they should have left all their energy in the first two samplings of the calorimeter. We can thus build a variable such as:

$$f_3 = \frac{E^{3^{\text{rd}}\text{sampling}}}{E_T} \tag{5.5}$$

which will show a narrow peak around zero for isolated electrons. Also the other components will peak at $f_3 = 0$, but their tails will be larger, especially the one for hadrons, which do not loose all their energy in the second sampling of the EM calorimeter. The effect induced by pile-up on this variable is quite

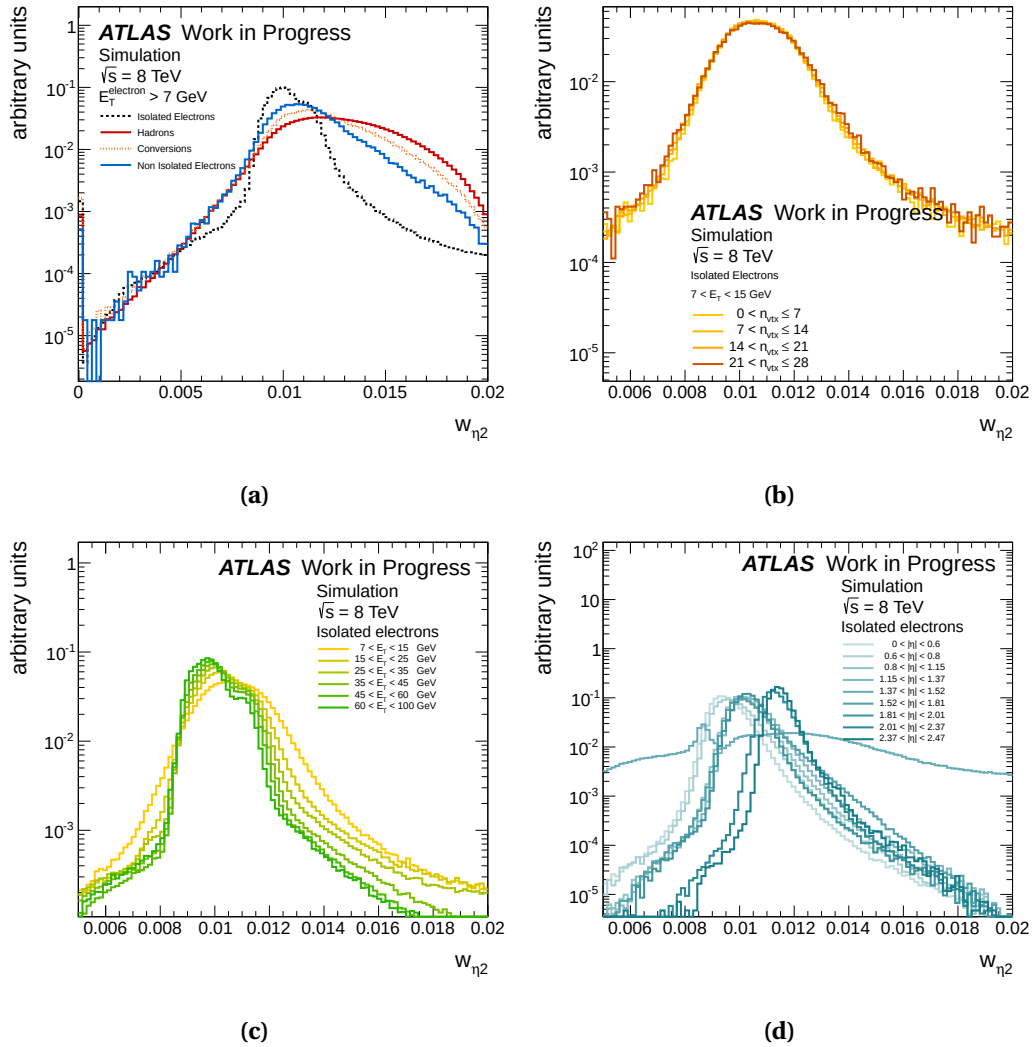

Figure 5.4 $w_{\eta 2}$ distributions. In (a) are shown the four categories (dashed black line for isolated electrons, red line for hadrons, dashed orange line for conversions and azure line for non isolated electrons) for electrons with an E_T greater than 7 GeV. In (b) it is shown the dependence of the distribution on the number of reconstructed vertices in the event, n_{vtx}, for isolated electrons with E_T between 7 and 15 GeV. In (c) it is shown the dependence of the distribution on the measured E_T and in (d) on the measured η, for isolated electrons only.

small (see Figure 5.5b), while the effect given by E_T and η must be taken into account (see Figure 5.5c and 5.5d).

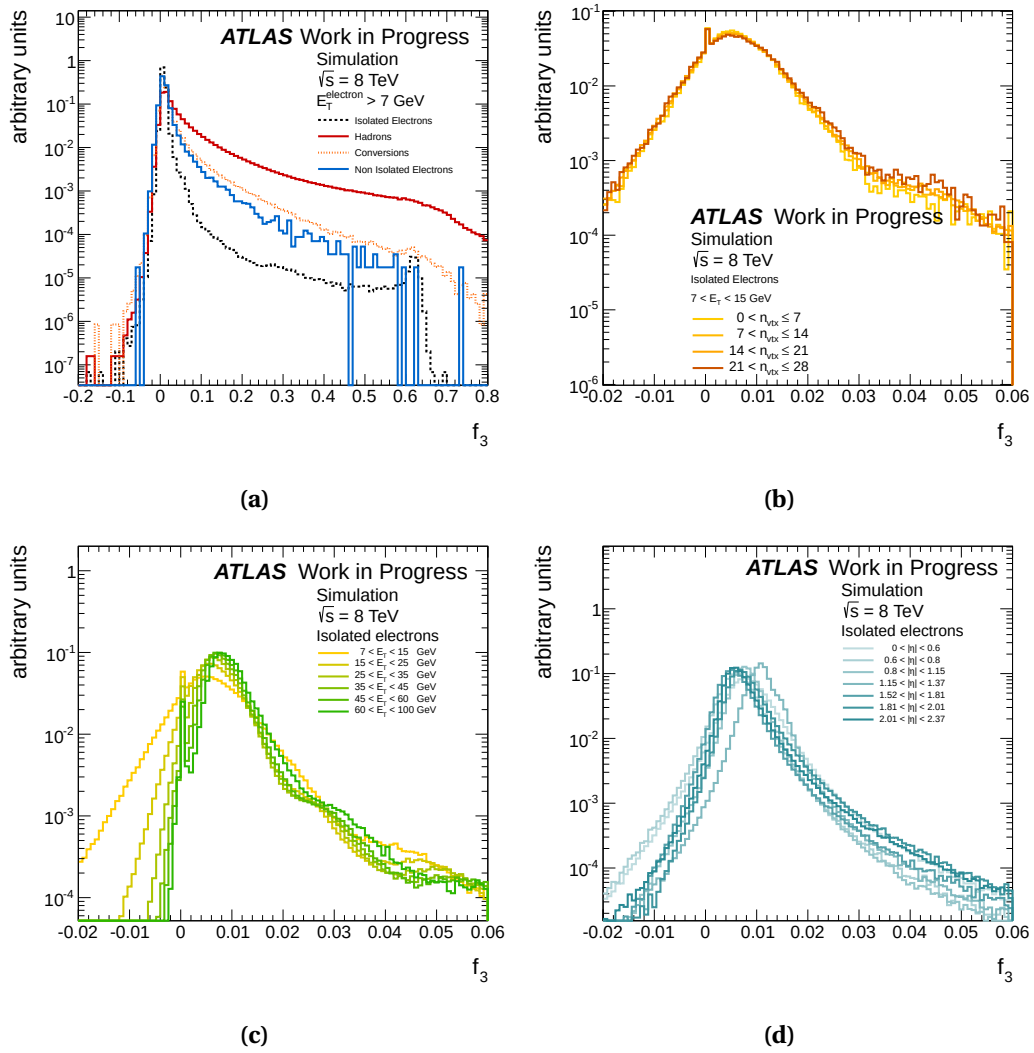

Figure 5.5 f_3 distributions. In (a) are shown the four categories (dashed black line for isolated electrons, red line for hadrons, dashed orange line for conversions and azure line for non isolated electrons) for electrons with an E_T greater than 7 GeV. In (b) it is shown the dependence of the distribution on the number of reconstructed vertices in the event, n_{vtx}, for isolated electrons with E_T between 7 and 15 GeV. In (c) it is shown the dependence of the distribution on the measured E_T and in (d) on the measured η, for isolated electrons only.

5.2.6 R_{had}

The energy deposited in the hadronic calorimeter is a very powerful tool to discriminate between electrons and hadrons. The variable we use is the en-

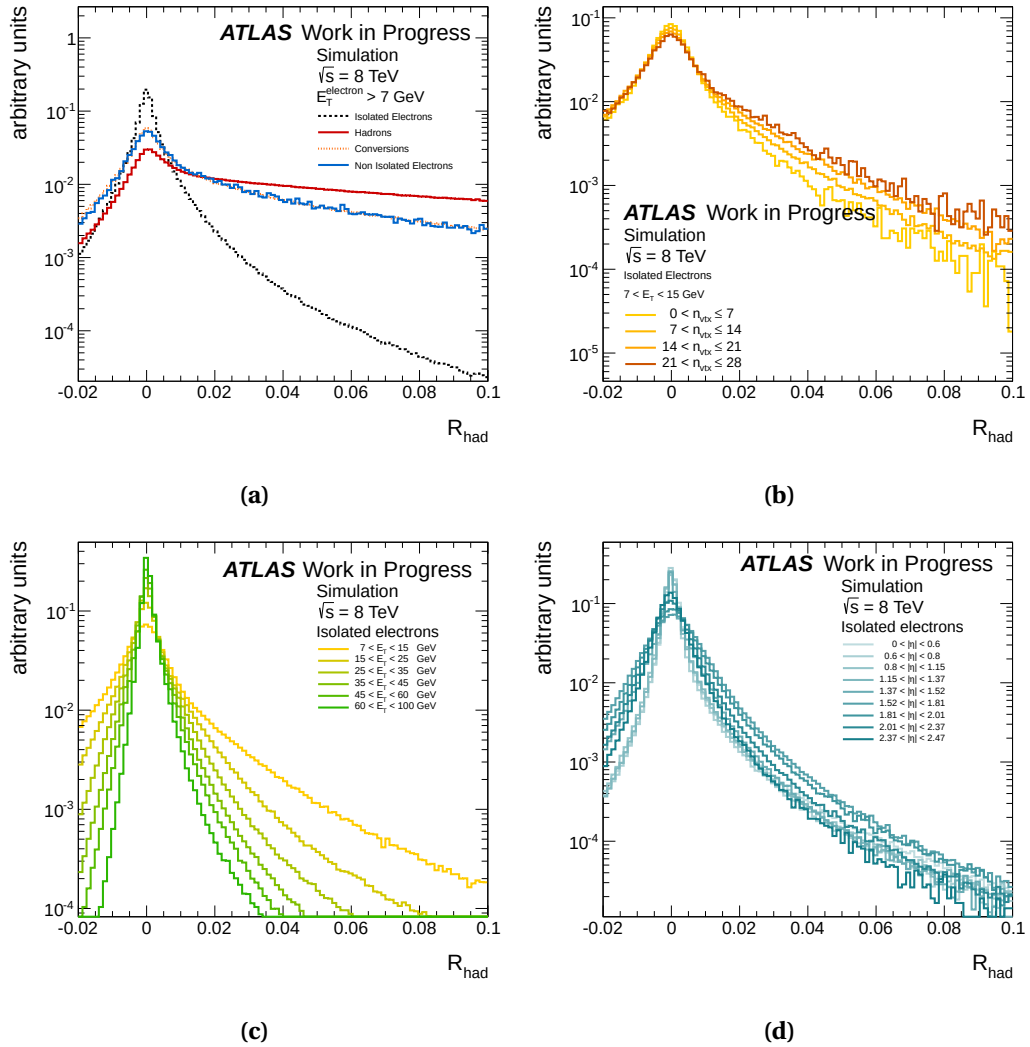

Figure 5.6 R_{had} distributions. In (a) are shown the four categories (dashed black line for isolated electrons, red line for hadrons, dashed orange line for conversions and azure line for non isolated electrons) for electrons with an E_T greater than 7 GeV. In (b) it is shown the dependence of the distribution on the number of reconstructed vertices in the event, n_{vtx}, for isolated electrons with E_T between 7 and 15 GeV. In (c) it is shown the dependence of the distribution on the measured E_T and in (d) on the measured η, for isolated electrons only.

ergy in the first sampling of the hadronic calorimeter (when available) divided

by the E_T of the cluster, as follows:

$$R_{had} = \frac{E_T{}^{had}(1^{st})}{E_T} \quad (|\eta| < 0.8 \text{ and } |\eta| > 1.37) \tag{5.6}$$

$$R_{had} = \frac{E_T{}^{had}}{E_T} \quad (0.8 < |\eta| < 1.37) \tag{5.7}$$

As we can see from Figure 5.6a, all components will have a distribution peaked at $R_{had} = 0$ but the isolated electrons will feature a very small tail, unlike the other ones. This makes R_{had} probably the best variable for discarding hadrons, exactly as one would expect, but its behavior with increasing pile-up, shown in Figure 5.6b, makes it also the most delicate one. The E_T and η dependent distributions are as expected, with narrower shapes for the barrel and for high-E_T electrons (see Figure 5.6c and 5.6d).

5.2.7 E/p

A variable which has always been used in high energy physics for electron identification is the ratio between the electron energy and momentum, E/p. In the case of the ATLAS experiment, the large quantity of material deteriorates the discrimination power provided by E/p (see Figure 5.7a), which is then used in identification menus requiring a very pure electron. There is no change in the E/p shape caused by pile-up, as it is visible in Figure 5.7b, and the effect of different E_T is very limited, shown in Figure 5.7c. Remarkable differences can be spotted in Figure 5.7d between the E/p distribution in barrel and endcap: this is due to the larger quantity of material which an electron going into the endcap has to pass through.

5.2.8 $\Delta\eta_1$

Among the variables used for track-cluster matching, the one called $\Delta\eta_1$ represents the difference between the η of the EM cluster and the η of the track extrapolated to the first sampling of the calorimeter. As we can see in Figure 5.8a, isolated electrons will show a narrow distribution peaked at $\Delta\eta_1 = 0$, while non isolated electrons, conversions and hadrons will show the same central value but much higher tails. A symmetric cut on such a variable can thus be very powerful for an electron identification menu. Another

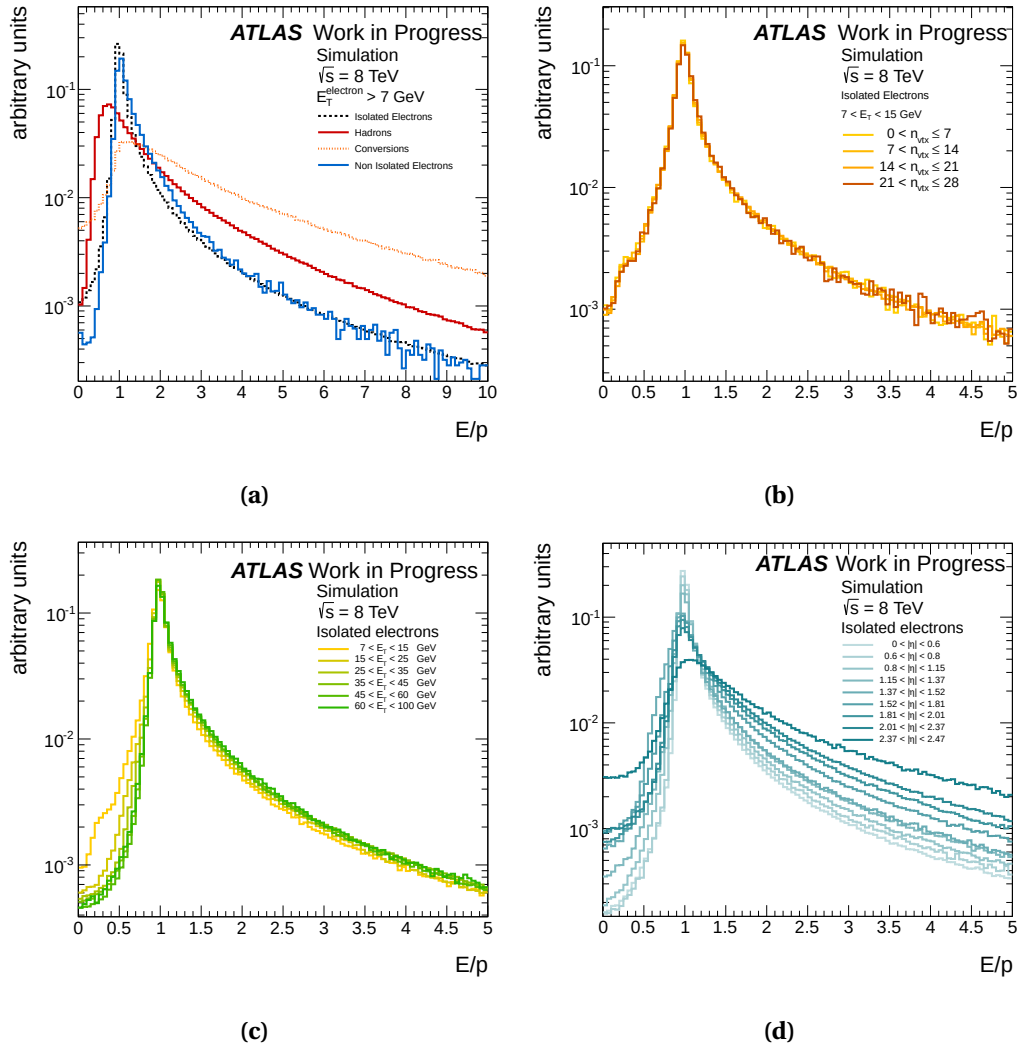

Figure 5.7 E/p distributions. In (a) are shown the four categories (dashed black line for isolated electrons, red line for hadrons, dashed orange line for conversions and azure line for non isolated electrons) for electrons with an E_T greater than 7 GeV. In (b) it is shown the dependence of the distribution on the number of reconstructed vertices in the event, n_{vtx}, for isolated electrons with E_T between 7 and 15 GeV. In (c) it is shown the dependence of the distribution on the measured E_T and in (d) on the measured η, for isolated electrons only.

feature of $\Delta\eta_1$ is its almost absent pile-up dependence as we can see in Figure 5.8b. Finally, in Figure 5.8c and 5.8d are shown the different $\Delta\eta_1$ shapes

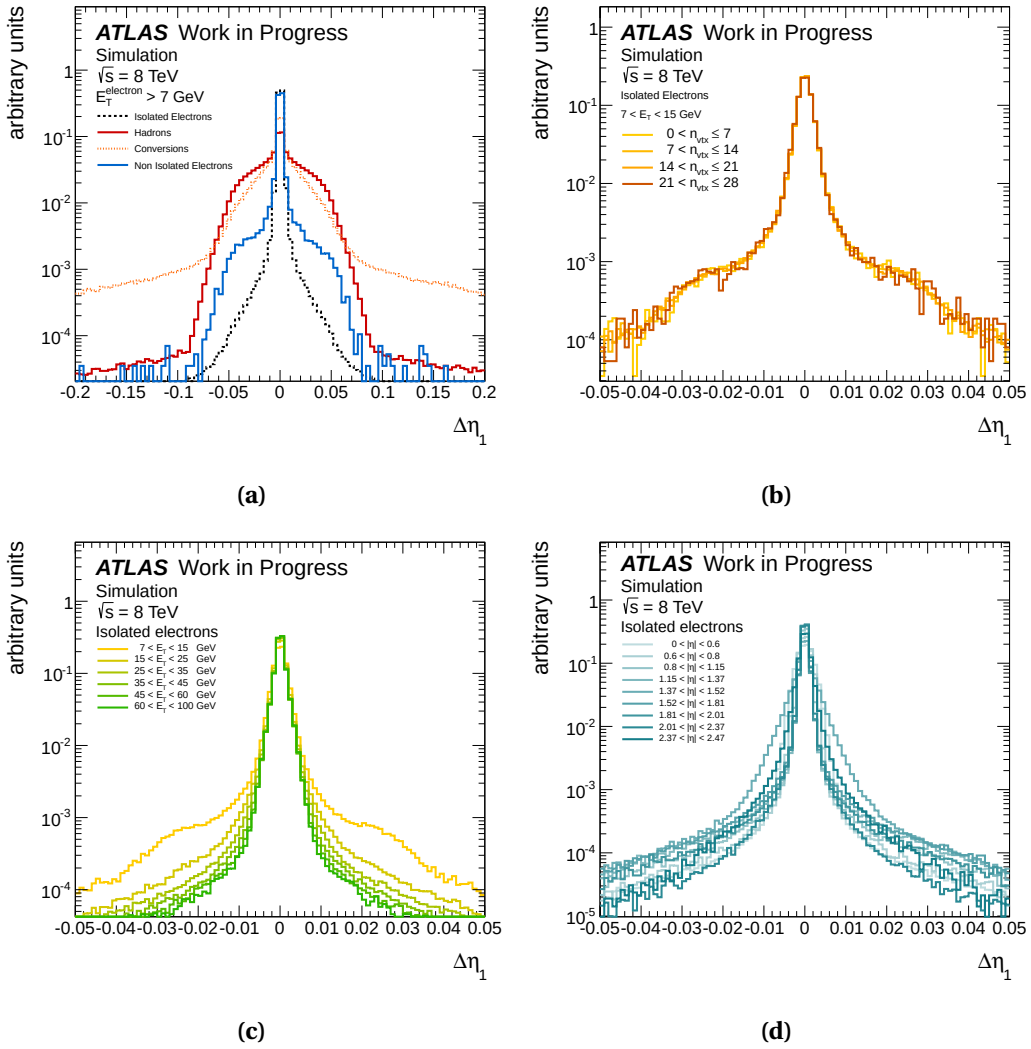

Figure 5.8 $\Delta\eta_1$ distributions. In (a) are shown the four categories (dashed black line for isolated electrons, red line for hadrons, dashed orange line for conversions and azure line for non isolated electrons) for electrons with an E_T greater than 7 GeV. In (b) it is shown the dependence of the distribution on the number of reconstructed vertices in the event, n_{vtx}, for isolated electrons with E_T between 7 and 15 GeV. In (c) it is shown the dependence of the distribution on the measured E_T and in (d) on the measured η, for isolated electrons only.

as a function of E_T and η respectively: the narrowing of the distribution with increasing E_T is as expected.

5.2.9 $\Delta\phi_2$

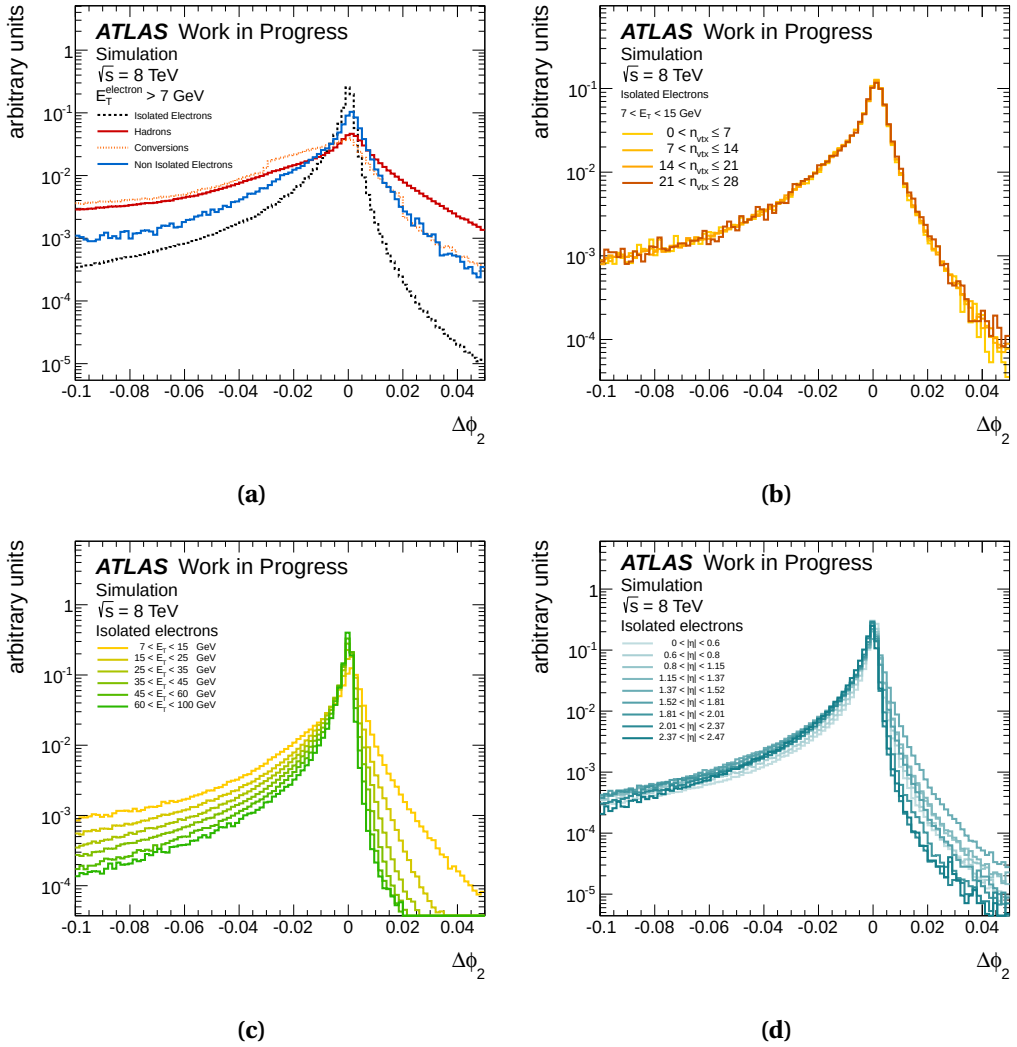

Figure 5.9 $\Delta\phi_2$ distributions. In (a) are shown the four categories (dashed black line for isolated electrons, red line for hadrons, dashed orange line for conversions and azure line for non isolated electrons) for electrons with an E_T greater than 7 GeV. In (b) it is shown the dependence of the distribution on the number of reconstructed vertices in the event, n_{vtx}, for isolated electrons with E_T between 7 and 15 GeV. In (c) it is shown the dependence of the distribution on the measured E_T and in (d) on the measured η, for isolated electrons only.

The second variable used for track-cluster matching is $\Delta\phi_2$, which is de-

fined as the difference between the ϕ of the EM cluster and the ϕ of the track extrapolated to the second layer of the EM calorimeter.[2] In Figure 5.9a is shown the distribution of $\Delta\phi_2$ for isolated and non isolated electrons, as well as for conversions and hadrons. The distribution is not symmetrical and this is due to the fact that, when extrapolating, we use the momentum measured in the tracking system which, as already explained in Section 4.2.2, tends to underestimate the real momentum of the electron. Once again it is important to note that $\Delta\phi_2$'s shape does not change with n_{vtx} (see Figure 5.9b) while it changes with E_T (Figure 5.9c) and with η (Figure 5.9d), as one would expect.

5.2.10 $\Delta\phi_{Res}$

The last track-cluster matching variable useful for electron identification is the so called $\Delta\phi_{Res}$, defined as $\Delta\phi_2$ but with a difference in the extrapolation procedure. In this case, in fact, the momentum of the track is replaced by the energy measured in the cluster and then the extrapolation is performed. The distribution for all the different sets of reconstructed electron is shown in Figure 5.10a, while $\Delta\phi_{Res}$ as a function of n_{vtx}, E_T and η is shown respectively in Figure 5.10b, 5.10c and 5.10d. These plots show a behavior which is very similar to the one of $\Delta\phi_2$, with the only difference given by the more symmetrical distribution around $\Delta\phi_{Res} = 0$, due to the use of the EM cluster energy instead of the track momentum.

5.2.11 TRT_{Ratio}

As already stated in Section 3.4.3, we can use the fraction of hits in the TRT which are above a certain threshold to discriminate between an electromagnetic object and a hadron. As we can see from Figure 5.11a the electromagnetic objects, isolated and non isolated electrons as well as conversions, will all have a higher fraction of hits above threshold with respect to hadrons. This variable, being based on hits in the Inner Detector, does not show any striking difference in bins of n_{vtx} (Figure 5.11b), E_T (Figure 5.11c) or η (Figure 5.11d).

[2] the first layer does not provide information about the ϕ coordinate, and thus in this case we are forced to extrapolate to the second layer.

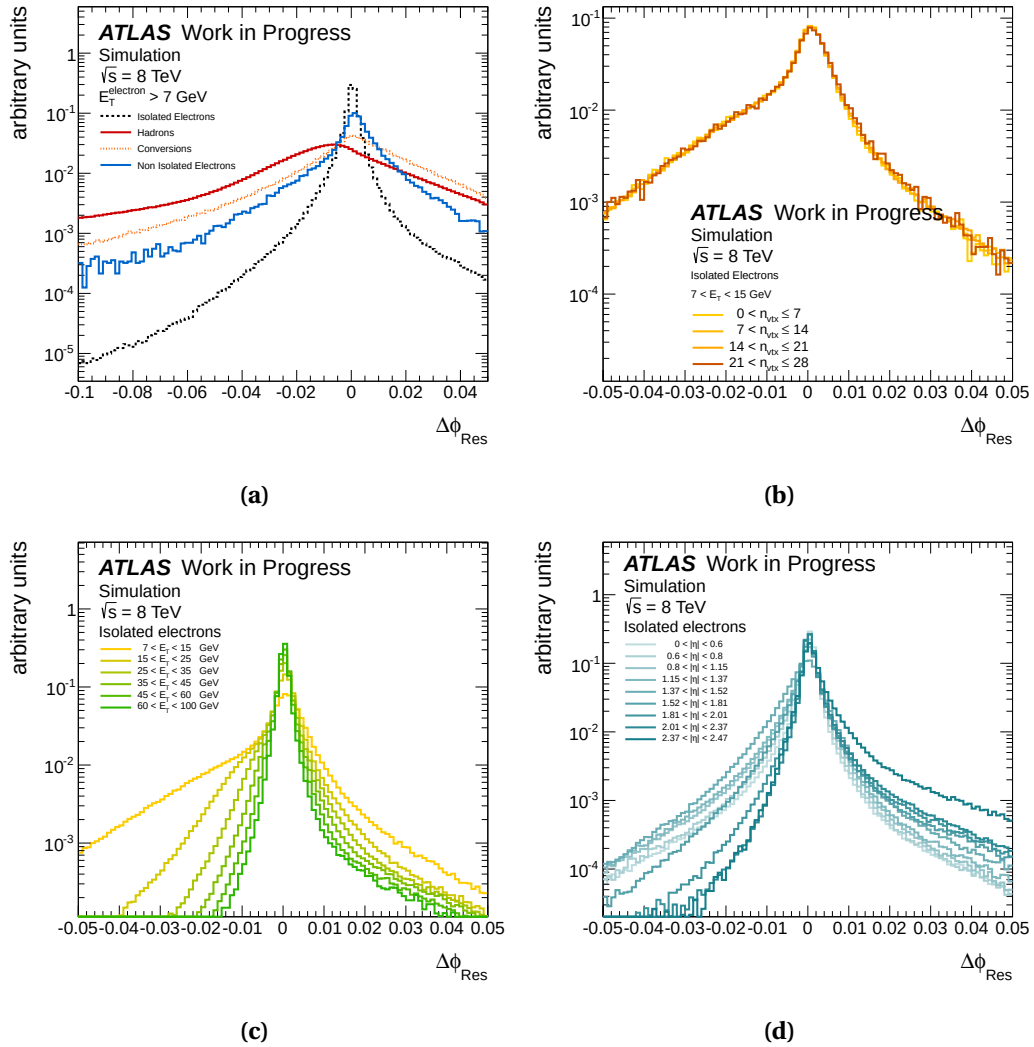

Figure 5.10 $\Delta\phi_{Res}$ distributions. In (a) are shown the four categories (dashed black line for isolated electrons, red line for hadrons, dashed orange line for conversions and azure line for non isolated electrons) for electrons with an E_T greater than 7 GeV. In (b) it is shown the dependence of the distribution on the number of reconstructed vertices in the event, n_{vtx}, for isolated electrons with E_T between 7 and 15 GeV. In (c) it is shown the dependence of the distribution on the measured E_T and in (d) on the measured η, for isolated electrons only.

5.2.12 Δp/p

The new electron reconstruction made with the GSF algorithm, allows us to know the momentum of the electron track both at the perigee and at the

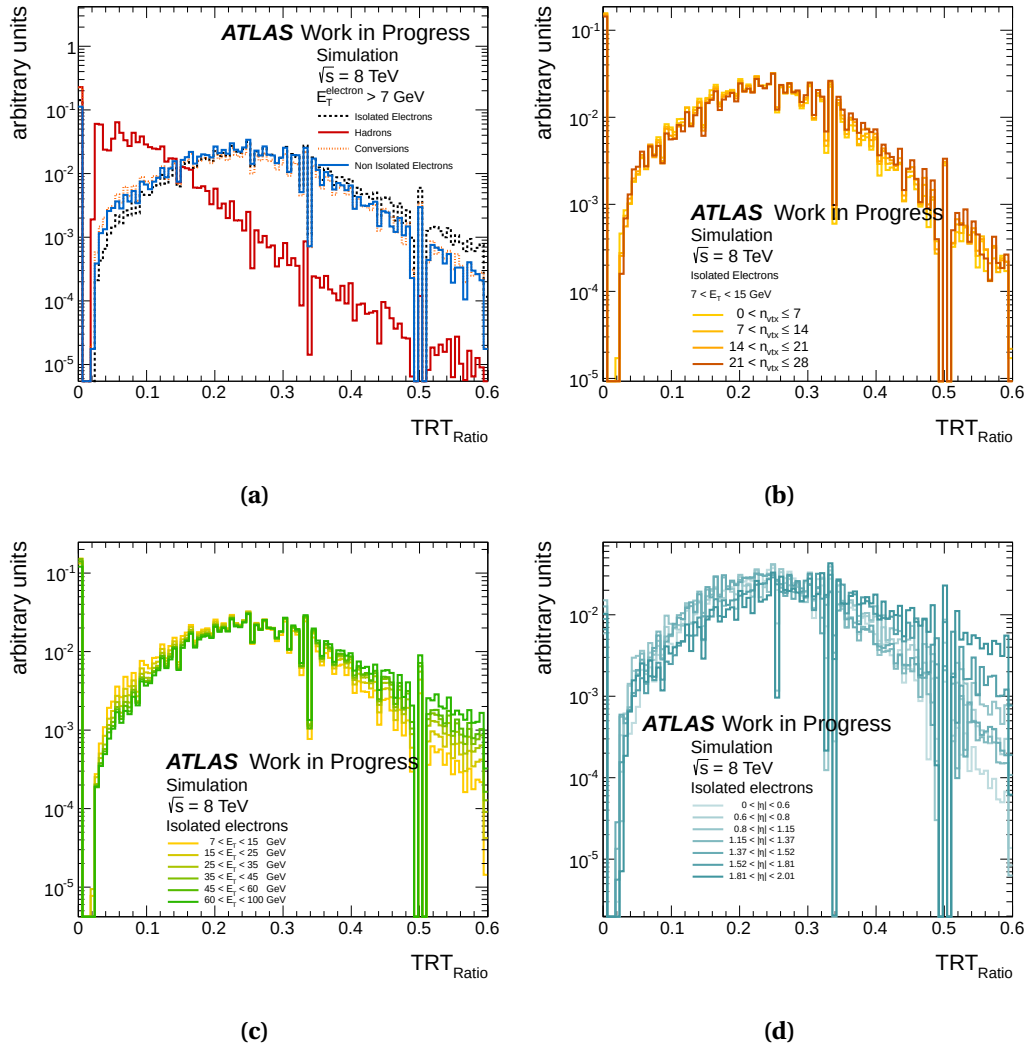

Figure 5.11 TRT_{Ratio} distributions. In (a) are shown the four categories (dashed black line for isolated electrons, red line for hadrons, dashed orange line for conversions and azure line for non isolated electrons) for electrons with an E_T greater than 7 GeV. In (b) it is shown the dependence of the distribution on the number of reconstructed vertices in the event, n_{vtx}, for isolated electrons with E_T between 7 and 15 GeV. In (c) it is shown the dependence of the distribution on the measured E_T and in (d) on the measured η, for isolated electrons only.

exit of the Inner Detector. Using these information, we can compute a variable

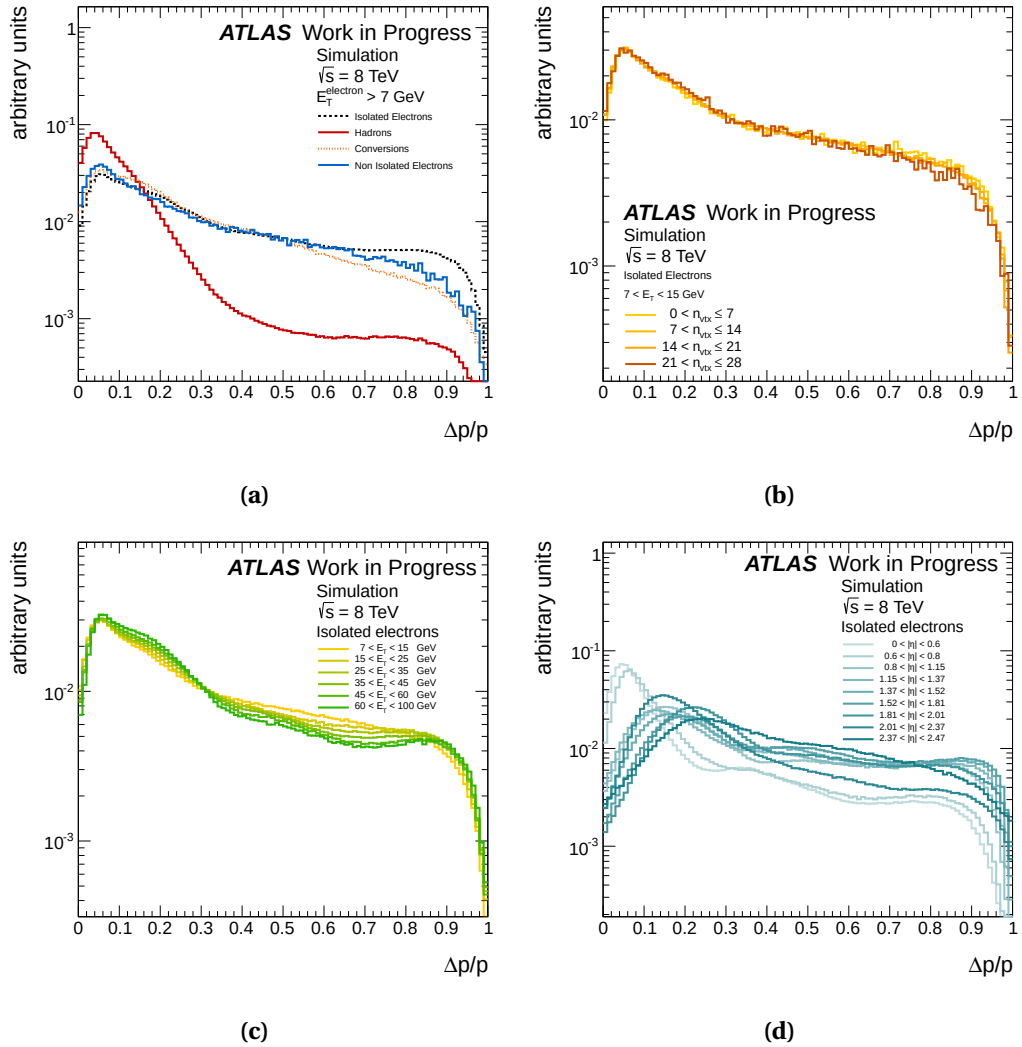

Figure 5.12 Δp/p distributions. In (a) are shown the four categories (dashed black line for isolated electrons, red line for hadrons, dashed orange line for conversions and azure line for non isolated electrons) for electrons with an E_T greater than 7 GeV. In (b) it is shown the dependence of the distribution on the number of reconstructed vertices in the event, n_{vtx}, for isolated electrons with E_T between 7 and 15 GeV. In (c) it is shown the dependence of the distribution on the measured E_T and in (d) on the measured η, for isolated electrons only.

which accounts for the momentum lost by the electron along the track:

$$\Delta p/p = \frac{p^{\text{initial}} - p^{\text{final}}}{p^{\text{final}}} \tag{5.8}$$

Results for such a variable are shown in Figure 5.12a, where it is possible to notice that all electromagnetic objects have a similar behavior while hadrons tend to cluster for low values of $\Delta p/p$ (which correspond to no energy loss). The plots in Figure 5.12b and 5.12c show that $\Delta p/p$ does not change when looking in different n_{vtx} or E_T bins. The last plot, Figure 5.12d, shows that the region of the detector has an impact on the distribution and must be taken into account.

5.3 *MultiLepton* menu

As already said in the introduction to this chapter, the $H \to ZZ^{(*)} \to 4\ell$ analysis has used the *loose*++ identification menu for data collected in 2011 at 7 TeV. There are some reasons which pushed us into developing, as part of the work for this thesis, a new menu for 2012 data, which could be explicitly dedicated to our analysis:

- The pile-up conditions of the data taking at 8 TeV in 2012 were expected (and proved to be) much harder than those of the previous year. A high inefficiency has been seen for the *loose*++ menu with an increasing number of vertices in the event in our simulation.

- The new reconstruction (with improved track-to-cluster matching and bremsstrahlung recovery, see Chapter 4), which was finally included in the official ATLAS software release in 2012, needed a new optimization of the cuts used by the menu. In particular, some of the new features of the GSF reconstruction were not exploited by the standard *loose*++ menu.

- The major background expected for the $H \to ZZ^{(*)} \to 4\ell$ analysis is given by hadrons faking electrons and we wanted to design a menu in the attempt of reducing as much as possible this component.

- The standard *loose*++ menu follows the same strategy applied at the trigger level, but in our case, having at least two to a maximum of four electrons, we had the chance to develop the *MultiLepton* menu without be-

ing forced to follow the trigger prescriptions. In this way we can use more variables than the standard *loose*++ menu.

The strategy followed in developing the *MultiLepton* menu was the following:

- Guarantee robustness against pile-up. The performance of the menu must not be spoiled by an increase in the calorimeter noise induced by pile-up, especially because the 2012 data taking conditions where not completely known at the moment the menu was developed. On top of this we must note that the pile-up simulation in our generators has proven to be quite trustworthy but not as much as to explicitly derive cuts dependent on n_{vtx} or $< \mu >$. For this reason we preferred to have a cut-based menu where the effect of pile-up has been mitigated by loosening the cuts on the variables which showed a particular dependence on n_{vtx}, for example R_{had} and R_{η}. Neural network or in general multivariate techniques have not been taken into account because we needed to be able to identify problematic cuts or variables not well represented in Monte Carlo as we were collecting data: only a cut-based menu can grant direct control over each variable used.

- Achieve the best possible efficiency and be sure that the menu will guarantee this efficiency for all 2012. The primary goal for a Higgs discovery is, in fact, a very high identification efficiency, and the background contributions are expected to be very small anyway. We must also note that our simulation of the background processes is not as reliable as the one we have for isolated electrons: for these cases we have had, from 2010 on, the chance to observe the behavior of data itself using *Tag & Probe* techniques (for a complete explanation, see Appendix A) and thus refine our simulation. For these reasons we preferred to use only the Monte Carlo for isolated electrons in the derivation of the cuts.

- Make use of all the features provided by the new GSF reconstruction algorithm. This includes bremsstrahlung depending and track-cluster matching variables.

The choice of the variables to be used in the *MultiLepton* menu has been made trying to keep the most discriminating variables and at the same time

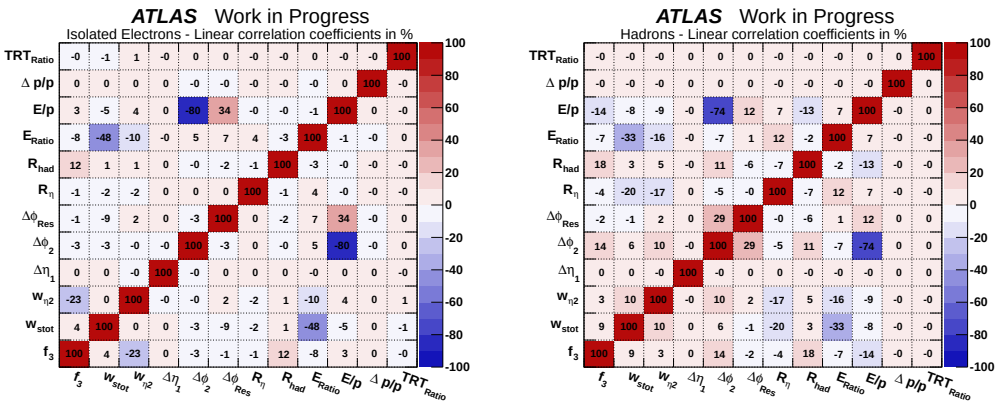

(a) **(b)**

Figure 5.13 Linear correlations for all the variables detailed in Section 5.2, in (a) for isolated electrons and in (b) for hadrons.

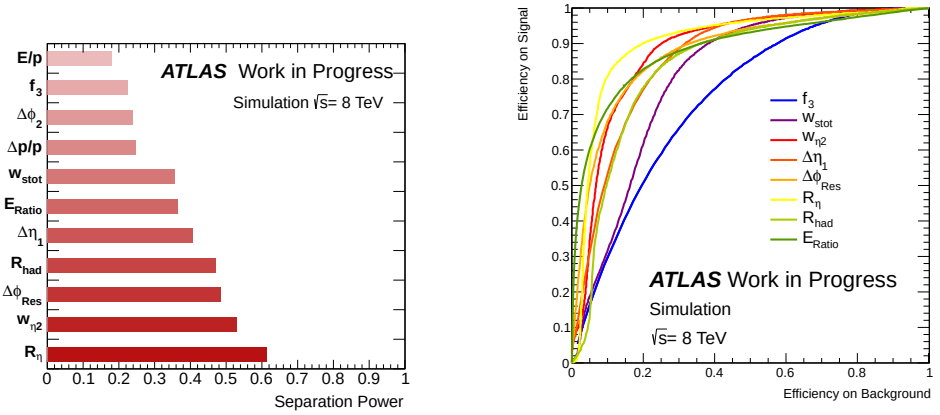

(a) **(b)**

Figure 5.14 Separation power and receiver operator characteristics curves for the variables used in the *MultiLepton* menu. The separation power is defined as one minus the overlap integral between the hadron and electron shapes. The ROC curves show the dependence of efficiency on signal as a function of the efficiency on the background.

those better represented in Monte Carlo. Among those who have been presented in the previous Section, the $\Delta\phi_2$ variable has not been kept since it does not provide more information and has a smaller rejection power than

$\Delta\phi_{Res}$. Another variable that has been discarded is E/p, since it does not provide a very good discrimination between hadrons and electrons and it also depends considerably on the material of the Inner Detector, which has to be properly simulated. For all the variables taken into account, we show in Figure 5.14 two interesting quantities: in Figure 5.14a we show the separation power of each variable between hadrons and isolated electrons, while in Figure 5.14b we show the efficiency on signal as a function of the efficiency on hadrons. The separation power is calculated evaluating the overlap integral of the shapes of isolated electrons and hadrons. It is clear that E/p and $\Delta\phi_2$ do not provide great performance and have been dropped, while f_3, which also provides a small contribution to rejecting hadrons, has been kept for analogy with the trigger menu.

5.3.1 Derivation of the *MultiLepton* menu

All the motivations given in the previous Section have brought us to define the following procedure for deriving the cuts of the identification menu:

$E_T \times \eta$ binning

As shown in the plots of Section 5.2, all quantities show different shapes in different bins in E_T or η. The simplest way to account for this is to define a 2D grid of $E_T \times \eta$ bins and derive different cuts for each bin.

$$\begin{aligned} E_T \text{ bins} &= \{5, 10, 15, 20, 30, 40, 50, 60, 70, 80\} \text{ (GeV)} \\ \eta \text{ bins} &= \{0, 0.1, 0.6, 0.8, 1.15, 1.37, 1.52, 1.81, 2.01, 2.37, 2.47\} \end{aligned}$$

Small correlations

Given the small correlations between the chosen input variables, visible in Figure 5.13 for both isolated electrons (a) and hadrons (b), we derived the cuts independently for each of them, thus exploiting all the available statistics.

Predefined efficiencies

Each single cut has been derived by imposing a specific efficiency on isolated electrons for each particular variable in each particular $E_T \times \eta$

bin. These values can range from 96% to 99%, depending on the stability against pile-up or the discrimination power of the variable.

***hard-brem* and *low-brem* categories**

Among all the variables shown (summarized in Table 5.1), the $\Delta p/p$ variable has not been used to derive cuts, but to categorize electrons into two different sets: those who lost a considerable amount of energy due to bremsstrahlung (*hard-brem*) and those who suffered from minor losses (*low-brem*). In order to decide the boundary that separates *hard-brem* from *low-brem* electrons we used a sample with hadrons and identified the value of $\Delta p/p$ which could contain 95% of them. In this way we will have one category (*low-brem*) which is basically composed by electrons with minor energy losses together with hadrons, and another category (*hard-brem*) which will have a very small contamination of hadrons and will allow us to tune our cuts in a different way. For this reason the only difference between these two categories will be represented by the cut on $\Delta\phi_{Res}$, split in *low-brem* and *hard-brem*.

Table 5.1 Summary of the variables used in the *MultiLepton* menu.

Name	Type	Region	Use
E_{Ratio}	Calorimetric	$\|\eta\| < 1.37$ and $1.52 < \|\eta\| < 2.37$	cut
w_{stot}	Calorimetric	$\|\eta\| < 1.37$ and $1.52 < \|\eta\| < 2.37$	cut
R_η	Calorimetric	all detector	cut
$w_{\eta 2}$	Calorimetric	all detector	cut
f_3	Calorimetric	$\|\eta\| < 2.37$	cut
R_{had}	Calorimetric	all detector	cut
$\Delta\eta_1$	Track-cluster matching	all detector	cut
$\Delta\phi_{Res}$	Track-cluster matching	all detector	cut
TRT_{Ratio}	Tracking	$1.37 < \|\eta\| < 1.52$	cut
$\Delta p/p$	Tracking	all detector	category
n_{hits}^{Pixel}	Tracking	all detector	cut
$n_{hits}^{Silicon}$	Tracking	all detector	cut

Finally in Table 5.1 we summarized the variables contained in the *MultiLepton* menu, their type, region of validity and the type of operation performed with

their information. We can notice that there are two variables explicitly related to the tracking reconstruction of electrons, n_{hits}^{Pixel} and $n_{hits}^{Silicon}$, which represent respectively the number of hits in the Pixel detector and the number of hits in the Pixel and SCT detectors together. A cut on these two variables makes sure that the identified electron has been built using a good track.

5.3.2 Expected performance of the *MultiLepton* menu and comparison with the standard *loose*++ menu

In view of the 2012 data taking also the standard working points of electron identification, *loose*++/*medium*++/*tight*++, have been re-optimized. The working point which we can use for comparison, as already explained in the introduction to this Chapter, is the *loose*++ menu. This menu has been improved with respect to 2011 in order to reduce the efficiency loss at high pile-up and makes use of these variables: R_{had}, R_η, $w_{\eta 2}$, w_{stot}, E_{Ratio}, $\Delta\eta_1$, n_{hits}^{Pixel} and $n_{hits}^{Silicon}$. In such a menu, no variable that can differentiate between *hard-brem* and *low-brem* electrons has been used and the $\Delta\eta_1$ cut is flat (not optimized for each $E_T \times \eta$ bin) at $\Delta\eta_1 = 0.015$.

The *MultiLepton* menu has been explicitly designed to obtain the very high efficiency typical of the *loose*++ menu, reducing as much as possible the effect of pile-up and obtaining more rejection on hadrons by using more variables without significant correlations between them.

In Figure 5.15, 5.16 and 5.17 are shown the efficiencies and rejections on conversions and hadrons for the *MultiLepton* menu and the *loose*++ menu in its 2011 and 2012 implementations. As we designed, the *MultiLepton* menu has the same efficiency overall of the *loose*++ menu (2012 version), but the dependence on n_{vtx} has been reduced to minimum, by loosening the cuts on R_{had} and R_η which are the most sensitive variables to pile-up. Also the behavior as a function of p_T is more reasonable than both implementations of the *loose*++ menu. The shape in η is very similar between the *MultiLepton* menu and the *loose*++ menu for 2012 and reflects the different regions of the detector. The great improvement of the *MultiLepton* menu is the almost doubled rejection on hadrons which is the direct result of the choices made in terms of variables to be used. Even if R_{had} and R_η, which are the most powerful vari-

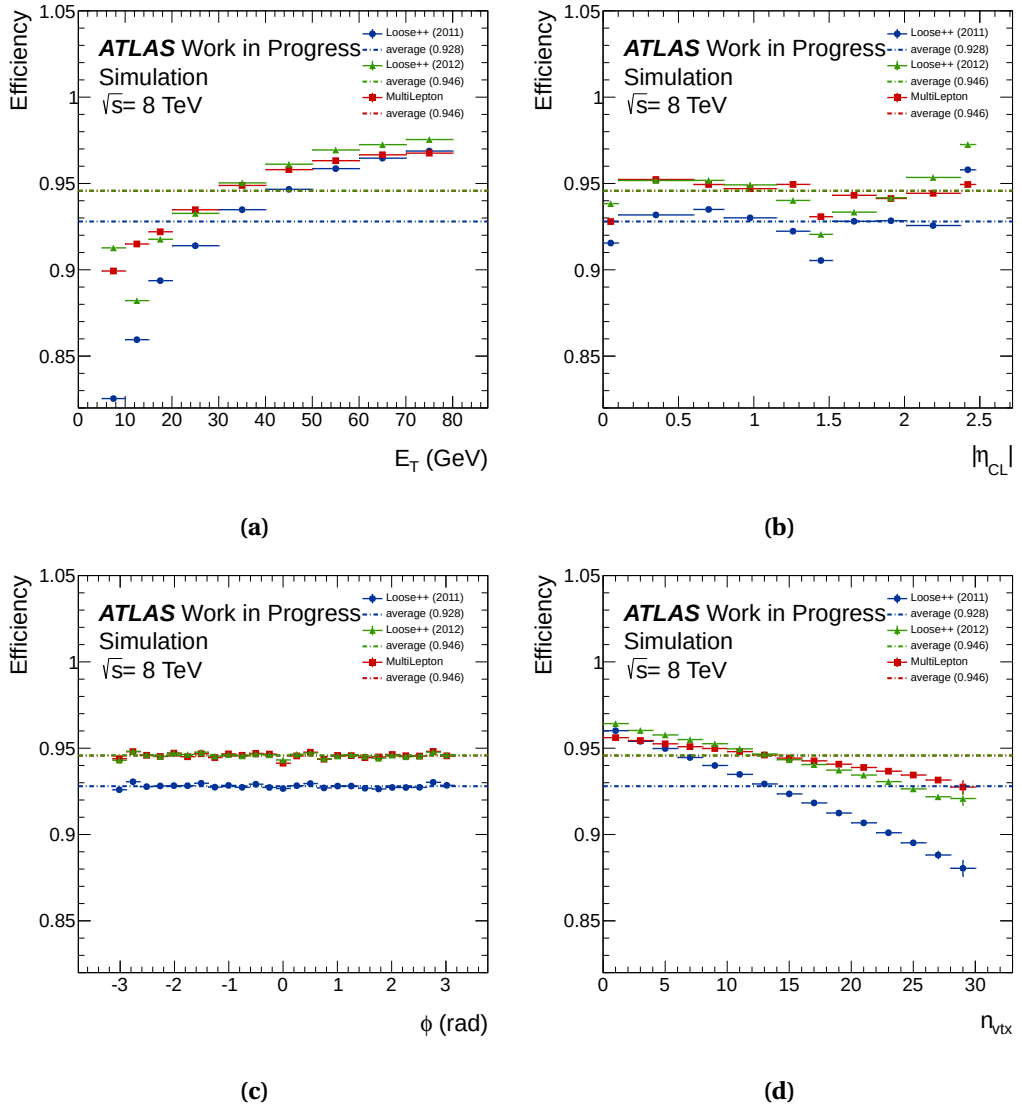

Figure 5.15 Expected efficiency of the *MultiLepton* (red), the 2011 *loose*++ (azure) and the 2012 *loose*++ menu (green), as a function of p_T (a), η (b), ϕ (c) and n_{vtx} (d).

ables in rejecting hadrons, have been set up with very loose cuts, a certain number of other factors allowed the *MultiLepton* menu to achieve a very high rejection, which we summarize here:

- Introduction of *hard-brem* and *low-brem* categories and subsequent cut on $\Delta\phi_{Res}$.

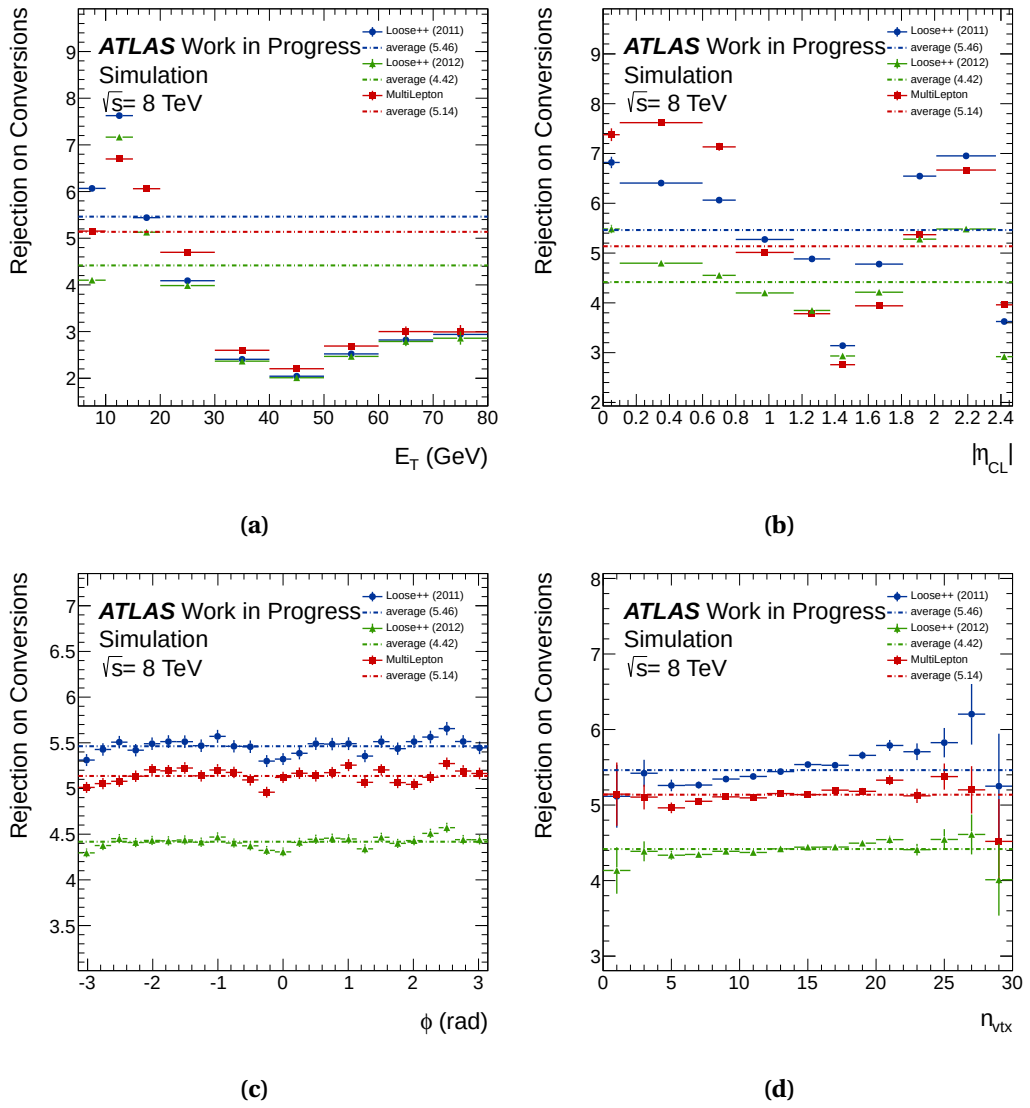

Figure 5.16 Expected rejection on conversions of the *MultiLepton* (red), the 2011 *loose*++ (azure) and the 2012 *loose*++ menu (green), as a function of p_T (a), η (b), ϕ (c) and n_{vtx} (d).

- Addition of f_3 to complement the information provided by R_{had}.
- Use of an $E_T \times \eta$ binned cut on $\Delta\eta_1$.

We also show the results for the measurement of the *MultiLepton* menu (as well as for the other three working points) identification efficiency done with J/ψ, $Z \rightarrow ee$ and $W \rightarrow e\nu$ *Tag & Probe* on the first data collected in the year

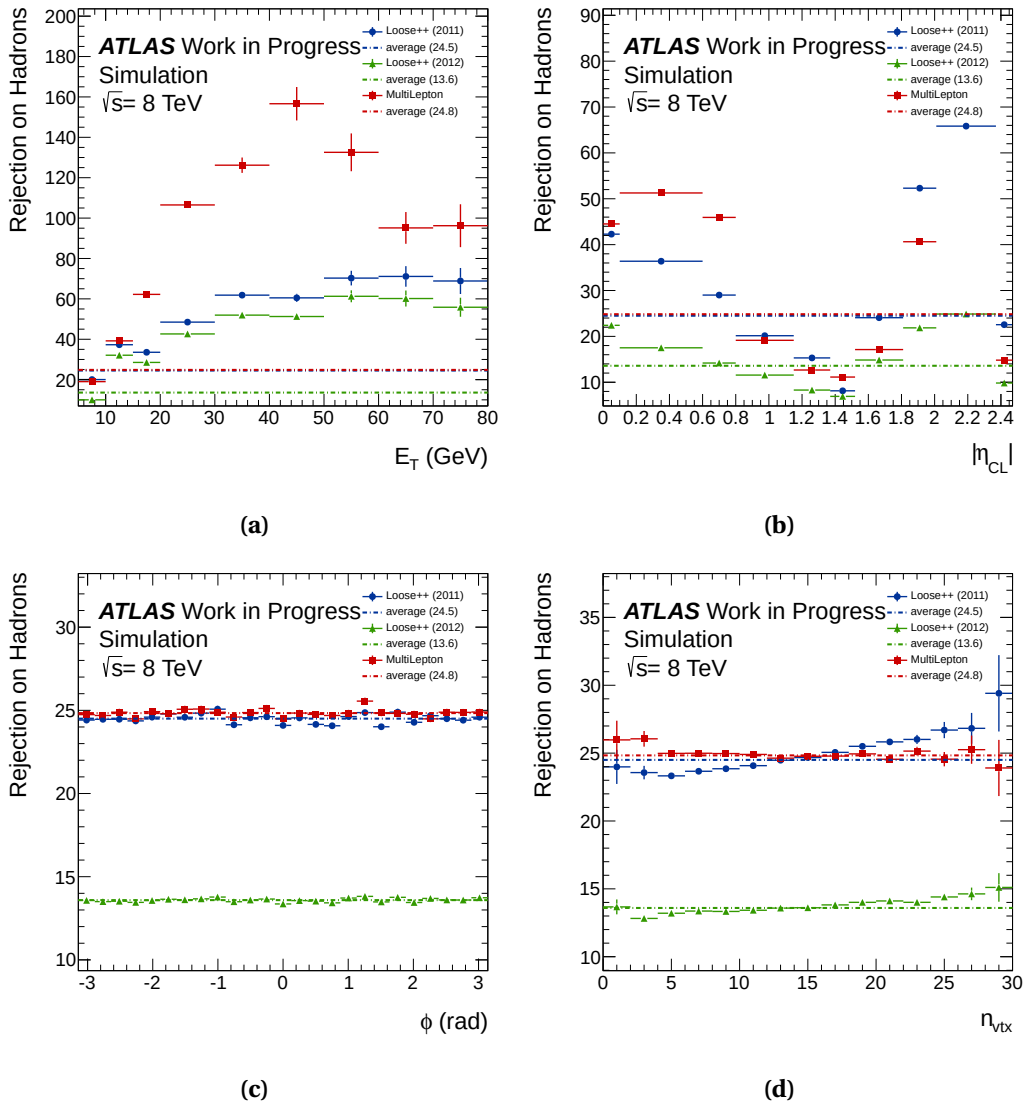

Figure 5.17 Expected rejection on hadrons of the *MultiLepton* (red), the 2011 *loose*++ (azure) and the 2012 *loose*++ menu (green), as a function of p_T (a), η (b), ϕ (c) and n_{vtx} (d).

2012 and on Monte Carlo, in Figure 5.18. The efficiencies provided by the *loose*++ menu and the *MultiLepton* are very similar and, as we expected, it seems that the latter is less pile-up dependent.

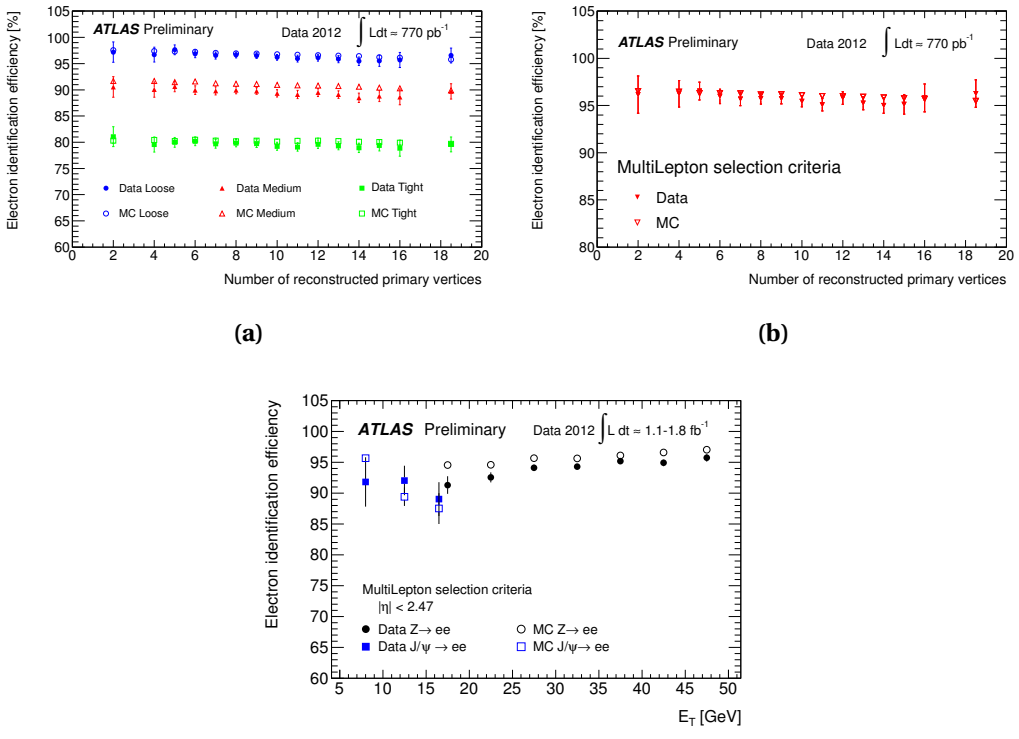

Figure 5.18 Efficiency of the electron identification working points, in (a) for the *loose++*/*medium++*/*tight++* menus, while in (b) for the *MultiLepton* menu as a function of n_{vtx}. In (c) it is shown the efficiency of the *MultiLepton* menu as a function of p_T instead. These efficiencies have been estimated on both data and simulation using the *Tag & Probe* technique withn J/ψ, $Z \rightarrow ee$ and $W \rightarrow e\nu$.

Chapter 6

$H \to ZZ^{(*)} \to 4\ell$ analysis: event selection

In this chapter we will describe the requirements for the $H \to ZZ^{(*)} \to 4\ell$ analysis on 2011 data at $\sqrt{s}$ = 7 TeV and on 2012 data at $\sqrt{s}$ = 8 TeV. The integrated luminosities for 2011 are 4.8 fb^{-1} for final states with muons and 4.9 fb^{-1} for final states with only electrons, while the integrated luminosity for 2012 is 5.8 fb^{-1}. In the last part of this chapter we will investigate in more detail the work done, within the development of this PhD thesis, for the determination of the Data/Monte Carlo scale factors for the selections of the $H \to ZZ^{(*)} \to 4\ell$ analysis.

6.1 Monte Carlo samples used for signal and background

As a simulation of our signal process, $H \to ZZ^{(*)} \to 4\ell$, we used the POWHEG Monte Carlo event generator [66, 67]. In POWHEG, gluon fusion and vector-boson fusion production mechanisms are provided separately with matrix elements up to next-to-leading order. POWHEG is interfaced to PYTHIA [68, 69] for showering and hadronization, while PYTHIA itself is interfaced to PHOTOS [70, 71] for quantum electrodynamics radiative corrections in the final state. For what regards the production of a Higgs boson in association with a vector-boson, $pp \to WH$ and $pp \to ZH$, it has been simulated using PYTHIA.

6.1.1 Cross sections

The Higgs boson production cross sections and decay branching ratios, as well as their uncertainties, are taken from Refs. [19, 20]. The cross sections for the gluon-fusion process have been calculated to next-to-leading order [72, 73, 74], and next-to-next-to-leading order [75, 76, 77] in QCD and they include also soft-gluon re-summations calculated in the next-to-next-to-leading log approximation [78]. Next-to-leading order electroweak radiative corrections have also been taken into account [79, 80].

6.1.2 Branching ratios

We used PROPHECY4F to obtain the Higgs boson decay branching ratios [81] to the different four-lepton final states. PROPHECY4F includes the complete next-to-leading order QCD and electroweak corrections, as well as interference effects between identical fermions. In Table 6.2 we summarized the production cross sections and branching ratios for $H \to ZZ^{(*)} \to 4\ell$ for several Higgs boson masses. These cross sections ad branching ratios are those used in the analysis to normalize the signal Monte Carlo.

6.1.3 Uncertainties

The QCD scale uncertainties for m_H = 125 GeV [19] is $^{+7}_{-8}$% for the gluon-fusion process and ±1% for the vector-boson fusion and associated production, $pp \to WH$ and $pp \to ZH$, processes. The uncertainty of the production cross section due to the parton distribution functions and α_s is ±8% for $gg \to H$ processes and ±4% for $q\bar{q} \to H$ processes.

6.1.4 Background samples

The irreducible $ZZ^{(*)}$ background has been taken from POWHEG [82] for $q\bar{q} \to ZZ$ and gg2ZZ [83] for $gg \to ZZ$ and then normalized to the MCFM prediction [84]. The $ZZ^{(*)}$ background is affected by a ±5% due to the QCD scale uncertainty, while the PDF and α_s uncertainties are ±4% for $q\bar{q} \to ZZ$ and ±8% for $gg \to ZZ$. For what regards the reducible backgrounds, we have:

Table 6.1 Higgs boson production cross sections for gluon fusion, vector-boson fusion and associated production with a W or Z boson in pp collisions at $\sqrt{s}$ = 7 TeV. The quoted uncertainties correspond to the total theoretical systematic uncertainties. We did not quote any production cross section for associated production with a W or Z boson for Higgs masses above 200 GeV since it is negligible. In the last column are shown the decay branching ratios for $H \to 4\ell$, with $\ell = e$ or μ.

m_H [Gev]	$\sigma(gg \to H)$ [pb]	$\sigma(qq' \to Hqq')$ [pb]	$\sigma(q\bar{q} \to WH)$ [pb]	$\sigma(q\bar{q} \to ZH)$ [pb]	$\mathrm{BR}(H \to ZZ^{(*)} \to 4\ell)$ $[10^{-3}]$
125	$15.3^{+3.0}_{-2.3}$	1.21 ± 0.03	$0.57^{+0.02}_{-0.03}$	$0.32 \pm .02$	0.13
130	$14.1^{+2.7}_{-2.1}$	1.15 ± 0.03	0.50 ± 0.02	0.28 ± 0.01	0.19
190	$5.9^{+1.0}_{-0.9}$	0.69 ± 0.02	0.125 ± 0.005	$0.074 \pm .004$	0.94
400	$2.03^{+0.32}_{-0.33}$	$0.162^{+0.009}_{-0.005}$	–	–	0.21
600	0.37 ± 0.06	$0.058^{+0.005}_{-0.002}$	–	–	0.23

Table 6.2 Higgs boson production cross sections for gluon fusion, vector-boson fusion and associated production with a W or Z boson in pp collisions at $\sqrt{s}$ = 8 TeV. The quoted uncertainties correspond to the total theoretical systematic uncertainties. We did not quote any production cross section for associated production with a W or Z boson for Higgs masses above 200 GeV since it is negligible. In the last column are shown the decay branching ratios for $H \to 4\ell$, with $\ell = e$ or μ.

m_H [GeV]	$\sigma(gg \to H)$ [pb]	$\sigma(qq' \to Hqq')$ [pb]	$\sigma(q\bar{q} \to WH)$ [pb]	$\sigma(q\bar{q} \to ZH)$ [pb]	$\mathrm{BR}(H \to ZZ^{(*)} \to 4\ell)$ $[10^{-3}]$
125	19.5 ± 2.9	$1.56^{+0.04}_{-0.05}$	0.70 ± 0.03	0.39 ± 0.02	0.13
130	18.1 ± 2.6	1.49 ± 0.04	0.61 ± 0.03	0.35 ± 0.02	0.19
190	7.9 ± 1.1	$0.91^{+0.03}_{-0.02}$	0.156 ± 0.007	0.094 ± 0.006	0.94
400	2.9 ± 0.4	0.25 ± 0.01	–	–	1.21
600	0.5 ± 0.1	0.097 ± 0.004	–	–	1.23

Z + jets

The production of a Z boson associated with jets is simulated using ALPGEN and it accounts for two different sources: Z + light jets and $Z + b\bar{b}$. The first one includes $Zc\bar{c}$ in the massless c-quark approximation and $Zb\bar{b}$ from parton showers, while the second one uses matrix element calculations to take into account the b-quark mass. In all these

cases also the Drell-Yan contribution is included in these samples.

$t\bar{t}$

The production of $t\bar{t}$ pairs is modeled using MC@NLO [85] and is normalized to the approximate next-to-next-to-leading cross section calculated using HATHOR [86]. The effect of the QCD scale uncertainty on the cross section account for a $^{+4}_{-9}$%, while the effect of PDF and α_s uncertainties is ±7%.

ALPGEN and MC@NLO are interfaced to HERWIG [87] for parton shower hadronization and to JIMMY [88] for the underlying event simulation.

Generated events are fully simulated using the ATLAS detector simulation which is based on the GEANT4 framework [61]. Additional pp interactions in the same and nearby bunch crossings (pile-up) are included in the simulation. The Monte Carlo samples are re-weighted to reproduce the observed distribution of the mean number of interactions per bunch crossing in the data.

6.2 Lepton reconstruction and identification

6.2.1 Trigger requirements

In this analysis single-lepton and di-lepton triggers have been used to collect data. The different p_T (in the case of muons) or E_T (in the case of electrons) thresholds for these triggers are summarized in Table 6.3:

Table 6.3 Summary of the single-lepton and di-lepton triggers used in the analysis.

	$\sqrt{s}$ = 7 TeV	$\sqrt{s}$ = 8 TeV
Trigger Type	Threshold(s) (GeV)	
single-muon	18	24
di-muon (symmetric)	10/10	13/13
di-muon (asymmetric)	-	18/8
single-electron	20 to 22[1]	24
di-electron	12/12	12/12

6.2.2 Electrons

The reconstruction of electrons has been described in Chapter 4 and their identification in Chapter 5. The identification menu used in the 2011 data analysis is *loose*++, while for 2012 we used the dedicated *MultiLepton* menu. Electrons are required in general to have at least 7 GeV of E_T and to be contained in the acceptance of the Inner Detector, $|\eta| < 2.47$.

6.2.3 Muons

In ATLAS there are four types of muons, which differ from each other in the way they are reconstructed:

Combined muons

Combined muons are the basic type of muon for any analysis in ATLAS. They are reconstructed matching a track in the Muon Spectrometer with a track in the Inner Detector. The final parameters of the muon track are obtained from the combination of these two tracks and the information regarding impact parameter are directly taken from the Inner Detector track.

Segment tagged muons

We identify an Inner Detector track as a muon if its trajectory, extrapolated to the Muon Spectrometer, can be matched with straight track segments in the precision chambers. As a result, the final muon track parameters will be those of the original Inner Detector track.

Calorimeter tagged muons

We also identify a track in the Inner Detector as a muon if its energy deposit in the calorimeter are compatible with the minimum ionizing particle hypothesis (as the muon would be). Also in this case the final muon track parameters are those of the Inner Detector track. They are used in our analysis to cover the region $0 < |\eta| < 0.1$ which has a hole in the Muon Spectrometer.

[1]The single-electron threshold in the 2011 data taking period has been changed to meet the trigger requirements in terms of processing time.

Stand-alone muons

The stand-alone muon are reconstructed using information from the Muon Spectrometer only and the final track parameters are taken from the Muon Spectrometer track extrapolated to the primary vertex, by taking into account multiple scattering effects and energy loss in the traversed material. These muons are used to extend the standard coverage provided by the tracker ($|\eta| < 2.47$) exploiting the fact that the muon spectrometer extends to $|\eta| = 2.7$.

The minimal energy that a muon must have to meet the analysis requirements is 6 GeV.

6.3 Event Selection

The event selection of the analysis proceeds as follows:

- Lepton quadruplets are built requiring two same-flavor, opposite-sign lepton pairs in one event.
- We require all the four leptons to originate from the primary vertex[2] in the event, by demanding the impact parameter of their track along the z axis (already defined in Section 4.2) to be within 10 mm from the primary vertex.
- In order to reject cosmic muons, we require that all muons in the analysis should have a d_0 (see Section 4.2 for the definition) within 1 mm from the primary vertex.
- Within one quadruplet, we require the most energetic lepton to have p_T >20 GeV, the second most energetic to have p_T >15 GeV and the third most energetic to have p_T >10 GeV.
- An overlap removal is applied on the leptons, requiring that same-flavor leptons have $\Delta R > 0.1$ and $\Delta R > 0.2$ if the overlap is between an electron and a muon. In case of overlap, only the highest-E_T lepton is kept.

[2]The primary vertex in the event is the one with the highest squared sum of p_T of associated tracks, provided that it has at least three tracks.

- The di-lepton which has a combined mass closest to the Z boson mass (m_Z =91.1876 GeV) is denoted as the leading pair in the quadruplet. The invariant mass of this pair is always regarded to as m_{12} and we require it to be close to m_Z: 50 < m_{12} <106 GeV. The wider window for m_{12} below m_Z has been introduced to extend the analysis at low mass, where we can have the Higgs boson decaying into two virtual Z.

- The other di-lepton that forms the quadruplet, usually referred to as the sub-leading one, is required to have a mass, m_{34}, which satisfies m_{min}< m_{34} <115 GeV, where the value of m_{min} depends on the reconstructed invariant mass of the lepton quadruplet (always denoted as $m_{4\ell}$), as a linear interpolation of the numbers shown in Table 6.4.

- Within a quadruplet, we build all possible opposite-sign, same-flavor pairs and each of them must satisfy $m_{\ell\ell}$ >5 GeV (to avoid considering leptons from the decay of a J/ψ).

- We require that each lepton passes a cut on the normalized track isolation, defined as the sum of the transverse momenta of all tracks within $\Delta R < 0.2$ around the lepton, divided by the lepton p_T[3]. This quantity, $\sum p_T/p_T$, must be smaller than 0.15 for all leptons in the quadruplet.

- A cut on the normalized calorimetric isolation is also applied. For electrons in 2012, this quantity is calculated by summing the positive-energy topological clusters with a barycenter in a cone of $\Delta R < 0.2$ around the electron and then dividing by the electron p_T. For muons and for electrons in 2011, the calorimetric isolation is calculated by summing the energies of all the calorimeter cells lying in a cone of $\Delta R < 0.2$ from the lepton. We require electrons in 2011 to have $\sum E_T/p_T < 0.3$ and in 2012 to have $\sum E_T/p_T < 0.2$. For muons the cut is $\sum E_T/p_T < 0.3$ for

[3]In the calculation of the sum of the momenta of the tracks in the $\Delta R = 0.2$ cone, the track of the lepton itself is of course discarded. Only tracks with minimal requirements are used in the computation of $\sum p_T$: for muons, they must have at least four hits in the Pixel and SCT detectors as well as p_T >1 GeV. For what regards electrons, they should have at least nine hits in the Pixel and SCT detectors, at least one hit in the b-layer and a p_T greater than 0.4 GeV for the 2012 analysis, while in 2011 they should have 7 hits in the Pixel and SCT detectors and a minimal p_T of 1 GeV.

combined, segment tagged and calorimeter tagged muons, while it is $\sum E_T/p_T < 0.15$ for stand-alone muons.

- A final cut is applied on the impact parameter significance of all the leptons, by requiring $d_0/\sigma_{d_0} < 3.5$ for muons and $d_0/\sigma_{d_0} < 6.5$ for electrons.

Table 6.4 Lower thresholds for the cut on m_{34}, for specific values of $m_{4\ell}$. For $m_{4\ell}$ values which fall between those given in this table, a linear interpolation is made to obtain the cut to be applied.

$m_{4\ell}$ [GeV]	≤120	130	150	160	165	180	≥190
m_{min} threshold [GeV]	17.5	22.5	30	30	35	40	50

6.4 Invariant mass resolution

As already stated in Chapter 1, the $H \to ZZ^{(*)} \to 4\ell$ channels is very pure and it also provides a very good resolution on the invariant mass.

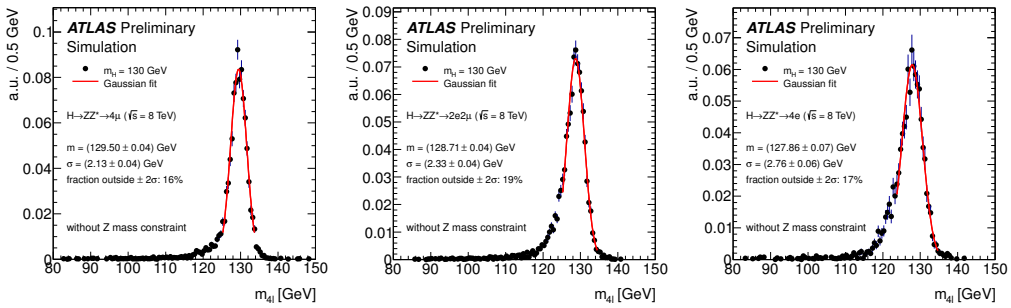

Figure 6.1 Invariant mass distributions (without any Z mass constraint) for simulated $H \to ZZ^{(*)} \to 4\mu$ (a), $H \to ZZ^{(*)} \to 2\mu 2e$ (b) and $H \to ZZ^{(*)} \to 4e$ (c) events for m_H=130 GeV, at $\sqrt{s}$ = 8 TeV. The slightly reduced mean values arise from radiative losses which are more explicit in channels involving electrons.

In Figure 6.1 are shown the invariant mass distribution for simulated Higgs of m_H = 130 GeV: the mean values are slightly lower than the expected Higgs

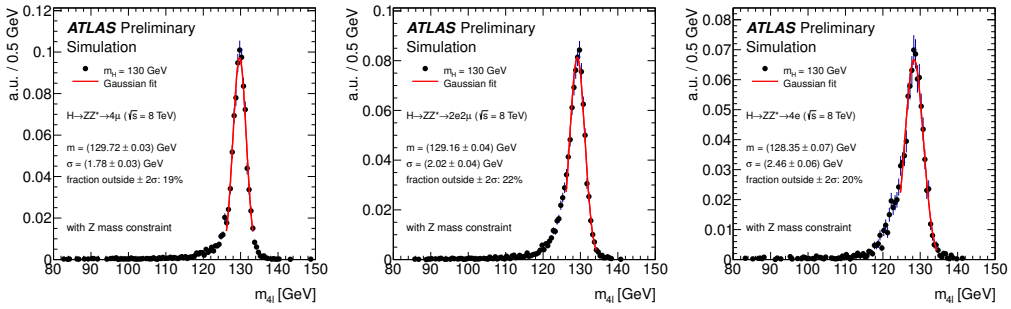

(a) **(b)** **(c)**

Figure 6.2 Invariant mass distributions (with Z mass constraint this time) for simulated $H \to ZZ^{(*)} \to 4\mu$ (a), $H \to ZZ^{(*)} \to 2\mu 2e$ (b) and $H \to ZZ^{(*)} \to 4e$ (c) events for m_H =130 GeV, at $\sqrt{s}$ = 8 TeV. The slightly reduced mean values arise from radiative losses which are more explicit in channels involving electrons.

boson mass (130 GeV) because of radiative losses. This effect is larger in channels involving electrons in the final state, where also the mass resolution is poorer. On the other hand, in Figure 6.2, we show the same exact distributions but applying a Z mass constraint on the leading di-lepton mass and also on the sub-leading di-lepton (if $m_{4\ell} > 190$ GeV). The improvements in the mass resolution are clearly visible in the plots and are also summarized in Table 6.5: for this reason the Z mass constraint has been introduced in the final analysis of our data.

Table 6.5 Summary of the invariant mass resolutions of the different sub-channels of the $H \to ZZ^{(*)} \to 4\ell$ analysis, with and without the Z mass constraint.

	Invariant mass resolution (GeV)		
	$H \to ZZ^{(*)} \to 4\mu$	$H \to ZZ^{(*)} \to 2\mu 2e$	$H \to ZZ^{(*)} \to 4e$
Without Z mass constraint	2.13 ± 0.04	2.33 ± 0.04	2.76 ± 0.06
With Z mass constraint	1.78 ± 0.03	2.02 ± 0.04	2.46 ± 0.06

6.5 Data/Monte Carlo scale factors for additional selection

The determination of efficiency scale factors, i.e. the efficiency of data relative to Monte Carlo, is fundamental for any study that involves a cross section measurement or the estimation of a limit, such as $H \to ZZ^{(*)} \to 4\ell$. The $H \to ZZ^{(*)} \to 4\ell$ search uses two different sets of cuts on the leptons:

Pre-selection cuts

These cuts have been already summarized in Section 6.2 and consist of the basic requirements established by the Combined Performance groups. The scale factors for these pre-selection cuts are provided by the Combined Performance groups themselves.

$H \to ZZ^{(*)} \to 4\ell$ specific cuts

As described in Section 6.3, the $H \to ZZ^{(*)} \to 4\ell$ analysis uses three additional cuts to further improve the signal/background ratio. These selections are:

Calorimetric isolation

We require $\sum \mathrm{E}_T{}^{\Delta R=0.2}/\mathrm{p}_T < 0.3$ for muons and $\sum \mathrm{E}_T{}^{\Delta R=0.2}/\mathrm{p}_T < 0.2$ for electrons, where the sum is made on all the calorimeter cells lying in a cone of $\Delta R = 0.2$ around the position of the lepton. We remove the contribution from overlapping leptons which fall within a cone of $\Delta R = 0.18$ from the original lepton.

Track isolation

We request $\sum \mathrm{p}_T{}^{\Delta R=0.2}/\mathrm{p}_T < 0.15$ for both muons and electrons, where the sum is made on all tracks contained in a cone of $\Delta R = 0.2$ around the position of the lepton. We remove the contribution from overlapping leptons which fall within a cone of $\Delta R = 0.2$ from the original lepton.

Impact parameter significance

We demand our muons to have $d_0/\sigma_{d_0} < 3.5$ and our electrons to have $d_0/\sigma_{d_0} < 6.5$.

For this thesis we took care of evaluating the scale factors relative to the additional cuts on electrons for the 2012 analysis. In the following Section we will describe how this estimation has been performed.

6.5.1 Scale factor determination technique

The efficiency, on data and Monte Carlo, of the isolation and impact parameter requirements has been measured (following the recommendations from the Egamma Combined Performance group) using a *Tag & Probe* technique (for a general explanation of the methodology applied, see Appendix A) over the full 5.8 fb^{-1} data sample collected in 2012 at 8 TeV. The tag electrons must pass the *tight++* requirement, have an E_T greater than 15 GeV and they must be matched with a trigger electron. Tags are also required to have $|\eta| < 1.37$, to improve the signal/background ratio below the Z peak, especially at low E_T. For what regards the probe, we require it to pass the basic requirements established by the Combined Performance group, shown in Section 6.2.2. Finally, *Tag & Probe* pairs are built only when tag and probe have opposite charges and when ${E_T}^{\text{Tag}} > {E_T}^{\text{Probe}}$. The efficiency for data and Monte Carlo is calculated as the ratio of the number of probes passing the three additional requirements to the total number of probes, estimated in the range $m_Z \pm 5$ GeV. To extract the efficiency, a fit to the data is performed using a template for the signal taken from ALPGEN. Templates for both $t\bar{t}$ and $Z \to \tau\tau$ backgrounds are taken from Monte Carlo and their normalization is fixed in the fit. Finally, an exponential function is used to describe the contribution from all other sources of background. Since these backgrounds are primarily relevant at low E_T, the exponential function is used in the fits only for those bins with $p_T < 28$ GeV. Fits have been performed in bins of p_T and n_{vtx} independently, in order to derive scale factors as a function of both the kinematics of the electron and the pile-up environment. As an example of the fitting results, we show the invariant mass plots made with the fitted components before (on the left) and after (on the right) applying the additional cuts of Section 6.3 for $12 < p_T < 17$ GeV in Figure 6.3, for $28 < p_T < 35$ GeV in Figure 6.4, for $10 < n_{vtx} < 12$ in Figure 6.5 and for $18 < n_{vtx} < 20$ in Figure 6.6.

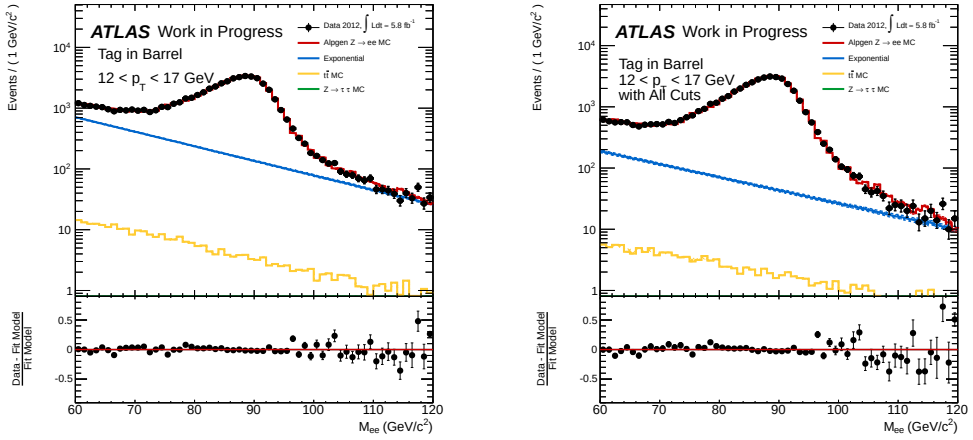

(a) **(b)**

Figure 6.3 Results for the fit of the $Z \to ee$ invariant mass fit for the $12 < p_T < 17$ GeV bin, in (a) before applying the additional cuts and in (b) after applying the isolation and impact parameter requirements. On the bottom part of the plot it is shown the ratio $\frac{\text{Data}-\text{Fit Model}}{\text{Fit Model}}$.

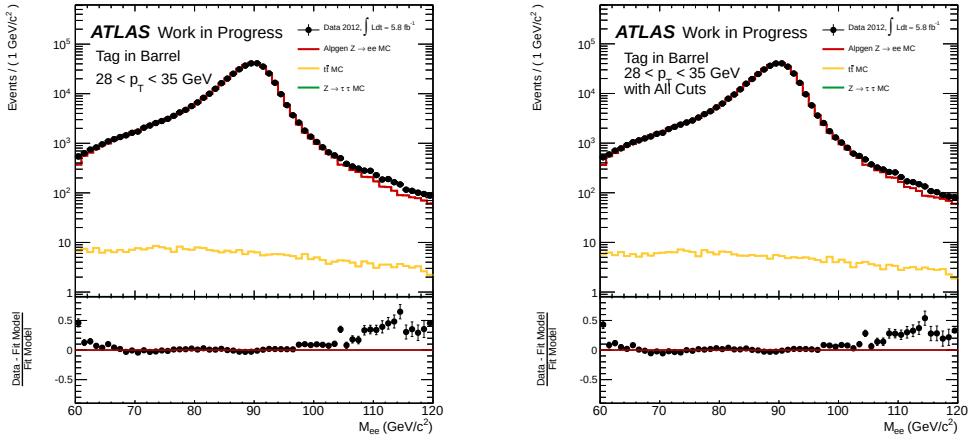

(a) **(b)**

Figure 6.4 Results for the fit of the $Z \to ee$ invariant mass fit for the $28 < p_T < 35$ GeV bin, in (a) before applying the additional cuts and in (b) after applying the isolation and impact parameter requirements. On the bottom part of the plot it is shown the ratio $\frac{\text{Data}-\text{Fit Model}}{\text{Fit Model}}$.

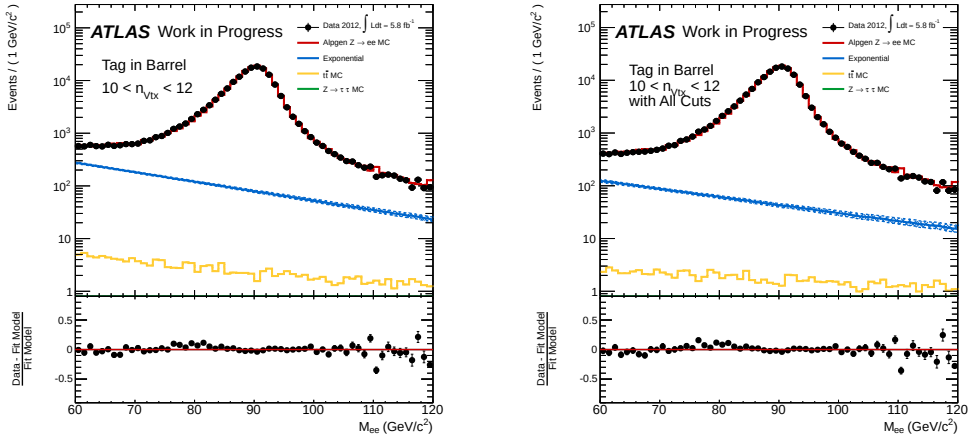

(a) **(b)**

Figure 6.5 Results for the fit of the $Z \to ee$ invariant mass fit for the $10 < n_{\text{vtx}} < 12$ bin, in (a) before applying the additional cuts and in (b) after applying the isolation and impact parameter requirements. On the bottom part of the plot it is shown the ratio $\frac{\text{Data}-\text{Fit Model}}{\text{Fit Model}}$.

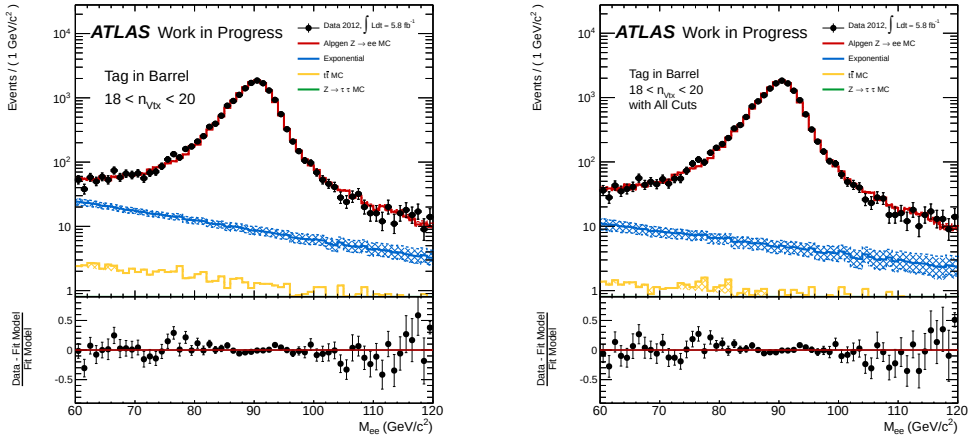

(a) **(b)**

Figure 6.6 Results for the fit of the $Z \to ee$ invariant mass fit for the $18 < n_{\text{vtx}} < 20$ bin, in (a) before applying the additional cuts and in (b) after applying the isolation and impact parameter requirements. On the bottom part of the plot it is shown the ratio $\frac{\text{Data}-\text{Fit Model}}{\text{Fit Model}}$.

The plots in Figure 6.3 show that in the low E_T bins the background contamination is quite high before the cuts and it is reduced approximately by a factor four when applying isolation and impact parameter significance requirements. Both plots, Figure 6.3a and Figure 6.3b, prove that the exponential function describes perfectly the background at low E_T.

The plots in Figure 6.4, on the other hand, show that for higher E_T (between 28 and 35 GeV, in this case) no function is needed for modelling the QCD background, since it is almost invisible.

Finally, the plots in Figure 6.5 and Figure 6.6 have been included to provide an example for the fitting results in bins of n_{vtx}: even with high pile-up our selection provides scale factors close to one and similar fits compared to the low pile-up regime.

Two different sources for systematic uncertainty are taken into account: the first one corresponds to the difference found when using PYTHIA or ALPGEN Monte Carlo as a template for signal events; the second one comes from varying the window from 3 GeV to 8 GeV around the Z peak used to count events.

6.5.2 Results

With the procedure explained in Section 6.5.1, we derived efficiencies for both data and Monte Carlo as a function of p_T (shown in Figure 6.7a) and as a function of n_{vtx} (shown in Figure 6.7b). The scale factors are then determined from the ratio between these two efficiencies, and are shown in Figure 6.8. It is clearly visible that the efficiencies tend to decrease slightly at high n_{vtx} values but the Monte Carlo clearly reproduces this inefficiency, since scale factors are all close to one (see Figure 6.8b). This small loss in efficiency is connected to the shifting of the isolation distributions given by a higher pile-up, and thus completely expected. For what regards the distribution as a function of p_T, we have to note that the *Tag & Probe* becomes more and more difficult at low E_T values since the background component increases substantially (which we can also observe from the difference between Figure 6.3 and Figure 6.4).

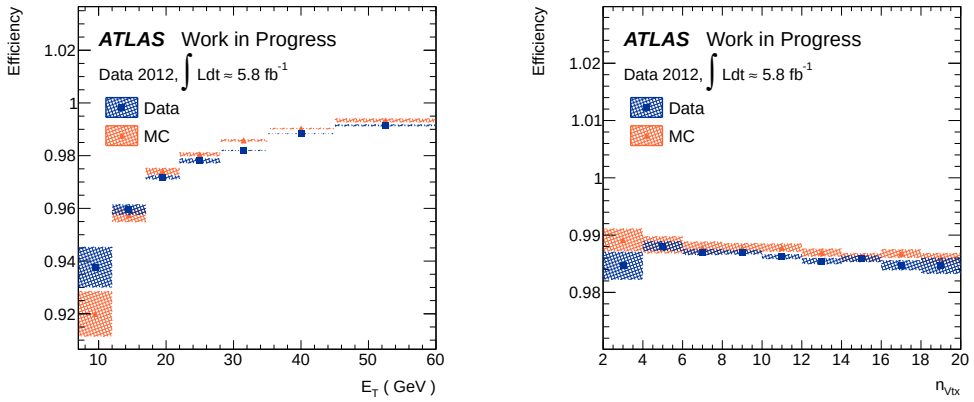

(a) **(b)**

Figure 6.7 Efficiency for data and Monte Carlo as a function of p_T (a) and as a function of n_{vtx} (b).

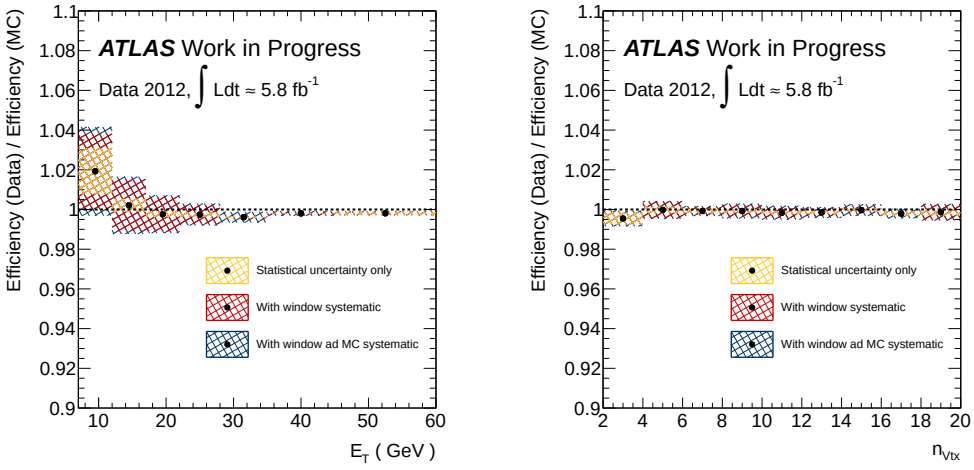

(a) **(b)**

Figure 6.8 Efficiency scale factors as a function of p_T (a) and as a function of n_{vtx} (b).

Chapter 7

$H \to ZZ^{(*)} \to 4\ell$ analysis: background estimation

sAfter explaining, in Chapter 6, the analysis requirements and samples used, in this Chapter we will describe the methods developed to estimate the background for the $H \to ZZ^{(*)} \to 4\ell$ analysis. As already shown in Section 6.3, the $H \to ZZ^{(*)} \to 4\ell$ channel gets split into three main sub-channels, 4μ, $4e$, and the mixed channel, containing a pair of muons and a pair of electrons. This mixed channel is subsequently split into two sub-channels, $2\mu 2e$ and $2e2\mu$. The first one accounts for those events where the leading di-lepton is a di-muon, while the second one for those events where the leading di-lepton is a di-electron. This splitting is needed because the backgrounds of this analysis will depend mostly on the flavor of the sub-leading di-lepton (which is usually regarded as Z_2) and this means that we will have methods for the estimation of the 4μ and $2e2\mu$ (which we in general denote as $\ell\ell + \mu\mu$ channels) and $4e$ and $2\mu 2e$ (denoted as $\ell\ell + ee$ channels) separately. In the following we will cover the estimations made in both of these two cases, giving particular attention to the part regarding the methods used in the $\ell\ell + ee$ case, which have been developed as part of the work for this PhD thesis.

In general, we can summarize the backgrounds of the $H \to ZZ^{(*)} \to 4\ell$ as follows:

Irreducible background

The irreducible background, given by the $pp \to ZZ^{(*)}$ production, has

been estimated using Monte Carlo simulated events normalized to the theoretical cross sections which have been shown in Section 6.1.

Reducible backgrounds

Under the "reducible backgrounds" label we group the $t\bar{t}$ and the Z + jets backgrounds. These are the contribution that depend on the sub-leading di-lepton flavor and these are all estimated using a mixture of Monte Carlo and data-driven techniques.

7.1 Estimation of the $\ell\ell + \mu\mu$ background

7.1.1 Fit to the m_{12} distribution

The biggest contribution we have in the $\ell\ell + \mu\mu$ case comes from $t\bar{t}$ and $Z + b\bar{b}$ background events. The best way to estimate this component is to build a control region where the $b\bar{b}$ component is dominant and this can be obtained by requiring the standard analysis cuts, with two exceptions:

- The sub-leading pair is not required to pass the calorimetric and track isolation cuts.
- The sub-leading di-muon has to fail the cut on the impact parameter significance. This allows us to remove almost completely the contribution to this control region given by the irreducible $ZZ^{(*)}$ background.

In order to separate the contributions from the $t\bar{t}$ and $Z + b\bar{b}$ backgrounds, we used a fit on the invariant mass of the leading di-lepton, m_{12}, shown in Figure 7.1. This distribution, in fact, is flat for events belonging to the $t\bar{t}$ background, while the $Z + b\bar{b}$ events will show a peak at $m_Z = 91.1876$ GeV. The fit on m_{12} is performed using a Chebychev polynomial for the $t\bar{t}$ component and a Breit-Wigner line-shape convolved with a Crystal-Ball resolution function for the Z + jets component. In order to obtain the final estimate of these two backgrounds for our analysis, we must apply a transfer factor[1] (taken from

[1]The transfer factors simply represent the probability that events in the control region can also be found in the signal region, and are thus used to extrapolate our estimates in the control regions to the signal region.

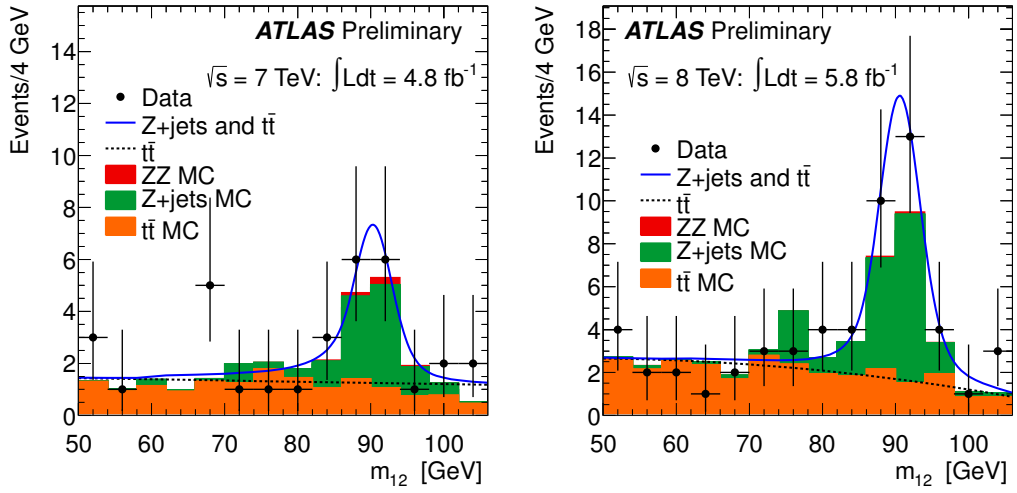

(a) **(b)**

Figure 7.1 m_{12} fit for 2011 (a) and for 2012 (b). The fit consists in a second order Chebychev polynomial for the $t\bar{t}$ component and in a Breit-Wigner convolved with a Crystal-Ball for the Z + jets component. Monte Carlo expectations are also overlaid for comparison: for example it is easy to see that the contribution given by the $ZZ^{(*)}$ irreducible background is very small in this control region.

Monte Carlo) which can account for the passage from this control region to the signal region. The good agreement between data and Monte Carlo for the selections involved has been verified by using $Z + \mu$ events passing the standard $H \to ZZ^{(*)} \to 4\ell$ analysis requirements for the leading di-lepton.

7.1.2 $t\bar{t}$ cross-check using $e\mu + \mu\mu$ control region

We can obtain a cross-check for the contribution of the $t\bar{t}$ background by building a control region where quadruplets are in the form $e^{\pm}\mu^{\mp} + \mu\mu$. If we require the standard analysis requirements except isolation and impact parameter significance on the sub-leading μ pair, we observe the following: 8 events in 2011, which should be compared with the Monte Carlo expectation of 11.0 ± 0.6, and 16 events in 2012, which we should compare with the 18.9 ± 1.1 expected from Monte Carlo. The extrapolated result in the signal region is shown in Table 7.1 for 2011 and in Table 7.2 for 2012.

7.1.3 Final overview

A complete overview of these background estimations for 2011 and 2012 is shown in Table 7.1 and Table 7.2.

Table 7.1 Overview of all background estimations for the $\ell\ell + \mu\mu$ channels of the 2011 data analysis. The methods for $\ell\ell + \mu\mu$ channels are described in Section 7.1.

Method	Estimated number of events in signal region	
	4μ	$2e2\mu$
m_{12} fit: Z + jets contribution	$0.25 \pm 0.10 \pm 0.08$	$0.20 \pm 0.08 \pm 0.06$
m_{12} fit: $t\bar{t}$ contribution	$0.022 \pm 0.010 \pm 0.011$	$0.020 \pm 0.009 \pm 0.011$
$t\bar{t}$ from $e^{\pm}\mu^{\mp} + \mu^{\pm}\mu^{\mp}$	$0.025 \pm 0.009 \pm 0.014$	$0.024 \pm 0.009 \pm 0.014$

Table 7.2 Overview of all background estimations for the $\ell\ell + \mu\mu$ channels of the 2012 data analysis. The methods for $\ell\ell + \mu\mu$ channels are described in Section 7.1.

Method	Estimated number of events in signal region	
	4μ	$2e2\mu$
m_{12} fit: Z + jets contribution	$0.51 \pm 0.13 \pm 0.16$	$0.41 \pm 0.10 \pm 0.13$
m_{12} fit: $t\bar{t}$ contribution	$0.044 \pm 0.015 \pm 0.015$	$0.040 \pm 0.013 \pm 0.013$
$t\bar{t}$ from $e^{\pm}\mu^{\mp} + \mu^{\pm}\mu^{\mp}$	$0.058 \pm 0.015 \pm 0.019$	$0.051 \pm 0.013 \pm 0.017$

7.2 Estimation of the $\ell\ell + ee$ background

7.2.1 Introduction

In general, the background to isolated electrons such as those produced by the decay of a Z boson includes jets, non-isolated electrons from b, c quark decays and background electrons from Dalitz decays or photon conversions originating from neutral pion decays. The classification of electron candidates based on Monte Carlo truth is crucial for any background study and has already been partially presented in Section 5.1. Also in this case, the official ATLAS truth matching and classification tool is used. The truth categories we can define are:

Isolated electrons (e)

An electron is classified as isolated if it matches a true electron originating from the decay of a Z or a W boson.

Non-isolated electrons (Q)

The electron should match a true electron originating from the decay of a b or c.

Background electrons (γ)

The electron must match a true electron originating from a photon. These electrons could be further divided depending upon the origin of the photon, for example the photon may arise from the decay of a π^0, from

the Bremsstrahlung cascade of an isolated electron, or from initial or final state radiation.

Fakes (j or f)

If an electron does not match any of the above categories and it does not even match a muon or tau, it is classified as a fake.

The composition obtained using ALPGEN Z + jets and $Z + b\bar{b}$ Monte Carlo, after applying the full analysis criteria with the exception of electron identification, isolation and impact parameter significance on the sub-leading pair is shown in Figure 7.2. In particular we show in Figure 7.2a the distribution only for sub-leading pairs where the two electrons have opposite charges, while in Figure 7.2b the same is done for electron pairs with the same charge. The numbers for the events in each category are also reported in Table 7.3 and show that, within errors, the yields for the same-sign and opposite-sign pairs are compatible for all categories except the $Z_2 \to QQ$, as we would expect since there are charge correlations in the production of two b quarks.The sum of this two sub-set is shown in Figure 7.2c. Several methods for estimating the background in the $4e$ and $2\mu 2e$ channels have been developed and they will be fully covered in the following Sections.

7.2.2 $\ell\ell + ee$ background estimation using categories

This method uses two different control regions, both highly rich with background. The first one is named $Z + XX$ and indicates a quadruplet which is required to pass all the standard analysis cuts except for the additional selections (see Section 6.5) on the sub-leading pair, the XX part. This control region is needed to estimate the composition of the background and may suffer from low statistics: for this reason electron requirements have been relaxed on the sub-leading pair. Such a control region allows us to estimate all non-$ZZ^{(*)}$ backgrounds and thus the contribution from the $ZZ^{(*)}$ irreducible background will have to be subtracted from our final estimation. The second control region is usually denoted as $Z + X$ and it is formed by a Z (that passes all the analysis requirements for the leading pair) and one additional electron. This control region provides a lot of statistics and allows us to estimate the trans-

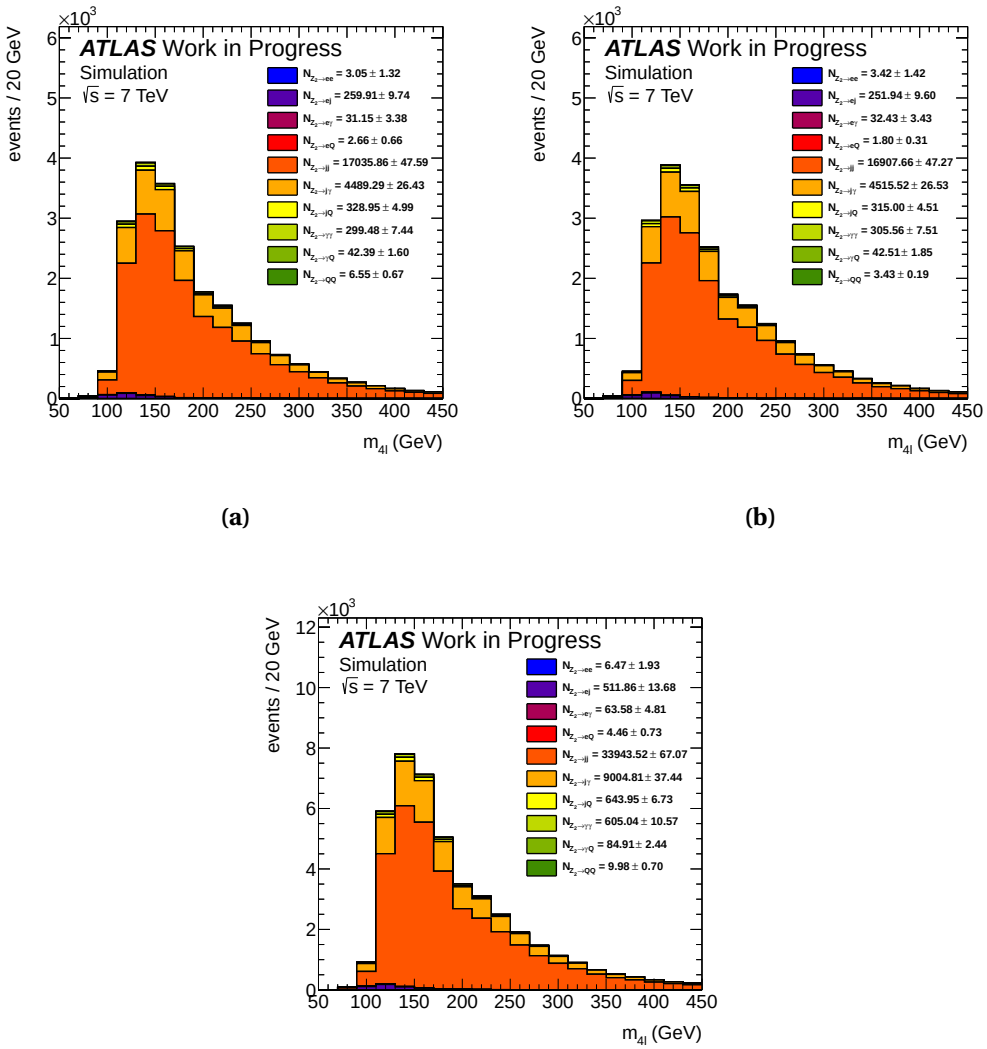

Figure 7.2 $m_{4\ell}$ distribution showing the composition obtained using the $Z + XX$ Monte Carlo (ALPGEN Z + jets and $Z + b\bar{b}$), after applying the full analysis criteria with the exception of electron identification, isolation and impact parameter significance for the sub-leading pair. In (a) for opposite-sign sub-leading pairs, in (b) for same-sign sub-leading pairs and in (c) for the sum of the two.

fer factors when going from the relaxed electron requirements to the analysis requirements.

Table 7.3 Expected number of events from ALPGEN Z + jets and $Z + b\bar{b}$ Monte Carlo, without any global rescaling for the ten different sub-leading di-electron types.

Category	N($Z + X^{\pm}X^{\mp}$)	N($Z + X^{\pm}X^{\pm}$)	N($Z + X^{\pm}X^{\mp}$)-N($Z + X^{\pm}X^{\pm}$)
$Z_2 \to ee$	3.0 ± 1.3	3.4 ± 1.4	-0.4 ± 1.9
$Z_2 \to ej$	260 ± 10	252 ± 10	8 ± 14
$Z_2 \to e\gamma$	31.1 ± 3.4	32.4 ± 3.4	-13 ± 5
$Z_2 \to eQ$	2.7 ± 0.7	1.8 ± 0.3	0.9 ± 0.7
$Z_2 \to jj$	17036 ± 48	16908 ± 47	128 ± 67
$Z_2 \to j\gamma$	4490 ± 26	4516 ± 27	-26 ± 37
$Z_2 \to jQ$	329 ± 5	315.0 ± 4.5	13.9 ± 6.7
$Z_2 \to \gamma\gamma$	299 ± 7	306 ± 7	-6 ± 10
$Z_2 \to \gamma Q$	42.4 ± 1.6	42.5 ± 1.8	-0.1 ± 2.4
$Z_2 \to QQ$	6.5 ± 0.7	3.4 ± 0.2	3.1 ± 0.7

In the $Z + XX$ control region, electron candidates are classified as already shown in Section 7.2.1 but the notation here is different, in order to allow to distinguish between the categorization performed using true Monte Carlo information and the categorization made on data. In this case we separate between **electrons (E)**, **conversions (C)** and **fakes (F)**: this categorization is performed using discriminating variables that have not been already used in the electron identification (see Chapter 5). The categorization is performed as follows:

Electron (E)

We categorize our object as an electron if:

- $f_1 > 0.1$[2]
- there is a b-layer hit (if expected)

[2] f_1 is the fraction of energy deposited in the first layer of the electromagnetic calorimeter:

$$f_1 = \frac{E^{1^{st}sampling}}{\mathrm{E}_T}$$

- if $|\eta| < 2.0$, then $\mathrm{TRT_{Ratio}} > 0.1$ (η-dependent), otherwise $R_\phi > 0.9$[3]

Conversion (C)

If it is not an electron, then it can be identified as a conversion if there is no b-layer hit (when expected) or $\mathrm{n_{hits}^{Pixel}} < 2$ (when a hit in the b-layer is not expected).

Fake (F)

An object is put in the "fakes" category when it has not been categorized as an electron or conversion.

Using this classification, we can combine the two objects of the sub-leading pair into building nine different samples: EE, EC, EF, CE, CC, CF, FE, FC and FF, where the first letter indicates the highest-E_T electron between the two.

In the end, the $Z + XX$ control region is built by not applying the isolation and impact parameter significance cuts on the sub-leading di-lepton (Z_2) and by relaxing the identification cuts on the electrons of this pair. Since we have two different identification menus for 2011 and 2012, the cuts used in the relaxed identification are slightly different:

2011 analysis at $\sqrt{s}$ = 7 TeV

We kept the cuts on $\mathrm{R_{had}}$, R_η, $\mathrm{w}_{\eta 2}$ and $\mathrm{w_{stot}}$ as they are applied in the *loose*++ menu used in the standard analysis.

2012 analysis at $\sqrt{s}$ = 8 TeV

We kept the cuts on $\mathrm{R_{had}}$, R_η, $\mathrm{w}_{\eta 2}$, $\mathrm{w_{stot}}$, f_3, $\Delta\phi_{Res}$ and $\mathrm{TRT_{Ratio}}$ as they are applied in the *MultiLepton* menu used in the standard analysis.

Common to 2011 and 2012

We require that a good track is matched to the electromagnetic cluster, thus we demand $\mathrm{n_{hits}^{Pixel}} \geq 1$ and $\mathrm{n_{hits}^{Silicon}} \geq 7$.

The final number of events falling in each of the nine different categories, for 2011 and 2012 is shown in Table 7.4. In this Table are also shown the

[3] Similarly to R_η, R_ϕ is defined as the ratio between a 3×3 and a 7×7 cluster: $R_\phi = \frac{E_{3\times 3}}{E_{7\times 7}}$. It represents a simple way to determine the width of a shower in the ϕ direction.

Monte Carlo expectations for each category (this time made using truth information as already explained in Section 7.2.1) which show a quite good agreement with what we observe in data.

Table 7.4 Observed yields of the different categories in the $\ell\ell + ee$ control region. Results for both the analysis of 2011 data at $\sqrt{s}$ = 7 TeV and of 2012 data at $\sqrt{s}$ = 8 TeV are shown. Electrons in the sub-leading pair of the $Z + XX$ control region are classified as electrons (E), conversions (C) or fakes (F). Monte Carlo expectations are also shown for comparison.

	2011 analysis at $\sqrt{s}$ = 7 TeV				2012 analysis at $\sqrt{s}$ = 8 TeV			
	$4e$		$2\mu 2e$		$4e$		$2\mu 2e$	
	Data	MC	Data	MC	Data	MC	Data	MC
EE	11	11.2±0.6	8	15.0±0.9	32	22.7±4.8	31	24.9±5.0
EC	4	2.5±0.8	3	3.0±1.1	6	6.0±2.5	2	1.9±1.4
EF	6	9.7±1.4	5	6.6±1.1	18	19.0±4.4	26	15.3±3.9
CE	5	1.5±0.7	6	4.5±1.6	4	8.8±3.0	6	5.1±2.3
CC	2	1.4±0.7	2	1.5±1.0	1	5.3±2.3	6	4.2±2.0
CF	7	4.7±1.2	10	9.9±2.3	12	8.8±3.0	15	15.3±3.9
FE	5	3.1±0.6	4	4.5±1.0	16	5.7±2.4	12	8.4±2.9
FC	5	3.0±1.0	4	6.3±1.8	6	6.5±2.6	7	4.3±2.1
FF	12	11.0±1.9	17	13.4±2.6	12	17.4±4.2	16	33.6±5.8
Total	57	48±3	59	65±5	107	100±10	121	113±11

In order to extrapolate from the $Z + XX$ control region to our signal region for each of the previously defined categories, we extract efficiencies from the $Z + X$ control region, where X satisfies the relaxed criteria used to form the $Z + XX$ sample. These efficiencies are shown in Table 7.5 for the 2011 data analysis and in Table 7.6 for the 2012 data analysis, separately for $Z(\mu\mu) + XX$ and $Z(ee) + XX$. The efficiencies are derived for each of the categories used in the data classification (E, C or F), for each of the possible true origins of the particles (e, Q, γ or j).

The final estimation for the number of background events that will fall in our signal region is obtained simulating toy pseudo-experiments according to the yields in the $Z + XX$ control region and the efficiencies from the $Z + X$

Table 7.5 Efficiency of isolation and impact parameter cuts, as well as the remaining cuts to complete the *loose++* menu which have been used to extrapolate from the $Z + XX$ control region to the signal region in the 2011 data analysis at $\sqrt{s}$ = 7 TeV. Letters E, C and F denote the reconstruction based classification while the other ones, e, Q, γ and j indicate the truth based one.

	e	Q	γ	j
$Z(\mu\mu) + XX$				
Leading Electron				
E	0.983 ± 0.00277	0.256 ± 0.0242	0.39 ± 0.0107	0.296 ± 0.00832
C	0.673 ± 0.0859	0.269 ± 0.0844	0.217 ± 0.00467	0.0841 ± 0.0103
F	0.96 ± 0.0131	0.327 ± 0.0392	0.308 ± 0.0171	0.165 ± 0.00292
Sub-Leading Electron				
E	0.975 ± 0.00577	0.283 ± 0.0195	0.301 ± 0.0133	0.312 ± 0.00819
C	0.626 ± 0.167	0.299 ± 0.0737	0.187 ± 0.00452	0.061 ± 0.00785
F	0.941 ± 0.0325	0.34 ± 0.039	0.262 ± 0.0182	0.128 ± 0.00296
$Z(ee) + XX$				
Leading Electron				
E	0.968 ± 0.00584	0.293 ± 0.0261	0.368 ± 0.0149	0.283 ± 0.0109
C	0.616 ± 0.112	0.183 ± 0.0843	0.198 ± 0.00537	0.0779 ± 0.0119
F	0.96 ± 0.0175	0.316 ± 0.0464	0.33 ± 0.0193	0.181 ± 0.00363
Sub-Leading Electron				
E	0.942 ± 0.0114	0.303 ± 0.0238	0.295 ± 0.0164	0.189 ± 0.0108
C	0.599 ± 0.21	0.235 ± 0.0816	0.172 ± 0.00545	0.0682 ± 0.00964
F	0.897 ± 0.0721	0.343 ± 0.0472	0.245 ± 0.0238	0.102 ± 0.00292

control region. For each experiment, we generate independently each background component using Poisson statistics. The obtained results are shown in Table 7.7; the largest uncertainty is always due to the fluctuations in the composition of the control region sample. Systematic uncertainties reflect the limited statistics in the Monte Carlo, which we used both for classification and for extrapolation.

Table 7.6 Efficiency of isolation and impact parameter cuts, as well as the remaining cuts to complete the *MultiLepton* menu which have been used to extrapolate from the $Z+XX$ control region to the signal region in the 2012 data analysis at $\sqrt{s}$ = 8 TeV. Letters E, C and F denote the reconstruction based classification while the other ones, e, Q, γ and j indicate the truth based one.

	e	Q	γ	j
$Z(\mu\mu)+XX$				
Leading Electron				
E	0.974 ± 0.006	0.181 ± 0.018	0.247 ± 0.007	0.210 ± 0.005
C	0.827 ± 0.117	0.187 ± 0.103	0.317 ± 0.005	0.122 ± 0.013
F	0.956 ± 0.026	0.204 ± 0.037	0.191 ± 0.010	0.163 ± 0.002
Sub-Leading Electron				
E	0.965 ± 0.011	0.207 ± 0.018	0.178 ± 0.007	0.116 ± 0.004
C	0.700 ± 0.329	0.252 ± 0.076	0.245 ± 0.005	0.068 ± 0.009
F	0.907 ± 0.096	0.282 ± 0.036	0.158 ± 0.010	0.106 ± 0.002
$Z(ee)+XX$				
Leading Electron				
E	0.839 ± 0.017	0.172 ± 0.023	0.229 ± 0.008	0.201 ± 0.006
C	0.695 ± 0.017	0.104 ± 0.081	0.258 ± 0.006	0.074 ± 0.012
F	0.633 ± 0.044	0.385 ± 0.063	0.188 ± 0.010	0.196 ± 0.003
Sub-Leading Electron				
E	0.796 ± 0.026	0.232 ± 0.021	0.171 ± 0.009	0.124 ± 0.005
C	0.632 ± 0.016	0.150 ± 0.084	0.181 ± 0.005	0.052 ± 0.009
F	0.505 ± 0.049	0.441 ± 0.049	0.114 ± 0.011	0.111 ± 0.002

7.2.3 $\ell\ell+ee$ background estimation using categories: $Z+X^{\pm}X^{\pm}$ control region

We have applied the same principles of the method just described to the case where the $Z+XX$ control region has only same-sign sub-leading pairs, as a cross check of the method. The background estimations provided by this version of the categories method are shown in Table 7.8.

Table 7.7 Final estimation provided by the categories method. The systematic uncertainties come from the limited statistics in the Monte Carlo used for the determination of the transfer factors.

Estimated events in signal region		
	2011 analysis at $\sqrt{s}$ = 7 TeV	2012 analysis at $\sqrt{s}$ = 8 TeV
$4e$ channel	$3.1 \pm 0.6 \pm 0.5$	$3.9 \pm 0.7 \pm 0.8$
$2\mu 2e$ channel	$2.6 \pm 0.4 \pm 0.4$	$4.9 \pm 0.8 \pm 0.7$

Table 7.8 Final estimation provided by the categories method when asking the subleading pair to have same-sign electrons. The systematic uncertainties come from the limited statistics in the Monte Carlo used for the determination of the transfer factors.

Estimated events in signal region		
	2011 analysis at $\sqrt{s}$ = 7 TeV	2012 analysis at $\sqrt{s}$ = 8 TeV
$4e$ channel	$3.2 \pm 0.6 \pm 0.5$	$3.1 \pm 0.5 \pm 0.6$
$2\mu 2e$ channel	$3.7 \pm 0.9 \pm 0.6$	$4.1 \pm 0.6 \pm 0.8$

7.2.4 $\ell\ell + ee$ background estimation using same sign events

In the plots in Figure 7.2 we have shown an example of the composition in the $Z + XX$ background estimation. The pure Monte Carlo expected number of events (without any rescaling) for each combination of the four categories (ee, ej, eγ, eQ, jj, jγ, jQ, $\gamma\gamma$, γQ, QQ) has been compiled in Table 7.3.

We expect real electrons (e), conversions (γ) and fakes (j) not to show any dependence on the charge, while the same cannot be stated for the $Z_2 \to QQ$ contribution, which should favor the production of opposite sign electrons, since b quarks are produced in pairs of quark-antiquark. This is clearly reflected in the numbers shown in Table 7.3 which have been obtained by not applying the electron identification, isolation and impact parameter significance selections, in the attempt of increasing the available statistics. These numbers allow us, since the $Z_2 \to QQ$ is expected to be very small, to give an estimation of the background for $\ell\ell + ee$ channels using events with quadru-

plets that satisfy all the analysis requirements but have same sign sub-leading pairs. Of course this method suffers heavily from low statistics and can thus be used only as a cross check. When applying the standard analysis requirements and inverting the charge requirement on the sub-leading pair, we end up with:

2011 analysis at $\sqrt{s}$ = 7 TeV

4 events in the $4e$ channel and 2 events in the $2\mu 2e$ channel.

2012 analysis at $\sqrt{s}$ = 8 TeV

4 events in the $4e$ channel and 7 events in the $2\mu 2e$ channel.

7.2.5 $\ell\ell + ee$ background estimation using $3\ell + X$ control region

The composition problem, seen in Section 7.2.2, can be simplified by constructing a control region where three of the electrons satisfy the analysis requirements. We indicate this new control region as $3\ell+X$ because our quadruplets are built by applying the standard analysis requirements on the three highest-p_T leptons in the event and only the standard hits requirement for the track, $n_{\text{hits}}^{\text{Silicon}} \geq 7$ and $n_{\text{hits}}^{\text{Pixel}} \geq 1$, are required on the fourth. We require same sign sub-leading pairs in the attempt of getting rid of the $ZZ^{(*)}$ irreducible background. The yields of events shown in Table 7.3 prove that this change will not affect our final estimation.

The simplified composition problem allows us to use a two-dimensional fit to obtain the yields for the different components. The discriminating variables used to perform the fit are $n_{\text{hits}}^{b\text{-layer}}$, $\text{TRT}_{\text{Ratio}}$ and f_1. The number of hits in the b-layer is used in all the regions of the detector, while $\text{TRT}_{\text{Ratio}}$ can be used only in the barrel and is replaced by f_1 in the endcap. In order to improve the available statistics, the templates for these three variables have been taken from the $Z + X$ control region already introduced in Section 7.2.2. Moreover, they have been re-weighted to take into account the difference between the p_T distribution in the $3\ell + X$ and $Z + X$ control region.

The fit has been improved by reducing the very high component of fakes, introducing a cut on R_η on data events observed in the $3\ell + X$ control region.

The results for the fit are shown in Table 7.9 and in Table 7.10, as well as the efficiencies obtained from $Z+X$ events to extrapolate to the signal region and the final estimated events.

Table 7.9 Results for the fitting procedure on 2011 data at $\sqrt{s}$ = 7 TeV. The yields in the $3\ell + X$ control region, the extrapolation efficiencies and the final number of expected events in the signal region are shown for each single component.

2011 data at $\sqrt{s}$ = 7 TeV			
	Yield from fit	Extrapolation efficiency	Final estimate
		$4e$	
j	$63.60\ ^{+8.61}_{-7.94}$	0.0190 ± 0.0010	$1.21\ ^{+0.16}_{-0.15}$
Q	$1.01\ ^{+0.49}_{-0.49}$	0.1987 ± 0.0099	$0.20\ ^{+0.10}_{-0.10}$
γ	$8.32\ ^{+4.06}_{-3.61}$	0.0995 ± 0.0050	$0.83\ ^{+0.40}_{-0.36}$
		$2\mu 2e$	
j	$61.10\ ^{+8.33}_{-7.67}$	0.0202 ± 0.0010	$1.23\ ^{+0.17}_{-0.15}$
Q	$1.41\ ^{+0.68}_{-0.68}$	0.2142 ± 0.0107	$0.30\ ^{+0.15}_{-0.15}$
γ	$3.48\ ^{+2.93}_{-2.48}$	0.1000 ± 0.0050	$0.35\ ^{+0.29}_{-0.25}$

Table 7.10 Results for the fitting procedure on 2012 data at $\sqrt{s}$ = 8 TeV. The yields in the $3\ell + X$ control region, the extrapolation efficiencies and the final number of expected events in the signal region are shown for each single component.

2012 data at $\sqrt{s}$ = 8 TeV			
	Yield from fit	Extrapolation efficiency	Final estimate
		$4e$	
j	$117.00\ ^{+11.80}_{-11.10}$	0.0126 ± 0.0013	$1.48\ ^{+0.15}_{-0.14}$
Q	$1.79\ ^{+0.77}_{-0.77}$	0.1774 ± 0.0177	$0.32\ ^{+0.14}_{-0.14}$
γ	$19.50\ ^{+6.39}_{-5.93}$	0.0592 ± 0.0059	$1.15\ ^{+0.38}_{-0.35}$
		$2\mu 2e$	
j	$100.00\ ^{+11.40}_{-10.70}$	0.0135 ± 0.0013	$1.35\ ^{+0.15}_{-0.14}$
Q	$2.46\ ^{+1.07}_{-1.07}$	0.1686 ± 0.0169	$0.41\ ^{+0.18}_{-0.18}$
γ	$31.70\ ^{+7.81}_{-7.40}$	0.0536 ± 0.0054	$1.70\ ^{+0.42}_{-0.40}$

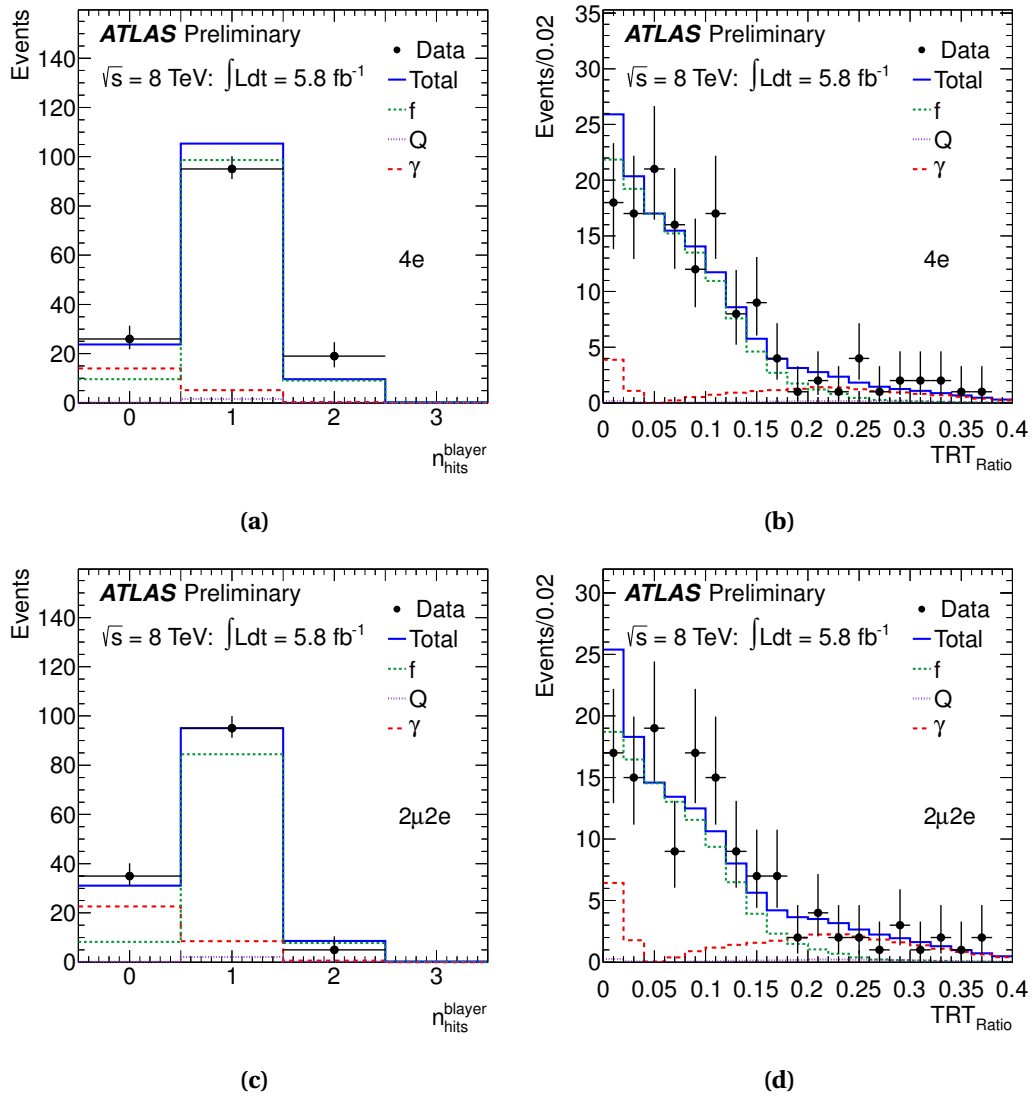

Figure 7.3 Simultaneous fit results to $n_{\text{hits}}^{b\text{-layer}}$ in (a) and (c) and to $\text{TRT}_{\text{Ratio}}$ in (b) and (d) for the analysis of 2012 data at $\sqrt{s}$ = 8 TeV. In plots (a) and (b) is shown the simultaneous fit for the $4e$ channel background estimation, while in (c) and (d) the same is shown for the $2\mu 2e$ channel. The different background sources are denoted as follows: fakes (f), photon conversions (γ) and electrons from semi-leptonic decays of heavy quarks (Q).

As an example of the simultaneous fits, we show the results of the analysis of 2012 data at $\sqrt{s}$ = 8 TeV in Figure 7.3.

The final result obtained is shown in Table 7.11:

Table 7.11 Final estimation provided by the $3\ell + X$ control region method. The systematic uncertainties come from fits performed on other test variables, such as $\Delta\eta_1$, and from the uncertainty on the extrapolation coefficients.

Estimated events in signal region		
	2011 analysis at $\sqrt{s}$ = 7 TeV	2012 analysis at $\sqrt{s}$ = 8 TeV
$4e$ channel	$2.2 \pm 0.5 \pm 0.3$	$3.0 \pm 0.4 \pm 0.4$
$2\mu 2e$ channel	$1.9 \pm 0.4 \pm 0.4$	$3.5 \pm 0.5 \pm 0.5$

where the systematic effects come from substituting $\mathrm{TRT}_{\mathrm{Ratio}}$ with $\Delta\eta_1$ in the fitting procedure as well as from the uncertainties on the efficiencies needed to pass from the $3\ell + X$ control region yields to the number of expected events in the signal region. There are (although small) correlations between the three different background sources in the fit: nevertheless, the final statistical uncertainty has been taken as the quadratic sum of the three, in a conservative way.

7.2.6 Final overview

A complete overview of the background estimations for $\ell\ell + ee$ channels in both 2011 and 2012 is shown in Table 7.12 and Table 7.13.

Table 7.12 Overview of all background estimations for the $\ell\ell + ee$ channels of the 2011 data analysis at $\sqrt{s}$ = 7 TeV. The methods for $\ell\ell + ee$ channels are described in Section 7.2.

Method	Estimated events in signal region	
	$4e$	$2\mu 2e$
Categories with $\ell\ell + e^{\pm}e^{\mp}$	$3.1 \pm 0.6 \pm 0.5$	$2.6 \pm 0.4 \pm 0.4$
Categories with $\ell\ell + e^{\pm}e^{\pm}$	$3.2 \pm 0.6 \pm 0.5$	$3.7 \pm 0.9 \pm 0.6$
$3\ell + X$ control region	$2.2 \pm 0.5 \pm 0.3$	$2.0 \pm 0.5 \pm 0.3$
Same sign events	4 ± 2	2.0 ± 1.4

Table 7.13 Overview of all background estimations for the $\ell\ell + ee$ channels of the 2012 data analysis at $\sqrt{s}$ = 8 TeV. The methods for $\ell\ell + ee$ channels are described in Section 7.2.

Method	Estimated events in signal region	
	$4e$	$2\mu 2e$
Categories with $\ell\ell + e^{\pm}e^{\mp}$	$3.9 \pm 0.7 \pm 0.8$	$4.9 \pm 0.8 \pm 0.7$
Categories with $\ell\ell + e^{\pm}e^{\pm}$	$3.1 \pm 0.5 \pm 0.6$	$4.1 \pm 0.6 \pm 0.8$
$3\ell + X$ control region	$3.0 \pm 0.4 \pm 0.4$	$3.5 \pm 0.5 \pm 0.5$
Same sign events	4 ± 2	7.0 ± 2.6

7.3 Control plots

The final control over our background estimates is done with the plots in Figure 7.4. These plots have been made by removing the isolation and impact parameter significance requirements on the sub-leading pair. For the different backgrounds, Monte Carlo has been used for the m_{12} and m_{34} shapes, which have been rescaled using the data-driven background estimations explained in this Chapter. These plots allow us to check, in an enlarged signal region, the good agreement between data and our expectations. In Figure 7.4a and in Figure 7.4b are shown the m_{12} and m_{34} distributions for the $\ell\ell + \mu\mu$ channels, while in Figure 7.4c and in Figure 7.4d are shown the m_{12} and m_{34} distributions for the $\ell\ell + ee$ channels.

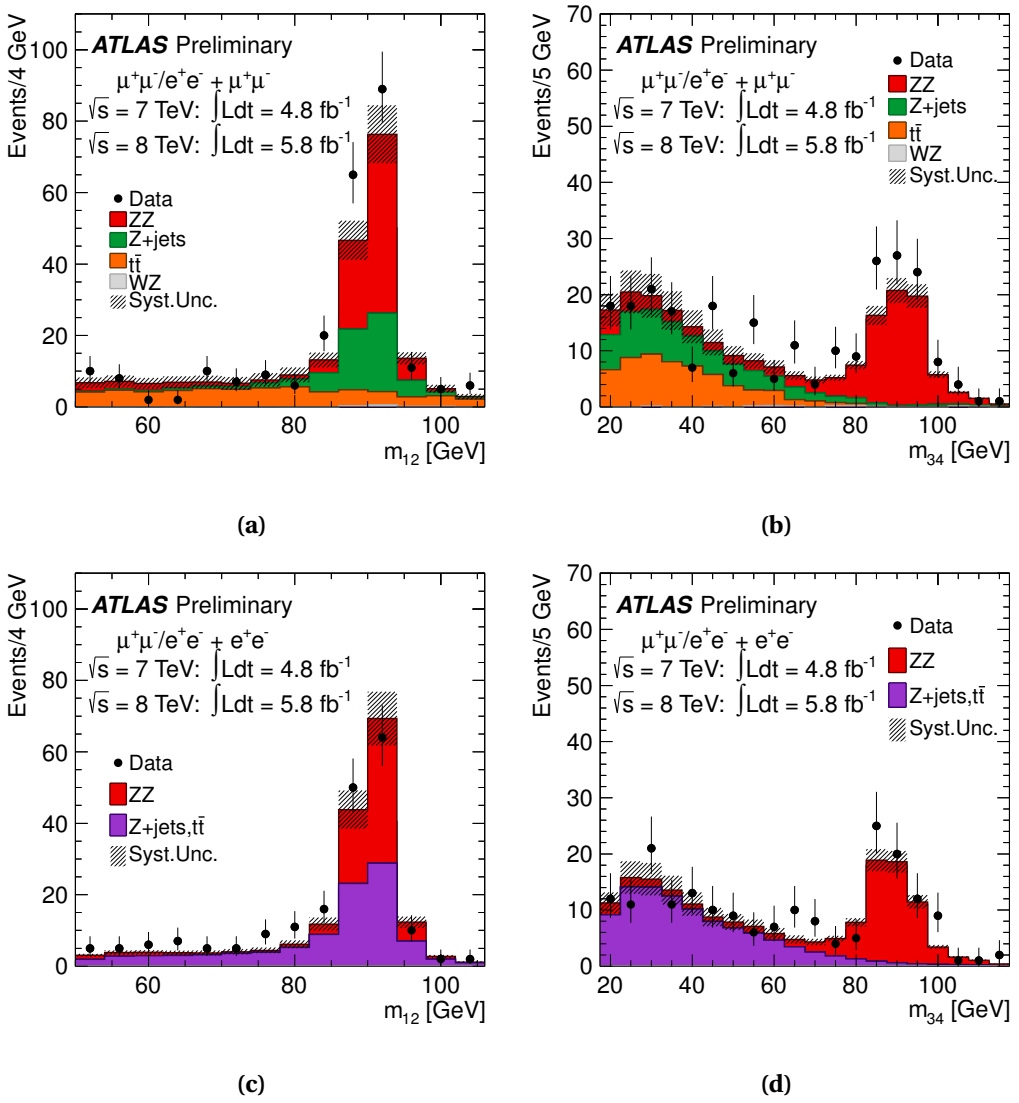

Figure 7.4 Invariant mass distributions of the lepton pairs in the control sample defined by a Z boson candidate and an additional same-flavor lepton pair, for the $\sqrt{s}$ = 7 TeV and $\sqrt{s}$ = 8 TeV datasets combined. The sample is divided according to the flavor of the additional lepton pair. In (a) the m_{12} and in (b) the m_{34} distributions are presented for $\ell\ell + \mu\mu$ events. In (c) the m_{12} and in (d) the m_{34} distributions are presented for $\ell\ell + ee$ events. The kinematic selection of the analysis is applied. Isolation and impact parameter significance requirements are applied to the first lepton pair only. The Monte Carlo is normalized to the data driven background estimations.

Chapter 8

$H \to ZZ^{(*)} \to 4\ell$ analysis: results

8.1 Results for the event selection

In Table 8.1, the number of events observed in each final state is summarized and compared to the expected backgrounds, separately for $m_{4\ell}$ <160 GeV and $m_{4\ell}$ ≥160 GeV, and to the expected signal for various m_H hypotheses, for 2011 data. The same is done in Table 8.2 for 2012 data. Table 8.3 presents the observed and expected events, in a window of ±5 GeV around various hypothesized Higgs boson masses, for the 4.8 fb^{-1} at $\sqrt{s}$ = 7 TeV and the 5.8 fb^{-1} at $\sqrt{s}$ = 8 TeV datasets as well as for their combination.

The expected $m_{4\ell}$ distributions for the total background and several signal hypotheses are compared to the data in Figure 8.1. In particular in (a) and (c) are shown the results for the analysis of 2011 data, while in (b) and (d) are shown the results for the analysis of 2012 data. Two different mass ranges are adopted for these comparisons: the complete mass range for the analysis (80-600 GeV) is shown in (a) and (b), while a zoom on the low mass region (80-250 GeV) is shown in (c) and (d). The combination of the 2011 and 2012 datasets is shown, instead, in Figure 8.2 for both the complete mass range (Figure 8.2a) and the enlarged view of the low mass region (Figure 8.2b).

Table 8.1 The observed numbers of events and the final estimate for the expected backgrounds, separated into "Low mass" ($m_{4\ell}$ <160 GeV) and "High mass" ($m_{4\ell}$ ≥160 GeV) regions for the analysis of 2011 data at $\sqrt{s}$ = 7 TeV. The expected numbers of signal events is also shown for various Higgs boson mass hypotheses. For signal and background estimates, the corresponding total uncertainty is given.

	4μ		$2e2\mu/2\mu2e$		$4e$	
	Low mass	High mass	Low mass	High mass	Low mass	High mass
$ZZ^{(*)}$	4.9±0.2	18.1±1.3	3.1±0.2	27.3±2.0	1.6±0.2	10.2±0.8
Z + jets, $t\bar{t}$	0.2±0.1	0.07±0.03	2.1±0.5	0.7±0.2	2.3±0.6	0.8±0.2
Background	5.1±0.2	18.2±1.3	5.1±0.5	28.0±2.0	3.9±0.6	11.0±0.8
Data	8	25	5	28	4	18
m_H=125 GeV	1.0±0.1		1.0±0.1		0.37±0.05	
m_H=150 GeV	3.0±0.4		3.4±0.5		1.4±0.2	
m_H=190 GeV	5.1±0.6		7.4±1.0		2.8±0.4	
m_H=400 GeV	2.3±0.3		3.8±0.5		1.6±0.2	

Table 8.2 The observed numbers of events and the final estimate for the expected backgrounds, separated into "Low mass" ($m_{4\ell}$ <160 GeV) and "High mass" ($m_{4\ell}$ ≥160 GeV) regions for the analysis of 2012 data at $\sqrt{s}$ = 8 TeV. The expected numbers of signal events is also shown for various Higgs boson mass hypotheses. For signal and background estimates, the corresponding total uncertainty is given.

	4μ		$2e2\mu/2\mu2e$		$4e$	
	Low mass	High mass	Low mass	High mass	Low mass	High mass
$ZZ^{(*)}$	6.3±0.3	27.5±1.9	3.7±0.2	41.7±3.0	2.9±0.3	17.7±1.4
Z + jets, $t\bar{t}$	0.4±0.2	0.15±0.07	3.9±0.9	1.4±0.3	2.9±0.8	1.0±0.3
Background	6.7±0.3	27.6±1.9	7.6±1.0	43.1±3.0	5.7±0.8	18.8±1.4
Data	4	34	11	61	7	25
m_H=125 GeV	1.4±0.2		1.7±0.2		0.8±0.1	
m_H=150 GeV	4.5±0.6		5.9±0.8		2.7±0.4	
m_H=190 GeV	8.2±1.0		12.5±1.7		5.3±0.8	
m_H=400 GeV	3.9±0.5		6.6±0.9		2.9±0.4	

Table 8.3 The numbers of expected signal and background events together with the number of observed events, in a window of ±5 GeV around the hypothesized Higgs boson mass for the 4.8 fb^{-1} at $\sqrt{s}$ = 7 TeV dataset, the 5.8 at $\sqrt{s}$ = 8 TeV dataset and their combination.

	$\sqrt{s}$ = 7 TeV			$\sqrt{s}$ = 8 TeV			$\sqrt{s}$ = 7 TeV and $\sqrt{s}$ = 8 TeV		
				4μ					
m_H	exp. signal	exp. bkg	obs	exp. signal	exp. bkg	obs	exp. signal	exp. bkg	obs
120	0.48±0.06	0.46± 0.03	2	0.68±0.09	0.61±0.04	2	1.16±0.15	1.07±0.07	4
125	0.84±0.11	0.56± 0.03	2	1.25±0.17	0.74±0.05	4	2.09±0.28	1.30±0.08	6
130	1.38±0.18	0.63± 0.03	1	1.88±0.25	0.81±0.05	2	3.26±0.43	1.44±0.08	3
				$2e2\mu/2\mu2e$					
m_H	exp. signal	exp. bkg	obs	exp. signal	exp. bkg	obs	exp. signal	exp. bkg	obs
120	0.48±0.07	0.78± 0.10	1	0.81±0.12	1.15±0.17	2	1.29±0.19	1.93±0.18	3
125	0.83±0.11	0.89± 0.11	2	1.45±0.20	1.30±0.19	3	2.28±0.31	2.19±0.21	5
130	1.27±0.17	0.94± 0.11	1	2.24±0.32	1.34±0.20	2	3.51±0.49	2.28±0.21	3
				$4e$					
m_H	exp. signal	exp. bkg	obs	exp. signal	exp. bkg	obs	exp. signal	exp. bkg	obs
120	0.15±0.02	0.60±0.12	1	0.35±0.05	0.79±0.15	1	0.50±0.07	1.39±0.19	2
125	0.28±0.04	0.69±0.13	0	0.61±0.09	0.90±0.17	2	0.89±0.13	1.59±0.22	2
130	0.42±0.06	0.74±0.14	0	0.91±0.15	0.96±0.17	1	1.33±0.21	1.70±0.22	1

8.2 Systematic uncertainties

Before extracting any information from the plots shown in Figure 8.1, we summarize all the systematic effects taken into account in the analysis being presented:

Electron reconstruction and identification

The electron reconstruction and identification efficiencies give rise to an uncertainty on the normalization of the whole mass spectrum of 4.5% for 2012 and of 4% for 2011.

Electron additional selections

The studies conducted on the additional selections, isolation and impact parameter significance, which have been discussed in Section 6.5, show that particular attention must be paid in the region E_T< 15 GeV for 2012 data at $\sqrt{s}$ = 8 TeV. For this reason a 4% systematic for electrons in

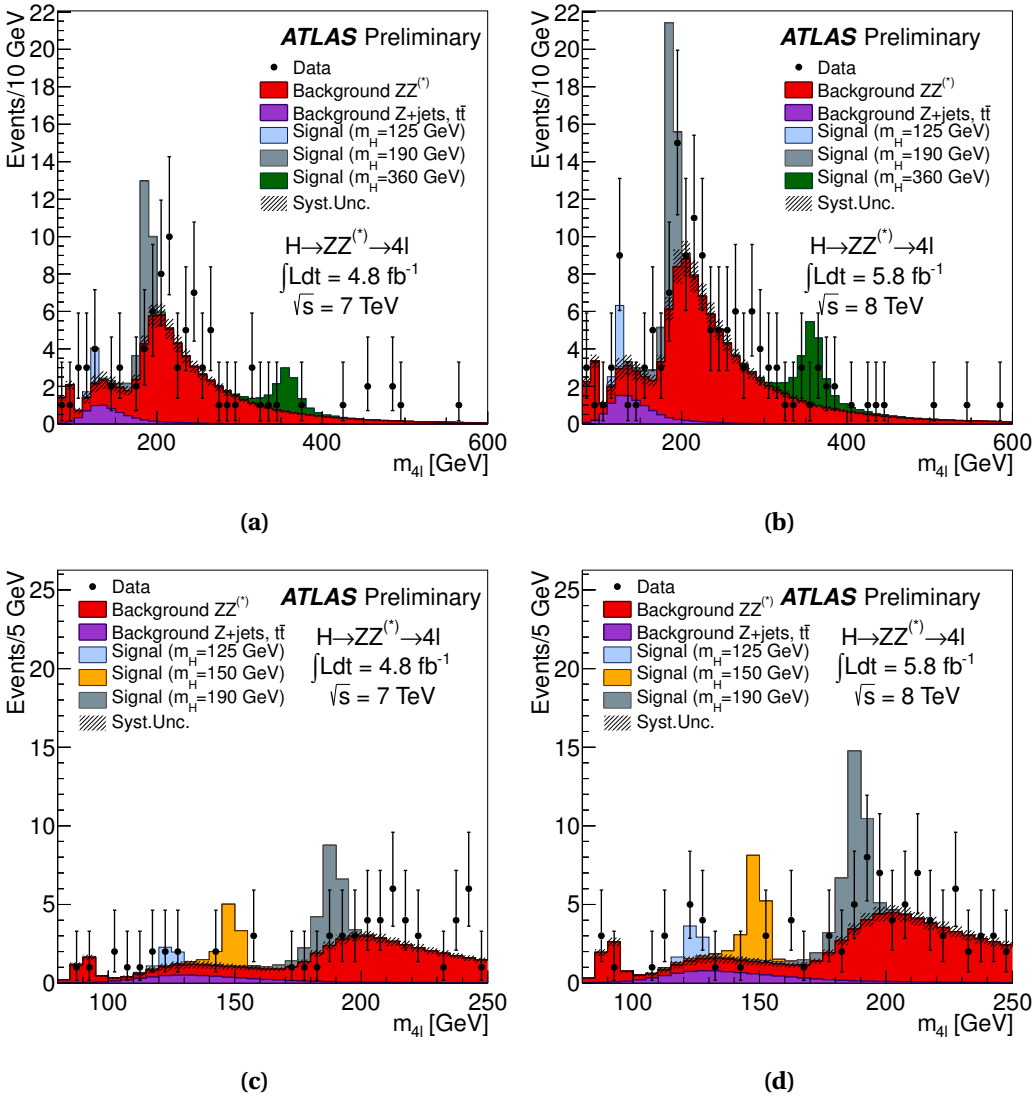

Figure 8.1 The distribution of the four-lepton invariant mass, $m_{4\ell}$, for the 2011 analysis in (a) for the mass range 80-600 GeV and in (c) for the mass range 80-250 GeV and for the 2012 analysis in (b) for the mass range 80-600 GeV and in (d) for the mass range 80-250 GeV, compared to the background expectation. Error bars represent 68.3% central confidence intervals. In (c) and (d) the signal expectation for m_H = 125, 150, 190 GeV is shown while in (a) and (b) the signal expectation for m_H = 125, 190, 360 GeV is shown.

the barrel and 2% for electrons in the crack and in the endcap has been added.

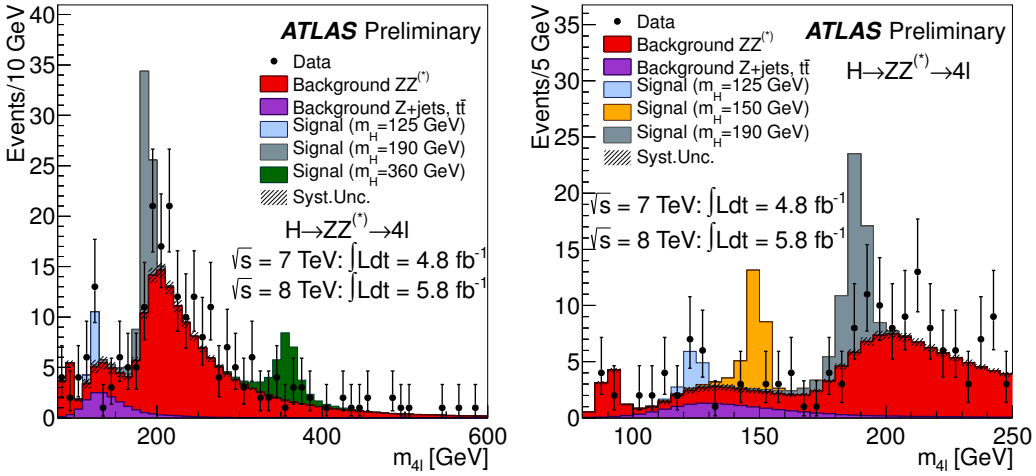

(a) **(b)**

Figure 8.2 $m_{4\ell}$ distribution for the combined dataset, in (a) for the mass range 80-600 GeV and in (b) for the mass range 80-250 GeV. In (b) the signal expectation for m_H = 125, 150, 190 GeV is shown while in (a) the signal expectation for m_H = 125, 190, 360 GeV is shown.

Electron energy scale

The impact of the electron energy scale has been found to be very small, 0.7% for $4e$ and 0.4% for the mixed channel on the $m_{4\ell}$ scale.

Muon identification efficiency

The effect of the muon identification efficiency uncertainty gives rise to an error on the normalization of 0.11%, averaged on the complete mass spectrum.

Muon momentum scale and resolution

These uncertainties are found to be less than 1% and thus negligible.

Background estimations

The systematic errors arising from the different background estimation techniques have been explained in Chapter 7.

Cross sections

All theoretical uncertainties concerning the Higgs boson production cross sections have already been detailed in Section 6.1.

Luminosity

The uncertainty given on the overall normalization by the integrated luminosity is 1.8% for 2011 and 3.6% for 2012.

PDF and QCD scale uncertainties

In the case of 2011 data, we computed the systematic uncertainty arising from these two effects, by varying the Higgs boson p_T spectrum accordingly. The signal kinematics modeling has been improved for the 2012 data analysis and this systematic uncertainty is no longer needed.

8.3 Upper limits on the Higgs boson production cross section

In order to derive upper limits on the Higgs boson production cross section at 95% CL, we use the modified frequentist confidence level, CL_s, with the profile likelihood test statistic. A perfect choice for inspecting the presence of a signal in a sample is, in fact, the likelihood ratio between the signal plus background hypothesis ($s+b$) and the background only hypothesis (b). The first one is the probability that the observed events, n_i, are compatible with the $s+b$ hypothesis while the second is the probability that n_i is compatible with the background only hypothesis. We can consider each of our channels as an independent experiment and thus we can write, for N independent experiments, the following likelihood ratio:

$$Q = \prod_{i=1}^{N} \frac{\mathscr{P}(n_i \mid s_i + b_i)}{\mathscr{P}(n_i \mid b_i)} = \prod_{i=1}^{N} \left(1 + \frac{s_i}{b_i}\right)^{n_i} \cdot e^{-s_i} \tag{8.1}$$

It is more useful to use, in these cases, the logarithmic likelihood ratio:

$$\ln Q = \sum_{i=1}^{N} \left[-s_i + n_i \ln\left(1 + \frac{s_i}{b_i}\right)\right] \tag{8.2}$$

where we identified with s_i the number of expected signal events, with b_i the expected number of background events and with n_i the observed number of events. At this point the confidence level for excluding the signal plus background hypothesis is given by:

$$CL_{s+b} = \mathscr{P}_{s+b}(\ln Q \leq \ln Q_{obs}) \tag{8.3}$$

and, in an analogous way, the confidence level for excluding the background only hypothesis is:

$$CL_b = \mathscr{P}_b(\ln Q \leq \ln Q_{obs}) \tag{8.4}$$

The modified frequentist confidence level, CL_s, is obtained by the ratio of Equation 8.3 and Equation 8.4:

$$CL_s = \frac{CL_{s+b}}{CL_b} \tag{8.5}$$

and it can be used to extract upper limits on the Higgs boson production cross section.

The following plots show both the observed CL_s (full line) and the expected CL_s (dashed line) in terms of the 95% CL limit on $\sigma/\sigma_{\mathrm{SM}}$. This particular scale is very useful since it allows us to directly obtain the excluded regions at 95% CL: if the observed CL_s line lies below one in a specific point, this means that our experimental sensitivity is sufficient for probing the existence of a Higgs boson with that mass but none has been observed.

These results, of course, make use of the theoretical inputs on the production cross sections and branching ratios, which we already presented in Chapter 1. The upper limit plots are finally shown in Figure 8.3 for 2011 data, in Figure 8.4 for 2012 data and in Figure 8.5 for the two datasets combined.

If we thus concentrate on the plots in Figure 8.5 we can observe that, by combining the 2011 and 2012 datasets we are able to exclude the presence of a Standard Model Higgs boson at 95% CL in the mass ranges 131-162 GeV and 170-460 GeV, while we would expect to exclude it in the ranges 124-164 GeV and 176-500 GeV. Apart from the ranges excluded, these plots (especially the zoom in the low mass region, Figure 8.5b) show that there is a significant excess of events around m_H = 125 GeV. The following Section illustrates the technique used to estimate the significance of such excess.

8.4 Significance of the excess

In order to quantify the significance of the excess observed consistently in 2011 and 2012 data in the low mass region, the best test is represented by the probability that a background-only experiment is more signal-like than

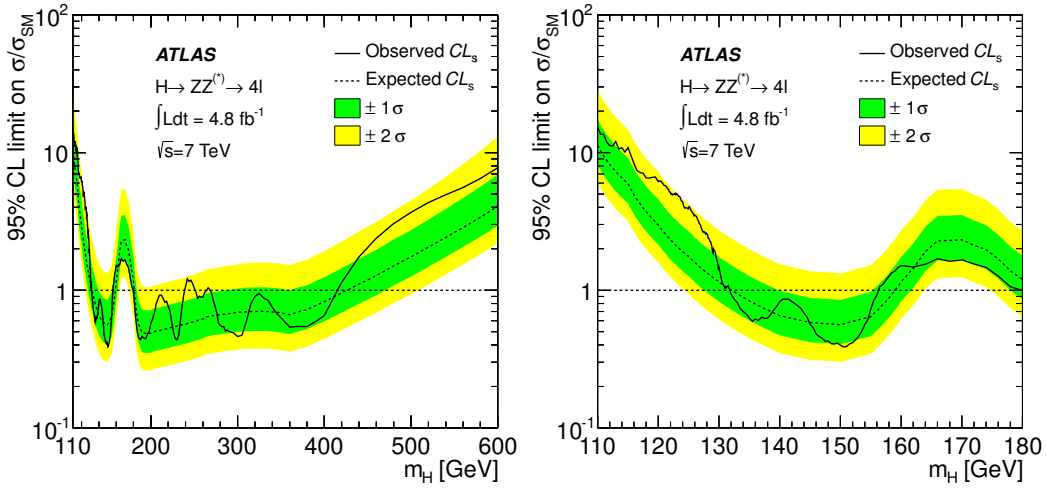

Figure 8.3 95% CL upper limits on the Standard Model Higgs boson production cross section as a function of m_H, for the analysis of 2011 data at $\sqrt{s}$ = 7 TeV. The dashed line represents the expected upper limit while the full line represents the observed one. The green and yellow (dark and light) bands show the expected limit $\pm 1\sigma$ and $\pm 2\sigma$. In (a) is shown the full mass range and in (b) the low mass range.

the observed data (this probability is usually indicated, and we will follow this convention, with the name p_0). In this case no theoretical input is thus used on the Higgs boson, since we want to probe the compatibility of the observed data with the background-only hypothesis. The plots for this test are shown in Figure 8.6 and in Figure 8.7. In Figure 8.6 we show the result for 2011 and 2012 data separately and combined, in two different mass ranges: the filled lines correspond to the observed p_0 while the dashed lines represent the expected p_0. From Figure 8.6b we can clearly see that the excess is seen in both 2011 and 2012 data around m_H = 125 GeV and the analysis of the complete dataset gives us a local p_0 minimum value of 0.029%, which corresponds to 3.4 standard deviations. If we calculate the probability that this excess occurs anywhere in the mass range not yet excluded by LHC experiments[1],110-141 GeV, we obtain a global p_0 of 0.65% (2.5 standard deviations) at m_H = 125 GeV. We also tested the stability of this result by removing the Z mass constraint (see

[1] this calculation is usually referred to as "Look Elsewhere Effect" (LEE).

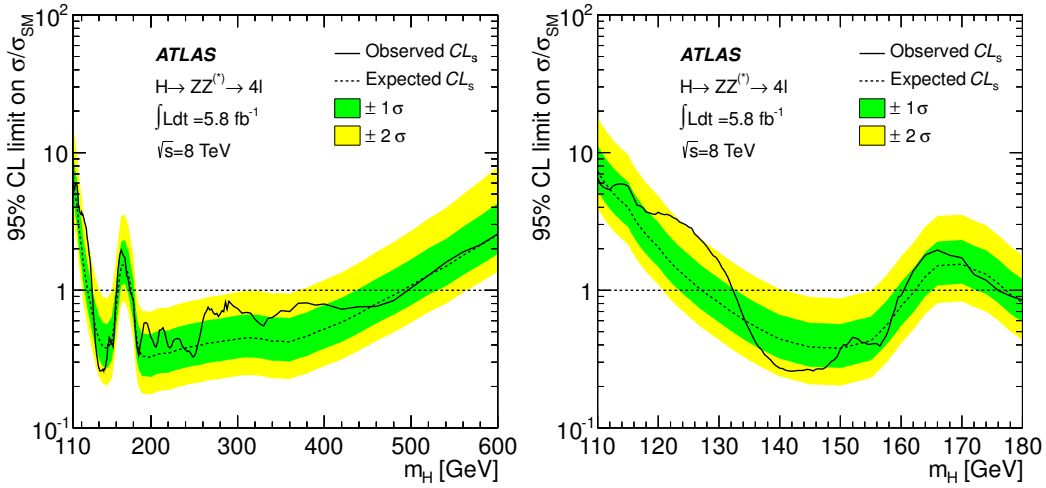

Figure 8.4 95% CL upper limits on the Standard Model Higgs boson production cross section as a function of m_H, for the analysis of 2012 data at $\sqrt{s}$ = 8 TeV. The dashed line represents the expected upper limit while the full line represents the observed one. The green and yellow (dark and light) bands show the expected limit $\pm 1\sigma$ and $\pm 2\sigma$. In (a) is shown the full mass range and in (b) the low mass range.

Section 6.4) or by letting the $ZZ^{(*)}$ background normalization free in the final fit, but none of these changes affects the 3.4σ achieved by the $H \to ZZ^{(*)} \to 4\ell$ channel. This excess is thus well above the expectations for the background-only hypothesis and provides a first observation of a new resonance.

Finally, it is very interesting to look at the different sub-channels of the analysis and they are shown in Figure 8.7, separately for 2011 and 2012 data. It is evident that the excess is driven by the 4μ channel, since muons have higher detection efficiency and less background contamination with respect to electrons, as well as a better resolution on $m_{4\ell}$. All channels with electrons have a smaller impact on the final result, as we would have expected. The improvements in the electron identification for 2012 have made the expected curves for the 4μ and $2e2\mu$ channels a little bit closer and the same can be said for the $2\mu 2e$ and $4e$ curves.

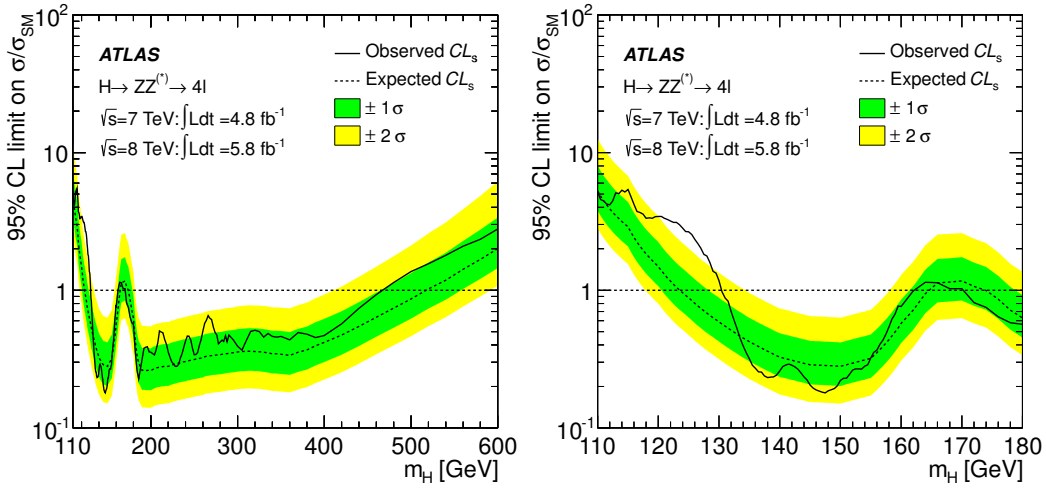

Figure 8.5 95% CL upper limits on the Standard Model Higgs boson production cross section as a function of m_H, for the analysis of the complete dataset. The dashed line represents the expected upper limit while the full line represents the observed one. The green and yellow (dark and light) bands show the expected limit $\pm 1\sigma$ and $\pm 2\sigma$. In (a) is shown the full mass range and in (b) the low mass range.

8.5 Signal strength

The 3.4σ significant excess seen by the $H \to ZZ^{(*)} \to 4\ell$ analysis can be further characterized by testing its compatibility with a first observation of the Standard Model Higgs boson. In order to accomplish this, we can define the strength of the signal observed in units of σ_{SM} as follows:

$$\mu = \frac{\sigma_{\mathrm{obs}}}{\sigma_{\mathrm{SM}}} \tag{8.6}$$

and, of course, σ_{SM} is taken from theoretical production cross section and branching ratio estimations. We expect this parameter μ to be one in case we are dealing with the observation of a Standard Model Higgs boson.

The signal strength is shown in Figure 8.8a as a function of m_H. In Figure 8.8b it is shown the same thing but injecting in our data sample a Higgs of $m_H = 125$ GeV. The best fit is represented by the black line while the approximate $\pm 1\sigma$ variations are shown by the colored bands and are evaluated using the interval $-2\ln\lambda(\mu) < 1$, where λ is the profile likelihood ratio test statistic.

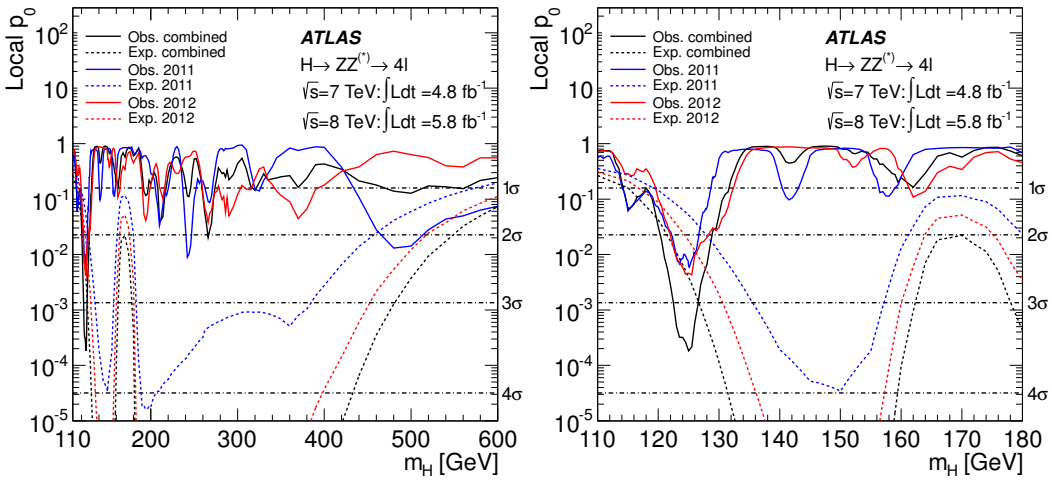

Figure 8.6 Local p_0 for the 2011 (blue) and 2012 (red) data, as well as for their combination (black). The full line represents the observed local p_0 while the dashed curve shows the expected median local p_0, tested for each m_H. The horizontal dotted lines indicate the p_0 values corresponding to 1σ, 2σ, 3σ and 4σ.

Finally, in Figure 8.9 we can see the best fit values, as well as their likelihood ratio contours for 68% CL and 95% CL, in the (μ, m_H) plane. The best fit is represented by the small cross and yields $\mu = 1.4 \pm 0.6$ and $m_H \sim 125$ GeV. These plots prove that the excess of events seen in data by the $H \to ZZ^{(*)} \to 4\ell$ analysis is, within errors, compatible with the presence of a Standard Model Higgs boson.

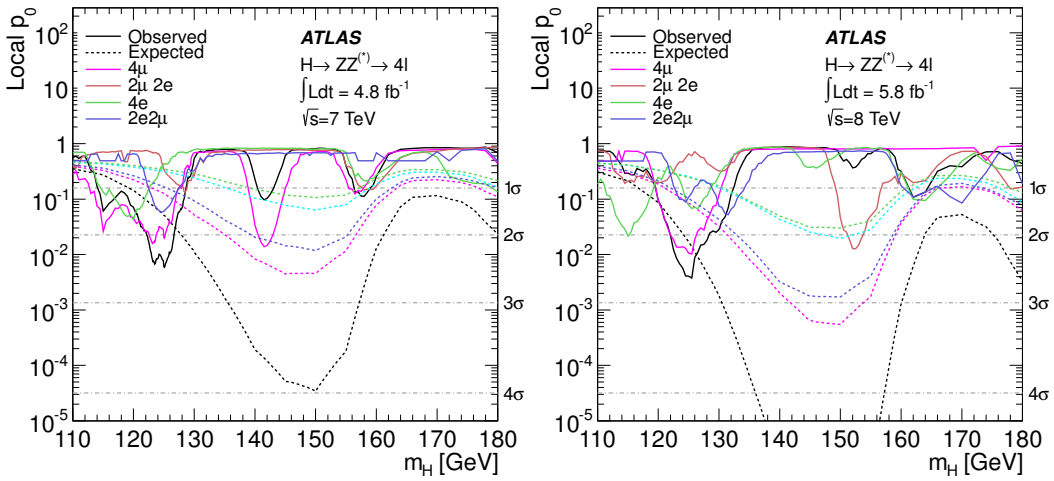

(a) **(b)**

Figure 8.7 Local p_0 for the 4μ, $2\mu 2e$, $4e$ and $2e2\mu$ channels separately, for the 2011 dataset (a) and for the 2012 dataset (b). The full line represents the observed local p_0 while the dashed curve shows the expected median local p_0, tested for each m_H. The horizontal dotted lines indicate the p_0 values corresponding to 1σ, 2σ, 3σ and 4σ.

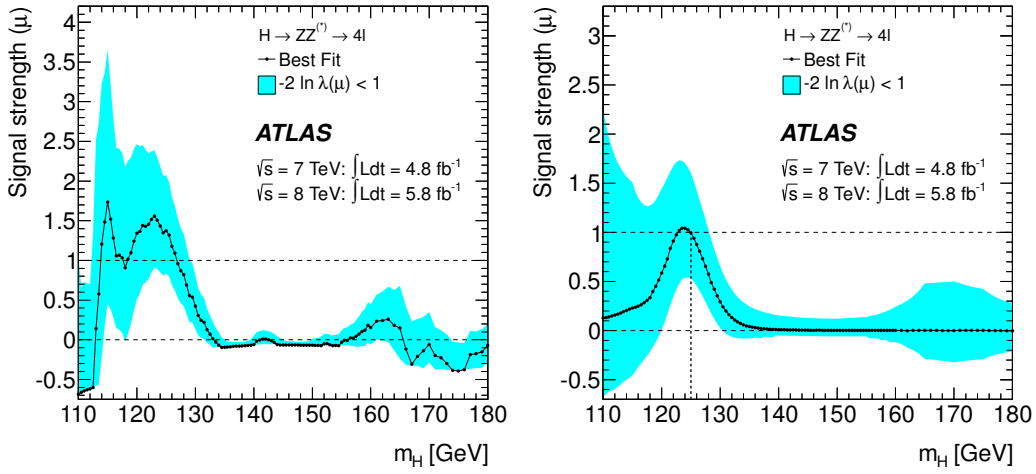

(a) **(b)**

Figure 8.8 The signal strength parameter $\mu = \frac{\sigma_{\rm obs}}{\sigma_{\rm SM}}$. obtained from a fit of the 2011 and 2012 data samples (a) and from the injection of a Standard Model Higgs boson signal with m_H = 125 GeV.

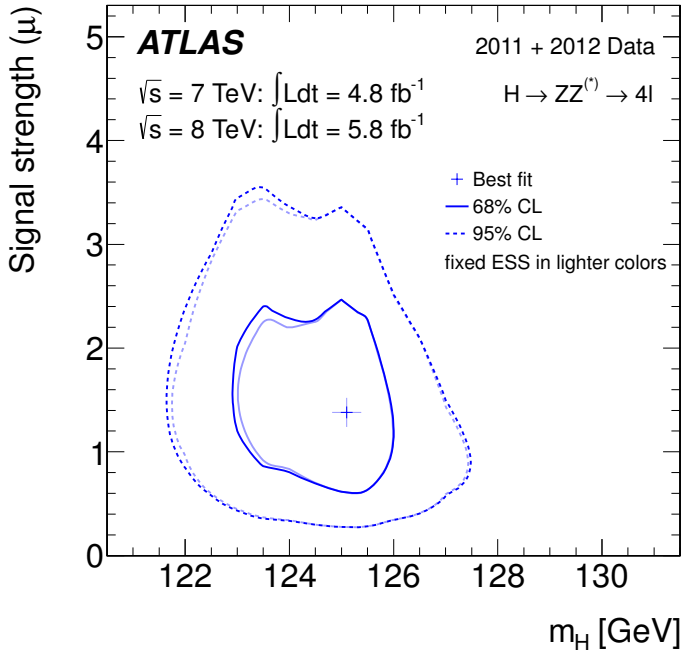

Figure 8.9 Best fit values for μ and m_H, and likelihood ratio contours that, in the asymptotic limit, correspond to 68% and 95% level contours in the (μ, m_H) plane. The light lines indicate the effect of holding constant at their best-fit values the nuisance parameters which describe the energy scale systematic uncertainties in the likelihood function.

Chapter 9

Combination of all ATLAS Higgs searches

The $H \to ZZ^{(*)} \to 4\ell$ channel is, as already explained in Chapter 1, not the only channel which can show the evidence of a Higgs boson. In this Chapter we will give the results of the combination of all ATLAS results in terms of Higgs searches [89].

For the following results the $H \to ZZ^{(*)} \to 4\ell$ analysis presented in this thesis has been used, together with the $H \to ZZ^{(*)} \to \ell\ell qq$, $H \to ZZ^{(*)} \to \ell\ell\nu\nu$, $H \to \gamma\gamma$, $H \to WW^{(*)}$, $VH \to Vb\bar{b}$ and $H \to \tau^+\tau^-$ channels. All these analyses have been performed on 2011 data while only the $H \to ZZ^{(*)} \to 4\ell$, $H \to WW^{(*)} \to e\nu\mu\nu$ and $H \to \gamma\gamma$ channels have also been updated to the luminosity collected until mid-June 2012, being these ones the less sensitive to pile-up effects and also the most promising.

The combination of all decay channels is based on the global signal strength, μ, and on the nuisance[1] parameters that correspond to the correlated sources of systematic uncertainty:

Integrated luminosity

The uncertainty on the integrated luminosity has been considered fully

[1] With the term "nuisance parameter" we indicate all those parameters which are not of immediate interest in the statistical analysis of our data, but must be accounted for. Systematic uncertainties, not being interesting parameters of the fit, are thus usually considered nuisance parameters.

Table 9.1 Summary of the individual channels used in the combination.

Higgs Boson Decay Channel	2011 data at $\sqrt{s}$ = 7 TeV $\int \mathscr{L} dt$ [fb^{-1}]	2012 data at $\sqrt{s}$ = 8 TeV $\int \mathscr{L} dt$ [fb^{-1}]	Ref.
$H \to ZZ^{(*)} \to 4\ell$	4.8	5.8	[90]
$H \to ZZ^{(*)} \to \ell\ell\nu\nu$	4.7	—	[91]
$H \to ZZ^{(*)} \to \ell\ell qq$	4.7	—	[92]
$H \to \gamma\gamma$	4.8	5.9	[93]
$H \to WW^{(*)} \to \ell\nu\ell\nu$	4.7	—	[94]
$H \to WW^{(*)} \to \ell\nu qq'$	4.7	—	[95]
$H \to WW^{(*)} \to e\nu\mu\nu$	—	5.8	[96]
$H \to \tau_{lep}\tau_{lep}$	4.7	—	[97]
$H \to \tau_{lep}\tau_{had}$	4.7	—	
$H \to \tau_{had}\tau_{had}$	4.7	—	
$ZH \to Zb\bar{b}\,(Z \to \nu\nu)$	4.6	—	[98]
$WH \to Wb\bar{b}\,(W \to \ell\nu)$	4.7	—	
$ZH \to Zb\bar{b}\,(Z \to \ell\ell)$	4.7	—	

correlated among the channels. The uncertainty assigned is ±3.9% for the 2011 data at $\sqrt{s}$ = 7 TeV and ±3.6% for the 2012 data at $\sqrt{s}$ = 8 TeV. Since the $H \to ZZ^{(*)} \to 4\ell$ and $H \to \gamma\gamma$ analyses on 2011 data have been re-made with optimized techniques, the uncertainty in these cases has been taken as ±1.8%.

Trigger efficiencies for photons and electrons

The trigger identification efficiencies of electrons and photons have been considered to be fully correlated and treated as such.

Energy scale for electrons and photons

The energy scale of electrons and photons has been modeled using a set of parameters that takes into account the pre-sampler energy scale, the material description in front of the calorimeters and the method used for the calibration of the EM calorimeter.

Muon reconstruction

In order to cope with the different types of muons used by the channels

taken into account, as well as the different p_T ranges, the systematic uncertainties related to the muon reconstruction have been separated in those concerning the Inner Detector measurement and those regarding the Muon Spectrometer measurement.

Jet energy scale and resolution

The uncertainties related to the jet energy scale and the jet energy resolution have a dependence on p_T and η, as well as on the flavor of the jet taken into account. In order to simplify this situation, independent nuisance parameters for jet energy scale and jet energy resolution are associated to processes with different kinematic selections.

Theoretical uncertainties

Uncertainties from theory affect mostly the predictions on the signal expectations. The QCD scale uncertainty, for m_H = 125 GeV, yields an uncertainty of $^{+7\%}_{-8\%}$ for the gluon-gluon fusion, ±1% for the vector boson fusion and associated production with a W or a Z and $^{+4\%}_{-9\%}$ for the production associated with a $t\bar{t}$ pair. The uncertainty on the predicted branching ratios is taken to be ±5% and the parton distribution functions give a ±8% uncertainty for gluon-gluon fusion and associated production with $t\bar{t}$, while ±4% for vector boson fusion and associated production with W/Z.

The limits on the production of the Standard Model Higgs boson are expressed in terms of the signal strength, μ. The combination gives an expected 95% CL exclusion range from 110 GeV to 582 GeV, while the observed exclusion range is 111-122 GeV and 131-559 GeV. This result is shown in Figure 9.1.

The significance of the excess around m_H = 126 GeV, on the other hand, is shown in the observed local p_0 plots, in Figure 9.1 and in Figure 9.3 for the combination of all the channels and in Figure 9.2 separately for $H\to ZZ^{(*)}\to 4\ell$, $H\to\gamma\gamma$ and $H\to WW^{(*)}\to\ell\nu\ell\nu$. This significance amounts to 6.0σ and becomes 5.9σ if we include the energy scale uncertainty for photons and electrons. The global significance of a local 5.9σ excess anywhere in the mass range 110-600 GeV is estimated to be approximately 5.1σ.

More information can be extracted from the observed excess by quantifying the strength of the signal observed in units of the theoretical cross section

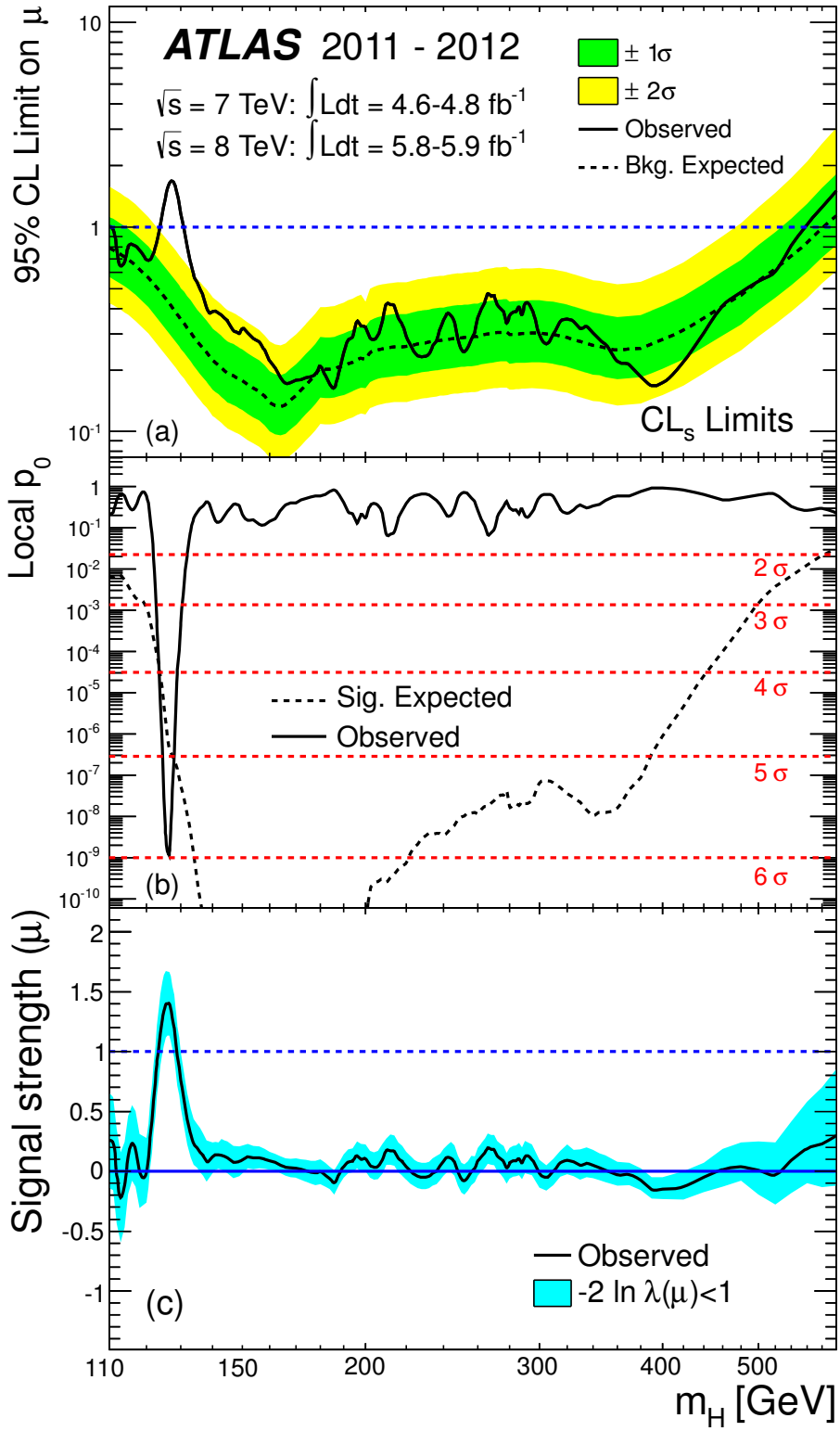

Figure 9.1 Results of the combination of the channels reported in Table 9.1. The observed (solid) 95% CL limits on the signal strength as a function of m_H and the expectation (dashed) under the background-only hypothesis are shown in (a). The observed local p0 is shown in (b) instead, as a function of m_H. The expected value for a Standard Model Higgs boson signal hypothesis is given by the dashed line. The signal strength $\hat{\mu}$ that yields the best fit is shown, as a function of m_H, in (c).

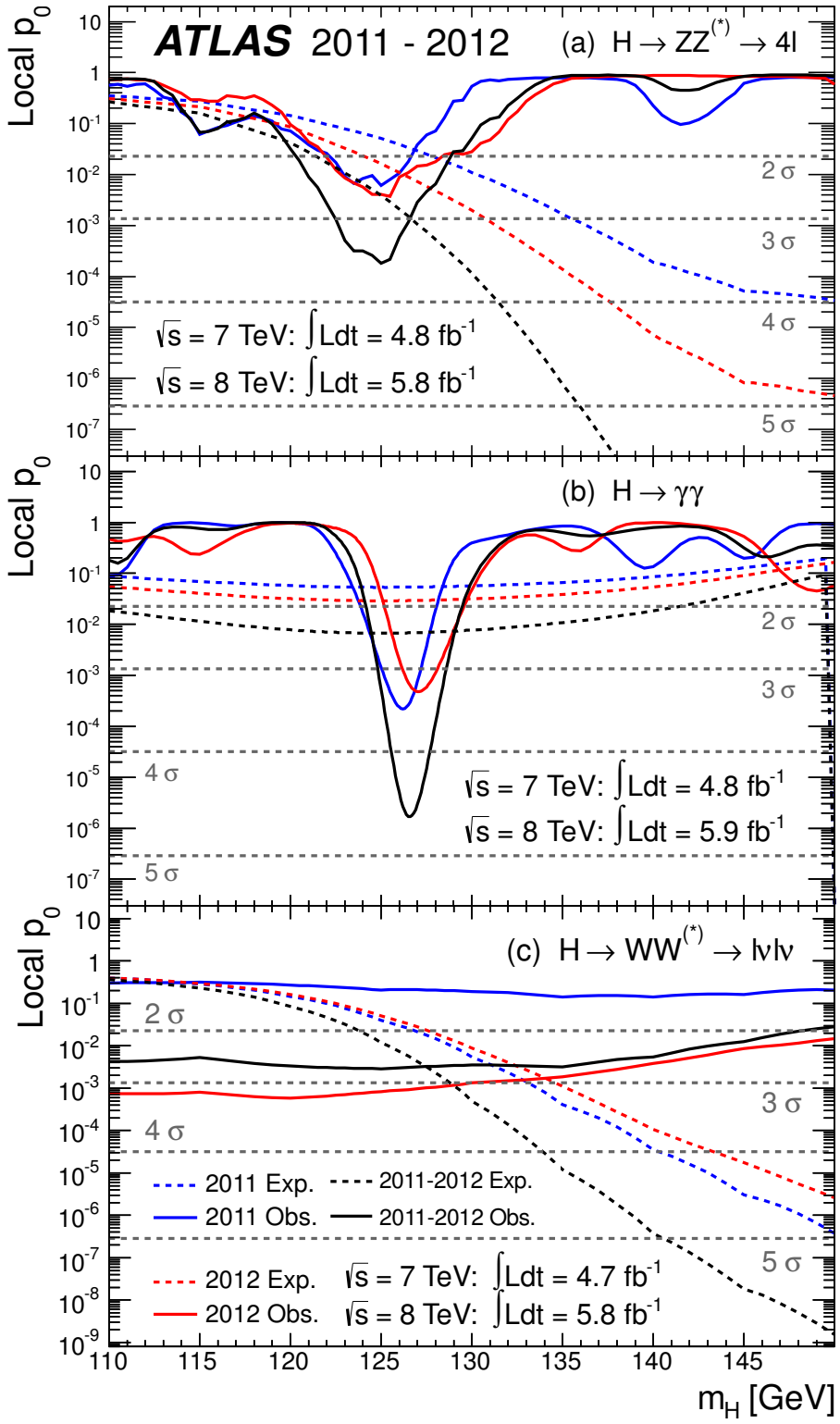

Figure 9.2 The solid line shows the observed local p_0 as a function of the hypothetical Higgs mass m_H for the three most sensitive channels used in the combination, (a) $H \to ZZ^{(*)} \to 4\ell$, (b) $H \to \gamma\gamma$ and (c) $H \to WW^{(*)} \to \ell\nu\ell\nu$, while the dashed line shows the expected p_0. In blue are shown the results of the analysis of 2011 data, in red those of 2012 data and in black the combination of the two datasets.

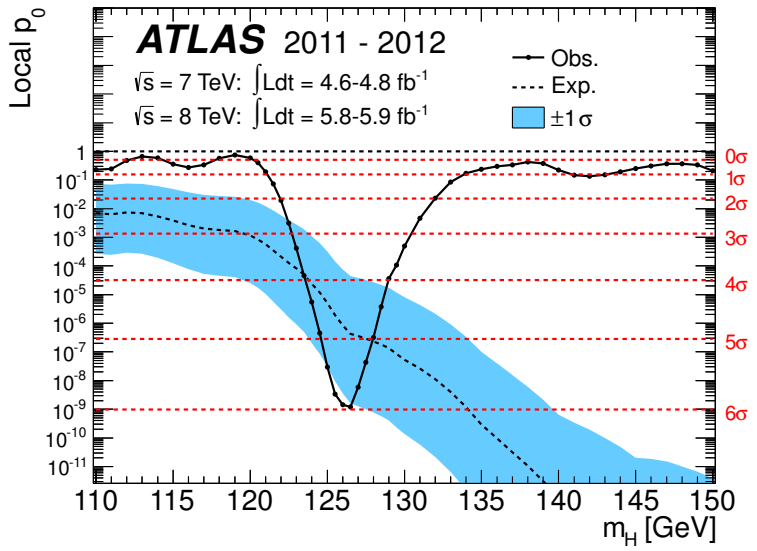

Figure 9.3 Local p_0 as a function of m_H, for the combination of the channels listed in Table 9.1. The solid line represents the observed p_0 while the dashed line shows the expected local p_0 for a Higgs boson at a specific mass. This plot shows clearly the significance obtained by the combination of all channels in ATLAS, which corresponds to 5.9σ.

σ_{SM}, as already explained in Section 8.5. The combined signal strength as a function of the hypothetical Higgs mass, m_H, is shown in Figure 9.1; the best fit value is obtained at $m_H = 126$ GeV and $\mu = 1.4 \pm 0.3$ and it is consistent with the Standard Model Higgs boson hypothesis ($\mu = 1$). The confidence intervals in the (μ, m_H) plane for the $H \to ZZ^{(*)} \to 4\ell$, $H \to \gamma\gamma$ and $H \to WW^{(*)} \to \ell\nu\ell\nu$ channels are shown, instead, in Figure 9.4. The best fits for each of these channels are indicated with the small crosses (the ones from the $H \to ZZ^{(*)} \to 4\ell$ analysis and the $H \to WW^{(*)} \to \ell\nu\ell\nu$ analysis are overlapping), the solid lines show the confidence intervals corresponding to 68% CL and the dashed ones to 95% CL. We can notice that the $H \to ZZ^{(*)} \to 4\ell$ and $H \to \gamma\gamma$ channels have a better resolution on m_H, compared to $H \to WW^{(*)} \to \ell\nu\ell\nu$. The shape of the contours for the $H \to WW^{(*)} \to \ell\nu\ell\nu$ analysis is a direct consequence of the low resolution on m_H of the channel and of the steep decrease of the theoretical cross section.

Finally, in Figure 9.5 are shown the different signal strengths observed by different channels; we can see that the $VH \to Vb\bar{b}$ and $H \to \tau^+\tau^-$ channels have very large uncertainties and slightly contribute to the combination, while the highest signal strength observed is the one obtained by the $H \to \gamma\gamma$ channel, which is $\mu \sim 1.8$.

The combination of all ATLAS results allowed to claim the discovery of a new particle, with a mass of $126.0 \pm 0.4(\text{stat.}) \pm 0.4(\text{syst.})$ GeV. This historical result still has to be completed, by fully understanding the nature of the newly found particle. First conclusions can be drawn on the basis of the observed decays:

Neutral From the observation of decays such as $H \to ZZ^{(*)} \to 4\ell$, $H \to \gamma\gamma$ and $H \to WW^{(*)} \to \ell\nu\ell\nu$, we can derive that this new particle is neutral.

Boson In order to decay into pairs of vector bosons, this particle must have integer spin.

Spin$\neq$ 1 Following Landau-Yang theorem [99, 100], a massive particle of spin equal to one cannot decay into a pair of photons (since this would violate angular momentum conservation laws). Having observed this particle in the $H \to \gamma\gamma$ channel, the spin 1 hypothesis is highly disfavoured.

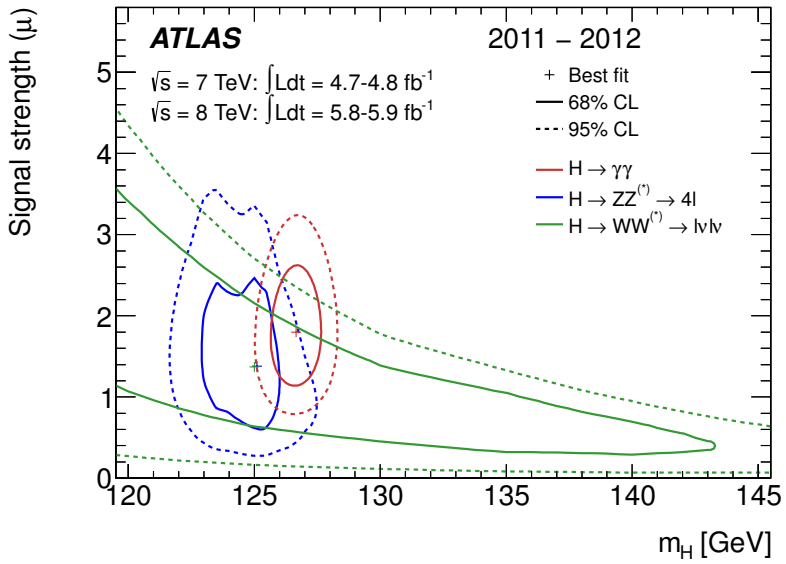

Figure 9.4 Confidence intervals in the (μ, m_H) plane for the three most sensitive channels, $H \to ZZ^{(*)} \to 4\ell$, $H \to \gamma\gamma$ and $H \to WW^{(*)} \to \ell\nu\ell\nu$. The values which give the best fit are indicated by the markers (those of $H \to ZZ^{(*)} \to 4\ell$ and $H \to WW^{(*)} \to \ell\nu\ell\nu$ coincide).

More data are needed to fully test the compatibility of this new resonance with the long-sought Higgs boson. Couplings to fermions have yet to be observed by the $VH \to Vb\bar{b}$ and $H \to \tau^+\tau^-$ channels and the spin-parity properties of the particle have also to be tested.

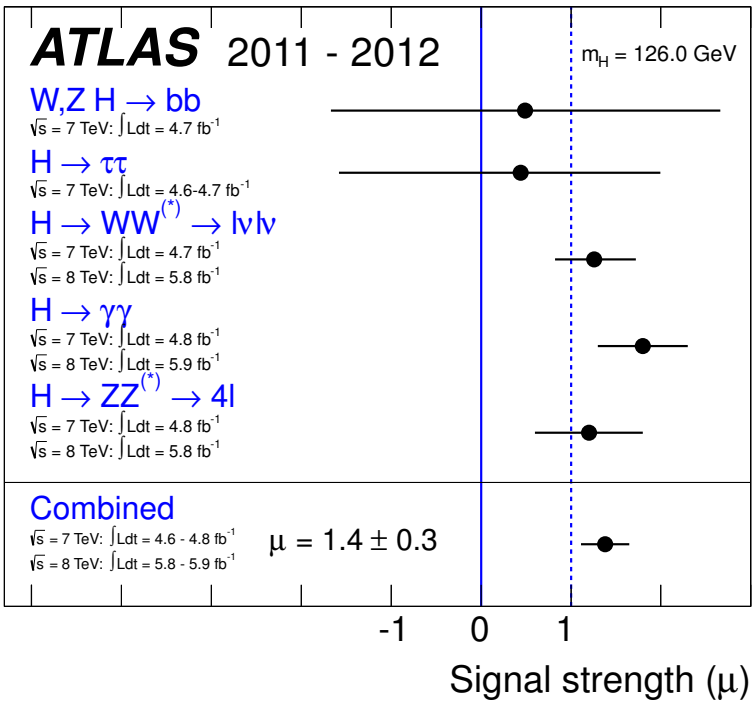

Figure 9.5 Comparison of the signal strengths observed in all the channels used in the combination, with m_H = 126 GeV.

Conclusions

The Standard Model of particle physics has proven to provide a good description for many phenomena of the subatomic interactions in these last twenty years. Many tests made at colliders such as LEP or Tevatron have certified this but were not able to come up with any conclusive statement on the only missing piece of the Standard Model, the Higgs boson. The introduction of such a particle in the Standard Model is fundamental to ensure that the theory is consistent with current observation. The weak vector bosons, $W^{\pm}$ and Z, acquire mass through the Higgs boson and also the masses of the fermions can be introduced through Yukawa couplings with this particle.

Among the many decay channels of the Higgs, the $H \to ZZ^{(*)} \to 4\ell$ is one of the best final states we can exploit at a hadron collider such as the LHC to search for the Higgs boson on a very wide mass range, from 110 to 600 GeV. The analysis of the decay $H \to ZZ^{(*)} \to 4\ell$ provides a very clean signature for the Higgs boson, exploiting the four leptons (electrons or muons) of the final state. One crucial aspect of this analysis is thus represented by the capability of the experiment of identifying leptons with good efficiency while rejecting fake leptons.

The first part of this thesis has thus been dedicated to the electron reconstruction and identification improvements. The electron reconstruction has been refined by introducing a Gaussian Sum Filter algorithm which can correctly account for the energy lost by electrons along their path inside the ATLAS detector via bremsstrahlung. The introduction of GSF electrons itself has increased our acceptance of ~20%. This new reconstruction algorithm and the harsh data taking conditions of 2012 required a new, dedicated identification menu. For this purpose, the *MultiLepton* menu has been developed and it ensures higher efficiency on electrons and, at the same time, higher rejection

on fakes with respect to the standard identification menu used in ATLAS. This *MultiLepton* menu has also the property of being very robust against pile-up, thus guaranteeing homogenous performance over the whole 2012 dataset.

In the central part of the thesis we presented a search for the Higgs boson in the $H \to ZZ^{(*)} \to 4\ell$ channel, using 4.8 fb^{-1} of 2011 data at $\sqrt{s}$ = 7 TeV and 5.8 fb^{-1} of 2012 data at $\sqrt{s}$ = 8 TeV. Particular emphasis has been given to the determination of data/Monte Carlo scale factors for the analysis selections on electrons and on the backgrounds of the $H \to ZZ^{(*)} \to 2\mu 2e$ and $H \to ZZ^{(*)} \to 4e$ channels. Together with the standard method of categorizing the sub-leading pairs, we also introduced the estimation using same-sign events and we also developed a completely new control region, built by requiring three of the four leptons to pass the analysis requirements while relaxing these same requirements on only one electron. This new control region allows for another estimation of the reducible background for electrons, by performing a multi-dimensional fit on sensitive variables which can distinguish between electrons, conversions and fakes.

We presented also the results of the $H \to ZZ^{(*)} \to 4\ell$ analysis, which observes an excess of events at 125 GeV compatible with a Standard Model Higgs boson, with a local significance corresponding to 3.4σ. The observed rate of events is compatible with the assumption of a Standard Model Higgs boson, being $\mu = \frac{\sigma_{\text{obs}}}{\sigma_{\text{SM}}} = 1.4 \pm 0.6$.

This result is corroborated by the combination of the $H \to ZZ^{(*)} \to 4\ell$ analysis with all the other Higgs searches performed by ATLAS, especially using the $H \to \gamma\gamma$ and $H \to WW^{(*)} \to \ell\nu\ell\nu$ channels. The ATLAS combined result translates in a significance of 5.9σ for the excess seen at $126.0 \pm 0.4(\text{stat.}) \pm 0.4(\text{syst.})$ GeV. The compatibility of this result with the Standard Model Higgs boson hypothesis is given by $\mu = 1.4 \pm 0.3$.

Bibliography

[1] D. J. Gross and F. Wilczek, *Asymptotically Free Gauge Theories. I*, Phys. Rev. D **8** (Nov, 1973) 3633–3652.

[2] H. D. Politzer, *Reliable Perturbative Results for Strong Interactions?*, Phys. Rev. Lett. **30** (Jun, 1973) 1346–1349.

[3] D. J. Gross and F. Wilczek, *Asymptotically Free Gauge Theories. II*, Phys. Rev. D **9** (Feb, 1974) 980–993.

[4] H. D. Politzer, *Asymptotic freedom: An approach to strong interactions*, Physics Reports **14** (1974) no. 4, 129 – 180.

[5] E. Fermi, *Tentativo di una Teoria Dei Raggi β*, Il Nuovo Cimento (1924-1942) **11** (1934) 1–19.

[6] S. L. Glashow, *Partial-symmetries of weak interactions*, Nuclear Physics **22** (1961) no. 4, 579–588.

[7] S. Weinberg, *A Model of Leptons*, Phys. Rev. Lett. **19** (Nov, 1967) 1264–1266.

[8] A. Salam and J. Ward, *Weak and electromagnetic interactions*, Il Nuovo Cimento (1955-1965) **11** (1959) 568–577.

[9] F. Englert and R. Brout, *Broken Symmetry and the Mass of Gauge Vector Mesons*, Phys. Rev. Lett. **13** (Aug, 1964) 321–323.

[10] P. W. Higgs, *Broken Symmetries and the Masses of Gauge Bosons*, Phys. Rev. Lett. **13** (Oct, 1964) 508–509.

[11] G. S. Guralnik, C. R. Hagen, and T. W. B. Kibble, *Global Conservation Laws and Massless Particles*, Phys. Rev. Lett. **13** (Nov, 1964) 585–587.

[12] N. Cabibbo, L. Maiani, G. Parisi, and R. Petronzio, *Bounds on the fermions and Higgs boson masses in grand unified theories*, Nuclear Physics B **158** (1979) no. 2–3, 295–305.

[13] J. Ellis, J. Espinosa, G. Giudice, A. Hoecker, and A. Riotto, *The probable fate of the Standard Model*, Physics Letters B **679** (2009) no. 4, 369 – 375.

[14] M. Baak, M. Goebel, J. Haller, A. Hoecker, D. Ludwig, et al., *Updated Status of the Global Electroweak Fit and Constraints on New Physics*, Eur.Phys.J. **C72** (2012) 2003, arXiv:1107.0975 [hep-ph].

[15] LEP Working Group for Higgs boson searches, ALEPH Collaboration, DELPHI Collaboration, L3 Collaboration, OPAL Collaboration Collaboration, R. Barate et al., *Search for the standard model Higgs boson at LEP*, Phys.Lett. **B565** (2003) 61–75, arXiv:hep-ex/0306033 [hep-ex].

[16] TEVNPH (Tevatron New Phenomina and Higgs Working Group), CDF Collaboration, D0 Collaboration Collaboration, *Combined CDF and D0 Search for Standard Model Higgs Boson Production with up to 10.0 fb^{-1} of Data*, arXiv:1203.3774 [hep-ex].

[17] ATLAS Collaboration, *Combined search for the Standard Model Higgs boson using up to* 4.9 fb^{-1} *of pp collision data at* $\sqrt{s} = 7$ TeV *with the ATLAS detector at the LHC*, Phys. Lett. **B710** (2012) 49–66, arXiv:1202.1408 [hep-ex].

[18] CMS Collaboration, *Combined results of searches for the standard model Higgs boson in pp collisions at* $\sqrt{s} = 7$ *TeV*, Phys. Lett. **B710** (2012) 26–48, arXiv:1202.1488 [hep-ex].

[19] LHC Higgs Cross Section Working Group, S. Dittmaier, C. Mariotti, G. Passarino, and R. Tanaka (Eds.), *Handbook of LHC Higgs cross*

sections: 1. Inclusive observables, 2011. arXiv:1101.0593 [hep-ph]. CERN-2011-002.

[20] LHC Higgs Cross Section Working Group, S. Dittmaier, C. Mariotti, G. Passarino, and R. Tanaka (Eds.), *Handbook of LHC Higgs Cross Sections: 2. Differential distributions*, 2012. arXiv:1201.3084 [hep-ph].

[21] F. Mandl and G. Shaw, *Quantum Field Theory*. A Wiley-Interscience publication. John Wiley & Sons, 2010.

[22] O. S. Brüning, P. Collier, P. Lebrun, S. Myers, R. Ostojic, J. Poole, and P. Proudlock, *LHC Design Report*. CERN, Geneva, 2004.

[23] O. S. Brüning, P. Collier, P. Lebrun, S. Myers, R. Ostojic, J. Poole, and P. Proudlock, *LHC Design Report*. CERN, Geneva, 2004.

[24] M. Benedikt, P. Collier, V. Mertens, J. Poole, and K. Schindl, *LHC Design Report*. CERN, Geneva, 2004.

[25] S. Myers and E. Picasso, *The design, construction and commissioning of the CERN Large Electron-Positron collider*, Contemporary Physics **31** (1990) no. 6, 387–403.

[26] CERN Courier, *Incident in sector 3-4 of the LHC*, 2008. November Issue (2008) .

[27] ATLAS Collaboration, *Luminosity Determination in pp Collisions at $\sqrt{s} = 7$ TeV Using the ATLAS Detector at the LHC*, Eur. Phys. J. **C 71** (2011) 1630, arXiv:1101.2185 [hep-ex].

[28] ATLAS Collaboration, *Luminosity Determination in pp Collisions at $\sqrt{s} = 7$ TeV using the ATLAS Detector in 2011*, .

[29] ATLAS Collaboration, *The ATLAS Experiment at the CERN Large Hadron Collider*, JINST **3** (2008) S08003.

[30] ATLAS Collaboration, *ATLAS detector and physics performance: Technical Design Report, 1*. Technical Design Report ATLAS. CERN, Geneva, 1999.

[31] ATLAS Collaboration, *ATLAS detector and physics performance: Technical Design Report, 2.* Technical Design Report ATLAS. CERN, Geneva, 1999.

[32] ATLAS Collaboration, *ATLAS magnet system: Technical Design Report, 1.* Technical Design Report ATLAS. CERN, Geneva, 1997.

[33] ATLAS Collaboration, *ATLAS central solenoid: Technical Design Report.* Technical Design Report ATLAS. CERN, Geneva, 1997.

[34] ATLAS Collaboration, *ATLAS barrel toroid: Technical Design Report.* Technical Design Report ATLAS. CERN, Geneva, 1997.

[35] ATLAS Collaboration, *ATLAS end-cap toroids: Technical Design Report.* Technical Design Report ATLAS. CERN, Geneva, 1997.

[36] ATLAS Collaboration, *ATLAS inner detector: Technical Design Report, 1.* Technical Design Report ATLAS. CERN, Geneva, 1997.

[37] ATLAS Collaboration, *ATLAS inner detector: Technical Design Report, 2.* Technical Design Report ATLAS. CERN, Geneva, 1997.

[38] ATLAS Collaboration, *The ATLAS Inner Detector commissioning and calibration*, Eur. Phys. J. C **70** (Jun, 2010) 787–821. 34 p.

[39] ATLAS Collaboration, *ATLAS pixel detector: Technical Design Report.* Technical Design Report ATLAS. CERN, Geneva, 1998.

[40] ATLAS Collaboration, *Calibration of the ATLAS Transition Radiation Tracker*, Tech. Rep. ATLAS-CONF-2011-006, CERN, Geneva, Feb, 2011.

[41] ATLAS Collaboration, *ATLAS calorimeter performance: Technical Design Report.* Technical Design Report ATLAS. CERN, Geneva, 1996.

[42] ATLAS Collaboration, *ATLAS liquid-argon calorimeter: Technical Design Report.* Technical Design Report ATLAS. CERN, Geneva, 1996.

[43] ATLAS Collaboration, *Drift Time Measurement in the ATLAS Liquid Argon Electromagnetic Calorimeter using Cosmic Muons*, Eur. Phys. J. C **70** (Jul, 2010) 755–785. 30 p.

[44] ATLAS Collaboration, *Readiness of the ATLAS Liquid Argon Calorimeter for LHC Collisions*, Eur. Phys. J. C **70** (May, 2010) 723–753. 31 p.

[45] ATLAS Collaboration, *ATLAS tile calorimeter: Technical Design Report*. Technical Design Report ATLAS. CERN, Geneva, 1996.

[46] ATLAS Collaboration, *Readiness of the ATLAS Tile Calorimeter for LHC collisions*, Eur. Phys. J. C **70** (Jul, 2010) 1193–1236. 64 p.

[47] ATLAS Collaboration, *ATLAS muon spectrometer: Technical Design Report*. Technical Design Report ATLAS. CERN, Geneva, 1997.

[48] ATLAS Collaboration, *Muon Momentum Resolution in First Pass Reconstruction of pp Collision Data Recorded by ATLAS in 2010*, Tech. Rep. ATLAS-CONF-2011-046, CERN, Geneva, Mar, 2011.

[49] ATLAS Collaboration, *ATLAS level-1 trigger: Technical Design Report*. Technical Design Report ATLAS. CERN, Geneva, 1998.

[50] ATLAS Collaboration, *ATLAS high-level trigger, data-acquisition and controls:Technical Design Report*. Technical Design Report ATLAS. CERN, Geneva, 2003.

[51] ATLAS Collaboration, *Atlas Computing: technical design report*. CERN, Geneva, 2005.

[52] ATLAS Collaboration, *The ATLAS Simulation Infrastructure*, Eur. Phys. J. C **70** (May, 2010) 823–874. 53 p.

[53] C. Eck et al., *LHC computing Grid: Technical Design Report. Version 1.06 (20 Jun 2005)*. Technical Design Report LCG. CERN, Geneva, 2005.

[54] ATLAS Collaboration, *Electron performance measurements with the ATLAS detector using the 2010 LHC proton-proton collision data*, Eur. Phys. J. C **72** (Oct, 2011) 1909. 45 p.

[55] W. Lampl, S. Laplace, D. Lelas, P. Loch, H. Ma, S. Menke, S. Rajagopalan, D. Rousseau, S. Snyder, and G. Unal, *Calorimeter Clustering Algorithms: Description and Performance*, Tech. Rep. ATL-LARG-PUB-2008-002. ATL-COM-LARG-2008-003, CERN, Geneva, Apr, 2008.

[56] J. Beringer et al., *Review of Particle Physics, 2012-2013. Review of Particle Properties*, Phys. Rev. D **86** (2012) no. 1, 010001.

[57] H. Bethe and W. Heitler, *On the Stopping of Fast Particles and on the Creation of Positive Electrons*, Proceedings of the Royal Society of London. Series A, Containing Papers of a Mathematical and Physical Character **146** (1934) no. 856, pp. 83–112.

[58] L. D. Landau and I. Y. Pomeranchuk Dokl. Akad. Nauk SSSR **92:535** (1953) 735.

[59] A. Migdal Phys. Rev. **103** (1956) 1181.

[60] M. Ter-Mikaelian, *High-energy electromagnetic processes in condensed media*. Interscience tracts on physics and astronomy. Wiley-Interscience, 1972.

[61] S. Agostinelli et al., *GEANT4: A simulation toolkit*, Nucl. Instrum. Meth. **A 506** (2003) 250–303.

[62] R. Frühwirth, *Application of Kalman filtering to track and vertex fitting*, Nucl. Instrum. Methods Phys. Res., A **262** (Jun, 1987) 444. 19 p.

[63] R. Frühwirth, *A Gaussian-mixture approximation of the Bethe-Heitler model of electron energy loss by bremsstrahlung*, Computer Physics Communications **154** (2003) no. 2, 131–142.

[64] ATLAS Collaboration, *Improved electron reconstruction in ATLAS using the Gaussian Sum Filter-based model for bremsstrahlung*, Tech. Rep. ATLAS-CONF-2012-047, CERN, Geneva, May, 2012.

[65] T. Cornelissen, M. Elsing, S. Fleischmann, W. Liebig, E. Moyse, and A. Salzburger, *Concepts, Design and Implementation of the ATLAS New Tracking (NEWT)*, Tech. Rep. ATL-SOFT-PUB-2007-007. ATL-COM-SOFT-2007-002, CERN, Geneva, Mar, 2007.

[66] S. Alioli, P. Nason, C. Oleari, and E. Re, *NLO Higgs boson production via gluon fusion matched with shower in POWHEG*, JHEP **04** (2009) 002, arXiv:0812.0578 [hep-ph].

[67] P. Nason and C. Oleari, *NLO Higgs boson production via vector-boson fusion matched with shower in POWHEG*, JHEP **02** (2010) 037, arXiv:0911.5299 [hep-ph].

[68] T. Sjostrand, S. Mrenna, and P. Z. Skands, *PYTHIA 6.4 Physics and Manual*, JHEP **05** (2006) 026, arXiv:hep-ph/0603175.

[69] T. Sjostrand, S. Mrenna, and P. Z. Skands, *A Brief Introduction to PYTHIA 8.1*, Comput. Phys. Commun. **178** (2008) 852–867, arXiv:0710.3820 [hep-ph].

[70] P. Golonka and Z. Was, *PHOTOS Monte Carlo: A Precision tool for QED corrections in Z and W decays*, Eur. Phys. J. **C 45** (2006) 97–107, arXiv:hep-ph/0506026.

[71] N. Davidson, T. Przedzinski, and Z. Was, *PHOTOS Interface in C++: Technical and Physics Documentation*, arXiv:1011.0937 [hep-ph].

[72] A. Djouadi, M. Spira, and P. M. Zerwas, *Production of Higgs bosons in proton colliders: QCD corrections*, Phys. Lett. **B 264** (1991) 440–446.

[73] S. Dawson, *Radiative corrections to Higgs boson production*, Nucl. Phys. **B 359** (1991) 283–300.

[74] M. Spira, A. Djouadi, D. Graudenz, and P. M. Zerwas, *Higgs boson production at the LHC*, Nucl. Phys. **B 453** (1995) 17–82, arXiv:hep-ph/9504378.

[75] R. V. Harlander and W. B. Kilgore, *Next-to-next-to-leading order Higgs production at hadron colliders*, Phys. Rev. Lett. **88** (2002) 201801, arXiv:hep-ph/0201206.

[76] C. Anastasiou and K. Melnikov, *Higgs boson production at hadron colliders in NNLO QCD*, Nucl. Phys. **B 646** (2002) 220–256, arXiv:hep-ph/0207004.

[77] V. Ravindran, J. Smith, and W. L. van Neerven, *NNLO corrections to the total cross section for Higgs boson production in hadron hadron collisions*, Nucl. Phys. **B 665** (2003) 325–366, arXiv:hep-ph/0302135.

[78] S. Catani, D. de Florian, M. Grazzini, and P. Nason, *Soft-gluon resummation for Higgs boson production at hadron colliders*, JHEP **07** (2003) 028, arXiv:hep-ph/0306211.

[79] U. Aglietti, R. Bonciani, G. Degrassi, and A. Vicini, *Two-loop light fermion contribution to Higgs production and decays*, Phys. Lett. **B595** (2004) 432–441, arXiv:hep-ph/0404071.

[80] S. Actis, G. Passarino, C. Sturm, and S. Uccirati, *NLO Electroweak Corrections to Higgs Boson Production at Hadron Colliders*, Phys. Lett. **B670** (2008) 12–17, arXiv:0809.1301 [hep-ph].

[81] A. Djouadi, J. Kalinowski, and M. Spira, *HDECAY: A program for Higgs boson decays in the standard model and its supersymmetric extension*, Comput. Phys. Commun. **108** (1998) 56–74, arXiv:hep-ph/9704448.

[82] T. Melia, P. Nason, R. Rontsch, and G. Zanderighi, *W^+W^-, WZ and ZZ production in the POWHEG BOX*, JHEP **1111** (2011) 078, arXiv:1107.5051 [hep-ph].

[83] T. Binoth, N. Kauer, and P. Mertsch, *Gluon-induced QCD corrections to $pp \to ZZ \to \ell\bar{\ell}\ell'\bar{\ell}'$*, arXiv:0807.0024 [hep-ph].

[84] J. M. Campbell, R. K. Ellis, and C. Williams, *Vector boson pair production at the LHC*, JHEP **07** (2011) 018, arXiv:1105.0020 [hep-ph].

[85] S. Frixione, P. Nason, and B. R. Webber, *Matching NLO QCD and parton showers in heavy flavour production*, JHEP **08** (2003) 007, arXiv:hep-ph/0305252.

[86] M. Aliev et al., *HATHOR: HAdronic Top and Heavy quarks crOss section calculatoR*, Comput. Phys. Commun. **182** (2011) 1034, arXiv:1007.1327 [hep-ph].

[87] G. Corcella et al., *HERWIG 6: an event generator for hadron emission reactions with interfering gluons (including super-symmetric processes)* , JHEP **01** (2001) 010.

[88] J. M. Butterworth, J. R. Forshaw, and M. H. Seymour, *Multiparton interactions in photoproduction at HERA*, Z. Phys. **C 72** (1996) 637–646, arXiv:hep-ph/9601371.

[89] ATLAS Collaboration, G. Aad et al., *Observation of a new particle in the search for the Standard Model Higgs boson with the ATLAS detector at the LHC*, Phys.Lett. **B716** (2012) 1–29, arXiv:1207.7214 [hep-ex].

[90] ATLAS Collaboration, *Observation of an excess of events in the search for the Standard Model Higgs boson in the $H \to ZZ^{(*)} \to 4\ell$ channel with the ATLAS detector.*, Tech. Rep. ATLAS-CONF-2012-092, CERN, Geneva, Jul, 2012.

[91] ATLAS Collaboration Collaboration, G. Aad et al., *Search for a Standard Model Higgs boson in the $H \to ZZ \to l^+l^-\nu\bar{\nu}$ decay channel using 4.7 fb^{-1} of sqrt(s) = 7 TeV data with the ATLAS detector*, arXiv:1205.6744 [hep-ex].

[92] ATLAS Collaboration Collaboration, G. Aad et al., *Search for a Standard Model Higgs boson in the mass range 200-600 GeV in the $H \to ZZ \to \ell^+\ell^- q\bar{q}$ decay channel*, arXiv:1206.2443 [hep-ex].

[93] ATLAS Collaboration, *Observation of an excess of events in the search for the Standard Model Higgs boson in the gamma-gamma channel with the ATLAS detector*, Tech. Rep. ATLAS-CONF-2012-091, CERN, Geneva, Jul, 2012.

[94] ATLAS Collaboration, *Search for the Standard Model Higgs boson in the $H \to WW^{(*)} \to \ell\nu\ell\nu$ decay mode with 4.7fb^{-1} of ATLAS data at $\sqrt{7}$*, Physics Letters B **716** (2012) no. 1, 62 – 81.

[95] ATLAS Collaboration, G. Aad et al., *Search for the Higgs boson in the $H \to WW \to lnujj$ decay channel at sqrt(s) = 7 TeV with the ATLAS detector*, arXiv:1206.6074 [hep-ex].

[96] ATLAS Collaboration, *Observation of an Excess of Events in the Search for the Standard Model Higgs Boson in the $H \to WW^{(*)} \to \ell\nu\ell\nu$*

Channel with the ATLAS Detector, Tech. Rep. ATLAS-CONF-2012-098, CERN, Geneva, Jul, 2012.

[97] ATLAS Collaboration, G. Aad et al., *Search for the Standard Model Higgs boson in the H to $\tau^+\tau^-$ decay mode in $\sqrt{s} = 7$ TeV pp collisions with ATLAS*, JHEP **1209** (2012) 070, arXiv:1206.5971 [hep-ex].

[98] ATLAS Collaboration, G. Aad et al., *Search for the Standard Model Higgs boson produced in association with a vector boson and decaying to a b-quark pair with the ATLAS detector*, arXiv:1207.0210 [hep-ex].

[99] L. D. Landau Dokl. Akad. Nawk. USSR **60** (1948) 207.

[100] C. N. Yang, *Selection Rules for the Dematerialization of a Particle into Two Photons*, Phys. Rev. **77** (Jan, 1950) 242–245.

Appendix A

Tag & Probe method

The *Tag & Probe* is widely used in particle physics for testing the efficiency of some selection on leptons. It consists of tagging a clean sample of events using one lepton from the decay of a well-known particle and then measuring the efficiency of interest using the second lepton from the decay of the same particle. The particle is chosen based on the p_T range which we want to probe, for example the J/ψ and Υ resonances can be used for low p_T leptons while W and Z bosons are usually employed for leptons above 10 GeV. The "tag" lepton is the one on which we will apply tight selection criteria, to ensure that the background contamination is as small as possible in our selection; the "probe" lepton is, instead, the one on which we want to test our selection and thus only a loose selection (or even no selection at all) is applied on this one.

J/ψ, Υ and Z can be exploited by requiring that the invariant mass of the tag+probe system is within a small window around the mass of the particle used, thus reducing the contamination from background. Also the W boson can be used, but in this case the tag will be given by the neutrino, i.e. a large missing transverse energy in the event. This case of application of the *Tag & Probe* is more delicate, as the transverse mass[1] reconstructed of the tag+probe

[1] Since p_z^ν is unknown, we cannot reconstruct the ev invariant mass and therefore must resort to other kinematic variables for the mass measurement

$$m_T = \sqrt{2\mathrm{p}_T{}^e \mathrm{p}_T{}^\nu \cdot (1 - \cos(\phi^e - \phi^\nu)}$$

This variable has the advantage that its spectrum is relatively insensitive to the production dynamics of the W.

system does not provide sufficient separation between signal and background: another discriminant is thus needed, such as isolation, for example.